UNIVERSITY OF CALIFORNIA, SAN DIEGO

Upper-ocean variability in Drake Passage and the Weddell Sea: Measuring the oceanic response to air-sea and ice-ocean interactions

A dissertation submitted in partial satisfaction of the
requirements for the degree
Doctor of Philosophy

in

Oceanography

by

Gordon Ronald Stephenson, Jr.

Committee in charge:

Sarah T. Gille, Co-Chair
Janet Sprintall, Co-Chair
Jan Kleissl
Robert Pinkel
Daniel Rudnick
Maria Vernet

2012

The dissertation of Gordon Ronald Stephenson, Jr. is approved, and it is acceptable in quality and form for publication on microfilm and electronically:

_____

_____

_____

_____

_____
Co-Chair

_____
Co-Chair

University of California, San Diego

2012

DEDICATION

Dedicated to my uncle John Stephenson and to my parents, Gordon and Liz.

EPIGRAPH

The world is always full of the sound of waves. ... The little fishes, abandoning themselves to the waves, dance and sing and play, but who knows the heart of the sea, a hundred feet down? Who knows its depth?

— excerpt from Musashi by Eiji Yoshikawa

TABLE OF CONTENTS

LIST OF FIGURES

ACKNOWLEDGEMENTS

Working with Sarah Gille and Janet Sprintall has been an honor. I have benefited greatly from their guidance and their thoughtful and insightful comments. I am grateful for their kindness and dedication, their persistence through many revisions, and especially for their patience, which has withstood all the tests I put to it.

I am also thankful for the support of the other members of my committee. I would like to thank Maria Vernet for her enthusiasm and for introducing me to the world of icebergs, Dan Rudnick and Rob Pinkel for their guidance as I planned my research, and Jan Kleissl for his help as I finished my research. I would also like to thank my former committee member, Paul Linden, for his input on Chapter IV as it was being prepared.

The help and support of SIO staff has been invaluable. Special thanks go to Tomomi Ushii and Phil Moses, who have helped me throughout my time at SIO. Thanks also go to April Fink for helping me with fellowship applications, to Gilbert Bretado for helping organize my defense, and to the rest of the SIO graduate office.

My life has been greatly enriched by the support and friendship of my peers. So thank you to all my mates. My office mates Tamara and Dian, who for years has been an unending source of chocolate and laughter. My hall mates Jim and Kyla, who inspired me by the examples they set. A note in the acknowledgments is insufficient to express thanks for my classmates; San, Yvonne, Peter, Ben, Aneesh, Mike, James, Shang, and Tom made up much of my day-to-day world, and it was a good one. I have also been fortunate to have wonderful housemates; thank you Anais, Jason, James, and Kaushik, for cooking and sharing and late-night discussions. Thanks also to my shipmates during the iceberg cruise on the N.B. Palmer, in particular to Ron and John and Maria, who have since been my co-authors and collaborators. And thanks to my teammates, the Pier Gladiators, for spending 300 hours of toe-breaking, mind-clearing soccer on the beach.

Finally, thank you to my family for their love and support, and to Claire, who understands.

Chapter 2, in full, is a reprint with no modifications to content of the article as it appears in Journal of Geophysical Research-Oceans, 2012, G.R. Stephenson Jr., S.T. Gille, and J. Sprintall, reproduced with permission of American Geophysical Union. The dissertation author was the primary researcher and author of this manuscript. Janet Sprintall provided the XBT/XCTD data and directed and supervised the research along with Sarah Gille.

Chapter 3, in full, is a manuscript in preparation for publication. I was the primary researcher and author of this material, with contributions from co-authors Sarah Gille and Janet Sprintall.

Chapter 4, in its entirety, is a reprint with no modifications to content of the article as it appears in Deep-Sea Research II, 2011, G.R. Stephenson Jr., J. Sprintall, S.T. Gille, M. Vernet, J.J. Helly, and R.S. Kaufmann, reproduced with permission of Elsevier. I was the primary researcher and author of this manuscript. Maria Vernet, John Helly, and Ron Kaufmann contributed to the field component of the research which forms the basis of this chapter. Janet Sprintall and Sarah Gille supervised the analysis and writing of the manuscript.

VITA

2006	B.S., Mathematics and Atmospheric and Oceanic Sciences, University of Wisconsin-Madison
2012	Ph.D., Oceanography Scripps Institution of Oceanography, University of California, San Diego.

PUBLICATIONS

Stephenson G.R. Jr., Gille S.T., and J. Sprintall, [in prep]: Interannual variability of upper ocean heat content in Drake Passage.

Stephenson G.R. Jr., Gille S.T., and J. Sprintall, 2012: Seasonal variability of upper ocean heat content in Drake Passage. *J. Geophys. Res.*, **117**, C04019.

Stephenson G.R., Sprintall J., Gille S.T., Vernet M., Helly J.J., and R.S. Kaufmann, 2011: Subsurface melting of a free-floating Antarctic iceberg. *Deep-Sea Res. II.*, **58**(11-12), 1336–1345.

Helly J.J., Kaufmann R.S., Vernet M., and G.R. Stephenson, 2011: Spatial characterization of the meltwater field from icebergs in the Weddell Sea. *Proc. of the Nat. Acad. of Sci.*, **108**(14), 5492–5497.

Helly J.J., Kaufmann R.S., Stephenson G.R., and M. Vernet, 2011: Cooling, dilution and mixing of ocean water by free-drifting icebergs in the Weddell Sea. *Deep-Sea Res. II.*, **58**(11-12), 1346–1363.

Gille, S.T., A. Lombrozo, J. Sprintall, G. Stephenson and R. Scarlet, 2009: Anomalous spiking in spectra of XCTD temperature profiles. *J. Atmos. Ocean. Tech.*, **26**(6), 1157–1164.

Fukumura, K., D. Kazanas, and G. Stephenson, 2009. Quasi-periodic oscillations from random X-ray bursts around rotating black holes. *The Astrophysical Journal*, **695**, 1199-1209.

Seemann, S., E. Borbas, R. Knuteson, H.-L. Huang, and G. Stephenson, 2008: Global infrared emissivity for clear sky atmospheric regression retrievals. *J. Appl. Meteorol. Climatol.*, **47**(1), 108–123.

Lehman-Ziebarth, N., P. Heideman, R. Shapiro, S. Stoddart, C. Hsiao, G. Stephenson, P. Milewski, and A. Ives, 2005: Evolution of Periodicity in Periodical Cicadas. *Ecology*, **86**(12), 3200–3211.

ABSTRACT OF THE DISSERTATION

Upper-ocean variability in Drake Passage and the Weddell Sea: Measuring the oceanic response to air-sea and ice-ocean interactions

by

Gordon Ronald Stephenson, Jr.

Doctor of Philosophy in Oceanography

University of California, San Diego, 2012

Sarah T. Gille, Co-Chair
Janet Sprintall, Co-Chair

In the first part of this dissertation, reanalysis heat flux products and profiles from a 15 year time series of high-resolution, near-repeat expendable bathythermograph / expendable conductivity-temperature-depth (XBT/XCTD) sampling in Drake Passage are used to examine sources of upper-ocean variability, with a focus on the nature of MLD variations and their impact on a first-order, one-dimensional heat budget for the upper ocean in the regions north and south of the Polar Front. Results show that temperature and density criteria yield different MLD estimates, and that these estimates can be sensitive to the choice of threshold. The difficulty of defining MLD in low-stratification regions, the large

amplitude of wintertime MLD (up to 700 m in Drake Passage), and the natural small-scale variability of the upper ocean result in considerable cast-to-cast variability in MLD, with changes of up to 200 m over 10 km horizontal distance. In contrast, the heat content over a fixed-depth interval of the upper ocean shows greater cast-to-cast stability and clearly measures the ocean response to surface heat fluxes. In particular, an annual cycle in upper ocean heat content is in good agreement with the annual cycle in heat flux forcing, which explains 24% of the variance in heat content above 400 m depth north of the Polar Front and 63% of the variance in heat content south of the Polar Front. At interannual timescales, the primary drivers of interannual variations in upper-ocean heat content in Drake Passage are advective processes; up to 40% of the variance of cross-Passage average upper-ocean heat content is due to meanders of the Polar Front, while 14% of the variability results from mesoscale eddies. Heat flux anomalies contribute less variance (5-10%) on interannual timescales. Teleconnections with ENSO and SAM contribute to anomalies in meridional winds and heat fluxes. As a result, ENSO and SAM contribute variability in upper ocean heat content at near-zero lags; ENSO and SAM are also correlated with upper ocean heat content anomalies on timescales of ∼2-5 years.

The second part of this dissertation explores a melting iceberg as a source of upper-ocean variability. Observations near a large tabular iceberg in the Weddell Sea in March and April 2009 show evidence that water from ice melting below the surface is dispersed in two distinct ways. Warm, salty anomalies in T-S diagrams suggest that water from the permanent thermocline is transported vertically as a result of turbulent entrainment of meltwater at the iceberg's base. Stepped profiles of temperature, salinity, and density in the seasonal thermocline are more characteristic of double-diffusive processes that transfer meltwater horizontally away from the vertical ice face. These processes contribute comparable amounts of meltwater–O(0.1 m^3) to the upper 200 m of a 1 m^2 water column–but only basal melting results in significant upwelling of water from below the Winter Water layer into the seasonal thermocline. This suggests that these two processes may have different effects on vertical nutrient transport near an iceberg.

Chapter 1

Introduction

As anthropogenic forcing alters atmospheric conditions worldwide, the effects on the global ocean are mediated by interactions between the atmosphere, cryosphere, and ocean. The Southern Ocean serves as an entry point for deep-ocean sequestration of carbon (Caldeira and Duffy, 2000), and Southern Ocean warming is implicated in the future response of global atmospheric temperatures to increased radiative forcing associated with increasing atmospheric CO_2 concentrations (Boé et al., 2009). Predicted changes in Antarctic climate associated with anthropogenic warming include strengthening of the circumpolar westerly winds and a southward shift in Southern Ocean storm tracks (Bracegirdle et al., 2008). Global changes in large-scale atmospheric forcing have been associated with shifts in the frequency or intensity of climate modes such as El Niño / Southern Oscillation (ENSO) and the Southern Annular Mode (SAM) (e.g., Meredith et al., 2008), and significant responses to these modes of atmospheric variability have been seen in the Southern Ocean (e.g., Meredith et al., 2008; Sprintall, 2008; Sallée et al., 2008) and in the sea-ice along the coast of Antarctica (e.g., Yuan and Martinson, 2000; Kwok and Comiso, 2002; Sprintall, 2008). The response of the Antarctic Circumpolar Current (ACC) in particular has been shown to affect global water mass properties (Naveira Garabato et al., 2009), and the global meridional overturning circulation (Wolfe and Cessi, 2010; Marini et al., 2011). The global ocean heat budget is sensitive to the amount of energy taken up by the Southern Ocean (see, e.g., Trenberth and Fasullo, 2010; Gille, 2008; Levitus et al., 2009); however, the remoteness and extreme conditions of the Southern Ocean have led to a historical scarcity of *in situ* measurements in the region, and there remains considerable uncertainty in the basic heat budget of the upper ocean in the region (Dong et al., 2007). This dissertation examines several different ways to measure the effects of air-sea or ice-ocean interactions so that we can better identify the mechanisms that govern upper ocean variability in the Southern Ocean and better predict the changes that might occur as a result of a changing climate.

One of the primary objectives of Chapter 2 is to identify a robust way to measure the response of the upper ocean to surface forcing. Mixed-layer depth (MLD) is commonly used to define the lower limit of direct atmospheric forcing in

the ocean, but MLD is also a major source of uncertainty in the Southern Ocean heat budgets (Dong et al., 2007). The variability of MLD estimates is strongly affected by oceanic conditions; low stratification and interleaving layers contribute to high variability north of the Polar Front, while a strong permanent pycnocline limits MLD variability south of the Polar Front. Thus, MLD is an unreliable measure of the effects of surface forcing on the upper ocean, as the response of MLD to a given atmospheric input is inconsistent. A more robust measure of the response of the upper ocean to atmospheric forcing is found to be the heat content of the upper ocean over a fixed depth range. Heat content is directly forced by surface heat fluxes, and results show that on seasonal time scales, a climatological seasonal cycle in surface heat fluxes is sufficient to explain ∼24% of the variance in upper ocean heat content above 400 m depth in the region north of the Polar Front in Drake Passage and ∼63% of the variance in upper ocean heat content in the region south of the Polar Front in Drake Passage (Stephenson et al., 2012).

Chapter 3 continues the exploration of upper ocean heat content variability in Drake Passage with the goal of identifying the mechanisms governing variability in upper ocean heat content at interannual time scales. An effort is made to distinguish between two types of interannual variability: variability governed by changes in surface forcing on interannual time scales and variability intrinsic to the ocean, such as frontal meanders and mesoscale eddies. On interannual time scales, heat flux anomalies upstream of Drake Passage make a small (5-10%) but significant contribution to upper ocean heat content variability. These heat flux anomalies are strongly linked to meridional wind anomalies, as other studies have also shown (e.g., Meredith et al., 2008; Naveira Garabato et al., 2009). Meridional wind anomalies, in turn, have been linked to ENSO and, in the southeast Pacific, to SAM (Turner, 2004). The response of upper-ocean heat content in Drake Passage to ENSO and SAM generally compares favorably with the response of surface or near-surface temperatures seen in other studies in locations in or near Drake Passage (Meredith et al., 2008; Sprintall, 2008; Naveira Garabato et al., 2009). The contribution of mesoscale eddies and frontal meanders to interannual variations in upper ocean heat content is examined using a database of tracked eddies (Chelton

et al., 2011b). Mesoscale variability appears to play a dominant role in governing upper ocean heat content in Drake Passage; eddies and meanders explain nearly half of the interannual variability of upper ocean heat content averaged across Drake Passage. Together, heat fluxes, ENSO variability, mesoscale eddies and frontal meanders explain ∼84% of the total (seasonal and interannually-varying) variance in average heat content above 400 m in Drake Passage.

The remainder of the dissertation focuses on ice-ocean interactions. Calving from glaciers in Antarctica accounts for 2,000 Gt of yearly freshwater input into the Southern Ocean, half of which takes the form of large tabular icebergs (Jacobs et al., 1992). Changes in upper ocean temperatures and circulation near the coast of Antarctica have the potential to rapidly melt ice sheets (Jacobs et al., 2011). Recent large ice-shelf break-ups, such as the Wilkens Ice Shelf in spring 2009 and Larsen B in 2002, were followed by an intense period of iceberg spawning. Due to the potential sea level rise associated with melting of ice shelves and ice sheets, considerable effort has been undertaken to understand how oceanic conditions and atmospheric conditions contribute to melting, calving, and ice-shelf break-up (e.g., Jacobs et al., 2011). The influence of icebergs on the ocean is less well understood. Drifting icebergs redistribute heat and freshwater, and transport trace metals and phytoplankton (Smith et al., 2007). Recent studies have shown that the wake of an iceberg is associated with an increase in surface chlorophyll concentration (Schwarz and Schodlok, 2009), and their effect on surface temperature and salinity may affect rates of sea-ice formation and Antarctic Bottom Water formation (Jongma et al., 2009). In regions with high iceberg concentrations, such as the Weddell Sea, iceberg meltwater is a larger term in the freshwater balance than the precipitation minus evaporation, and large icebergs greater than 10 nautical miles in one dimension are thought to be responsible for most of the transport of freshwater north of 63° S (Silva et al., 2006). Models that include icebergs often consider them as sources of surface freshwater(e.g., Jongma et al., 2009). While icebergs do have a net cooling and freshening effect on the surface ocean (Helly et al., 2011a) over distances of tens of kilometers (Helly et al., 2011b), they also have a vertical extent of tens to hundreds of meters. Melting that occurs below the sea surface produces meltwater

that can be dispersed in complicated ways.

Chapter 4 presents a detailed case study of the effects of one large tabular iceberg on the upper-ocean in the northwest Weddell Sea in March-April 2009. Subsurface melting at the sides and base of an iceberg introduces iron-rich meltwater to the surrounding ocean in two ways (Stephenson et al., 2011). Double-diffusive processes at the iceberg's sidewalls lead to the formation of stepped features in temperature and density profiles that may transport meltwater horizontally over tens of kilometers. Meltwater formed at the base of an iceberg appears to mix turbulently with surrounding Weddell Deep Water, resulting in an injection of relatively warm, nutrient-rich water to the base of the thermocline, presenting possibilities for vertical nutrient transport that may contribute to observed productivity increases in the wake of large icebergs (Schwarz and Schodlok, 2009).

Chapter 2

Seasonal variability of upper ocean heat content in Drake Passage

2.1 Abstract

Mixed-layer depth (MLD) is often used in a mixed-layer heat budget to relate air-sea exchange to changes in the near-surface ocean temperature. In this study, reanalysis heat flux products and profiles from a 15-year time series of high-resolution, near-repeat XBT/XCTD sampling in Drake Passage are used to examine the nature of MLD variations and their impact on a first-order, 1-D heat budget for the upper ocean in the regions north and south of the Polar Front. Results show that temperature and density criteria yield different MLD estimates, and that these estimates can be sensitive to the choice of threshold. The difficulty of defining MLD in low-stratification regions, the large amplitude of wintertime MLD (up to 700 m in Drake Passage), and the natural small-scale variability of the upper ocean result in considerable cast-to-cast variability in MLD, with changes of up to 200 m over 10 km horizontal distance. In contrast, the heat content over a fixed-depth interval of the upper ocean shows greater cast-to-cast stability and clearly measures the ocean response to surface heat fluxes. In particular, an annual cycle in upper-ocean heat content is in good agreement with the annual cycle in heat flux forcing, which explains ∼24% of the variance in heat content above 400 m depth north of the Polar Front and ∼63% of the variance in heat content south of the Polar Front.

2.2 Introduction

The Southern Ocean has experienced statistically significant warming over the past few decades (Böning et al., 2008; Gille, 2008; Levitus et al., 2009). Warming of the interior ocean contributes to thermosteric sea level rise (Church et al., 2011), but heat uptake by the ocean may also act to slow the warming of the atmosphere associated with anthropogenic forcing (Boé et al., 2009). Intermediate water properties of much of the world ocean are set by air-sea interactions in the Southern Ocean (Hanawa and Talley, 2001). In recent decades, Subantarctic Mode Water and Antarctic Intermediate Water have shown changes consistent with surface warming and increased precipitation in their Southern Ocean source regions

(Bindoff and McDougall, 2000; Durack and Wijffels, 2010). Understanding the rate at which heat is transferred from the atmosphere through the upper layers of the Southern Ocean will help us better determine the effects of global warming on both the ocean and the atmosphere.

In many studies of air-sea exchange, the limit of the upper-ocean is defined to be the mixed layer. The mixed-layer depth (MLD) can be used to relate near-surface temperature changes to the heat fluxes in and out of the mixed layer (e.g. Kuhnel and Henderson-Sellers, 1991; Qiu and Kelly, 1993; Dong et al., 2007). In the Southern Ocean, several mixed-layer depth climatologies have been developed (e.g. Kara et al., 2003; de Boyer Montégut et al., 2004; Dong et al., 2008; Holte and Talley, 2009). However, the MLD values in these climatologies differ depending on the methods (e.g. threshold difference, gradient, hybrid algorithm) (Holte and Talley, 2009) and parameters (e.g. temperature vs. density) (de Boyer Montégut et al., 2004) that are used to determine MLD. In the Southern Ocean, weak stratification or temperature inversions are common (Dong et al., 2008) and may contribute to the disagreement between estimates of MLD. Differences in Southern Ocean MLD estimates contribute to uncertainty not only in Southern Ocean heat budgets (Dong et al., 2007) but in global climate models as well. For example, MLD differences are a major cause of inter-model spread in the projected rate of heat transfer to the ocean interior and hence to the projected rate of increase of globally-averaged surface air temperature in the next 100 years (Boé et al., 2009). This underscores the importance of determining accurate and reliable estimates of vertical heat transfer in the Southern Ocean.

In fact, the choice to use MLD as the representative length scale for vertical mixing of heat within the upper ocean is not obvious. In their seminal paper, Price et al. (1986) introduced a vertical-mixing model (known as "PWP") that is now widely used to study the temporal evolution of the upper ocean, including the mixed layer. In the same study, Price et al. (1986) acknowledged some limitations of MLD. Calculating MLD is an attempt to define a quasi-homogeneous layer, where water properties (often temperature or density) are roughly uniform; the degree of desired homogeneity can be tuned by requiring that water properties

vary by less than a specified amount. When stratification in the upper ocean is weak, MLD estimates can be sensitive to the specified degree of non-homogeneity. Price et al. (1986) addressed this limitation and discussed two other vertical length scales: "trapping depth" is the weighted average depth of the temperature anomaly above a reference depth; "penetration depth" is a depth derived by relating the rate of change of near-surface temperature to changes in the upper-ocean heat content. In the following, we will show that upper-ocean heat content itself can be a useful measure of ocean uptake of heat from the atmosphere.

Surface forcing is one of the main drivers of upper-ocean variability, providing the energy input for seasonal cycles in oceanic heating and cooling. A good measure of upper-ocean variability will reflect the changes in ocean state corresponding to such forcing; however, other processes can also influence the upper-ocean. Horizontal advection in the form of eddies and frontal meanders, for example, can cause a strong warming or cooling signal through the upper 1000 m of the water column (e.g., Joyce et al., 1981). Vertical entrainment and mixing within the upper ocean redistribute heat internally and are a source of upper-ocean variability. To the extent that these processes are occurring in the upper ocean, the relationship between surface forcing and parameters representing the state of the upper ocean becomes less immediate and more difficult to discern.

This study will compare the characteristics of several measures of upper-ocean variability and evaluate their utility as measures of the ocean's response to surface heating. We focus on the Drake Passage, where a 15-year time-series of profile data from expendable probes along a near-repeat transect allows estimation of the seasonal patterns of surface heat forcing and the oceanic response. Section 2.3 describes the upper-ocean data and the heat flux products used in the analysis. Section 2.4 compares characteristics of MLD and heat content. Section 2.5 relates seasonal patterns in surface forcing, mixed-layer heat content and upper-ocean heat content. We present a simplified two-term (temperature tendency and total heat flux) seasonal heat budget for the upper ocean and assess its validity in the Drake Passage. Section 2.6 summarizes our findings.

2.3 Data

2.3.1 XBT and XCTD profiles

Variability in the upper ocean is examined using data collected as part of the high-resolution eXpendable Bathythermograph (XBT) / eXpendable Conductivity, Temperature, Depth (XBT/XCTD) sampling program (Sprintall, 2003) in Drake Passage (Fig. 2.1). Since 1996, approximately 6-7 XBT transects have been undertaken each year, resulting in a total of 91 transects to February 2010. Each transect typically takes 2-3 days to complete. Approximately 70 XBTs are dropped per transect. XBT casts are spaced 10-15 km apart, except when crossing the Subantarctic Front and the Polar Front, where casts are spaced 6-10 km apart. XBTs return temperature at 2 m vertical resolution to a depth of ∼850 m. The fall-rate correction of Hanawa et al. (1995) has been applied to each profile. Most transects after 2001 also include ∼10-12 XCTD profiles, spaced 25-50 km apart (Fig. 2.1). XCTDs return profiles to ∼1100 m of temperature (T) and conductivity, from which salinity (S) and density (ρ) can be calculated. The effective vertical resolution of the XCTDs is at best about 0.7 m (Gille et al., 2009). In this analysis, we have smoothed the XCTD T, S, and ρ to an effective resolution of 2 m using a low-pass filter (11 point least-squares, pass band = 0.07, stop band = 0.10) and then sub-sampled at 2 m depth increments.

When an XBT or XCTD is deployed, the probe requires a few seconds to equilibrate to the seawater temperature. Hence, the top 10 m of a cast may contain spurious temperatures. For this study, temperature values shallower than 10 m were replaced with the 11-m temperature value; one result of this replacement is that temperature is assumed to be well-mixed to at least 11 m depth.

Of the 91 XBT/XCTD transects, three cruises (September 1999, June 2000, and January 2009) deviated significantly from the typical crossings outlined in Figure 2.1 and another three (February 1998, May 1998, and July 1999) surveyed only the northern half of Drake Passage, likely due to sea-ice or foul weather. Data from these cruises have been omitted from our analysis (accounting for 372 XBT casts and 11 XCTD casts). In addition, while 70% of casts reached 800 m depth,

casts that do not reach at least 400 m depth are omitted as they may not fully resolve the mixed layer. From the 85 XBT/XCTD transects we considered for this study, we have included 5071 of a possible 5637 XBT casts and 343 of a possible 360 XCTD casts. Of these, 2668 XBT and 213 XCTD casts were collected north of the Polar Front, defined here as the northward extent of the 2 °C isotherm at 200 m depth (Orsi et al., 1995), and 2403 XBT casts and 130 XCTD casts were collected south of the Polar Front.

2.3.2 Heat Fluxes

In situ meteorological observations needed to determine the air-sea exchanges that comprise surface heat fluxes are sparse in the Southern Ocean. Several remote-sensing and reanalysis products provide estimates of the net heat flux into the ocean, but these products may differ by more than their uncertainties (e.g. Dong et al., 2007). Furthermore, systematic errors in estimates of high-latitude cloud cover cause a positive bias in the reanalysis surface heat fluxes over the Southern Ocean (Trenberth and Fasullo, 2010). As a result, surface heat fluxes are a major source of error in Southern Ocean heat budgets. To allow for the expected differences between heat flux products, we compared the daily, gridded heat fluxes of three products: NCEP-NCAR reanalysis, a $\sim$1.9° x 1.9° resolution product that we have sampled over 1 January 1996 - 31 December 2010; Japanese Ocean Flux dataset with Use of Remote Observations (J-OFURO, Kubota et al., 2002), at 1° x 1° resolution from 1 January 1997 to 31 December 2006; and Objectively Analyzed Fluxes (OAFlux, Yu and Weller, 2007), at 1° x 1° resolution from 1 January 1996 to 31 December 2007. Only the dataset from the NCEP-NCAR reanalysis overlapped the full time span of the XBT/XCTD transects (1996-2010); however, both J-OFURO and OAFlux flux products spanned 10 or more years, which should be sufficient to examine the annual cycle.

For each heat flux product, spatial averages were computed for regions north (56-59° S, 60-64° W) and south (59-62° S, 60-64° W) of the climatological position of the Polar Front (Orsi et al., 1995) in Drake Passage. The climatological position of the Polar Front was used rather than the instantaneous position because

we are also interested in determining the heat accumulating in the time intervals between transects, when there are no XBT data available to confirm the location of the Polar Front. Since the heat fluxes are fairly smooth (Dong et al., 2007), small shifts in the location of the Polar Front should not affect our results. For each heat flux product and region (north or south of the Polar Front), a monthly climatology of Q_{net} values was constructed (Fig. 2.2). The maximum heat input into the ocean ($\sim$150 to 200 W m^{-2}) occurs in December, while the greatest heat loss from the ocean surface (-100 to -50 W m^{-2}) occurs in June (Fig. 2.2). The annual cycle in heat fluxes is nearly sinusoidal; to quantify the amplitude and phase of the seasonal cycle, we least-squares fit a sinusoid with a period of 365.25 days to the timeseries of heat fluxes; this fit explained 64% of the variance in NCEP heat fluxes, 73% of the variance in OAFlux, and 74% of the variance in J-OFURO fluxes. Uncertainties were computed by multiplying the error estimates from the least-squares fitting procedure by the standard deviation of the heat flux values. A Monte-Carlo method with N=10^5 was used to calculate the uncertainty on the date of maximum amplitude.

The mean annual heat flux is positive (into the ocean) for all of the heat flux products (Table 2.1), with OAFlux indicating the largest mean net heat flux into the ocean both north and south of the Polar Front. All heat flux products show that the mean net heat flux is greater south of the Polar Front than north (Table 2.1). This north-south difference is greatest for J-OFURO (16 W m^{-2}). NCEP fluxes, with lower spatial resolution, showed a cross-frontal difference of only 2 W m^{-2}, which was smaller than the uncertainties in the annual mean. Despite the differences in the annual mean values of net air-sea heat flux, the amplitudes ($\sim$130 W m^{-2}) and phases (maximum within a few days of December 25) of the seasonal cycles in surface heating were remarkably similar between all products (Fig. 2.2, Table 2.1) and for the regions north and south of the Polar Front. *In situ* observations in Drake Passage have also found no significant differences in the seasonal cycle of turbulent heat fluxes across the Polar Front (Dong et al., 2007; Jiang et al., 2011). In this study, we examine the seasonal cycle in heat flux after the annual mean (Table 2.1) has been removed. After removing an annual mean,

we found little difference between heat flux products or between regions north and south of the Polar Front; therefore, in the following we will use only the results from NCEP heat fluxes north of the Polar Front to represent the annual cycle in heat flux forcing in Drake Passage.

2.4 Measures of upper-ocean variability

In Drake Passage, the Polar Front represents a boundary between two regions with distinct water mass characteristics. The difference is clearly visible in a section of temperature across Drake Passage, collected in late September 2009 at the end of austral winter (Fig. 2.3a). South of the Polar Front, Antarctic Surface Water (AASW) of the upper layer is colder than the upper Circumpolar Deep Water immediately below it. In summer, this cold layer is capped by warmer water, but a temperature minimum (inversion) at ∼150 m is nearly always present. The temperature inversion is density-compensated by salinity that increases with depth (Sprintall, 2003). North of the Polar Front, temperature stratification is weak and temperature generally decreases as depth increases, although occasionally small-amplitude inversions related to water mass interleaving and eddy mixing occur at depth (e.g., Sprintall, 2003). The differences in water-column structure north and south of the Polar Front complicate efforts to understand the upper-ocean variability of both regions using MLD. This section explores the robustness and the small-scale spatial variability of MLD as compared to the use of upper-ocean heat content.

Two other parameters that measure upper-ocean variability, trapping depth (D_T) and penetration depth (D_p), were also explored. D_T is essentially the mean depth of the temperature anomaly in the upper ocean (Price et al., 1986),

$$D_T = \frac{1}{T(z_{ref}) - T(0)} \int_{-z_{ref}}^{0} z \ (T(z) - T(0)) \ dz, \tag{2.1}$$

where T is temperature and z_{ref} is a lower reference depth. South of the Polar Front, the permanent temperature inversion makes the denominator in (2.1) close to zero or negative for $z_{ref} \geq$200 m, leading to spurious values for D_T. Hence D_T

does not provide a useful measure of upper-ocean variability in Drake Passage. D_p infers the depth to which heat fluxes are mixed by tracking changes in sea surface temperature (SST) and upper-ocean heat content. This requires a time series with more regular sampling than is available from our XBT timeseries in Drake Passage, so D_p is also not suited to the purposes of this study.

2.4.1 Mixed-layer depth

Two methods are typically employed to identify mixed-layer depth. The threshold (also known as finite-difference) method defines MLD as the depth at which a water property differs by a fixed amount from its surface value. In contrast, gradient methods determine MLD by locating a strong vertical gradient in a water property. The two methods often give different MLDs even in an idealized upper-ocean density profile, as they rely on choices of predetermined threshold and gradient (e.g. Holte and Talley, 2009). In the real ocean, the threshold method is more stable than the gradient method because profiles of the vertical derivatives of temperature or salinity are generally noisier than the properties themselves (Brainerd and Gregg, 1995). Holte and Talley (2009) developed a hybrid approach that applies several techniques, including threshold and gradient methods, to identify candidate MLDs and then selects one based on physical characteristics of the profile. To simplify comparison with mixed-layer climatologies, in this study we present results using the threshold method. The simplicity of the threshold difference also enables us to identify the cause of variations in MLD estimates between different profiles. Qualitatively similar results are obtained if MLD is calculated with the gradient method or the algorithm of Holte and Talley (2009).

We consider two variants of the threshold method of determining MLD. The first, MLD_T, is computed using a temperature threshold and is defined so that the base of the mixed layer at z_{ML} is the shallowest depth such that $|T(z_{ML}) - T_0| \geq \Delta T$, where T_0 is the near-surface temperature (at 11 m), and ΔT is the difference threshold. The presence of temperature inversions (Fig. 2.3a) makes the absolute value in this definition necessary. The second, MLD_ρ, is computed using a density threshold, finding z_{ML} such that $|\rho(z_{ML}) - \rho_{sfc}| \geq \Delta\rho$. While Holte and Talley

(2009) found that MLD estimates based on density are generally more accurate than those based only on temperature, the abundance of temperature profiles and relative lack of density profiles make consideration of both types of MLD estimates necessary. Following other studies of MLD in the Southern Ocean (e.g. de Boyer Montégut et al., 2004; Dong et al., 2008), we use a temperature threshold (ΔT) of 0.2 °C and a potential density threshold ($\Delta \rho$) of 0.03 kg m^{-3}.

Differences in MLD_T and MLD_ρ can occur where significant salinity changes occur with depth. A winter-time profile south of the Polar Front (at 58.5° S, 63.7° W) (Fig. 2.4a-c) shows temperature and salinity both increase with depth, but a salinity gradient near the surface is not mirrored in the temperature profile. As a result MLD_ρ is 80 m shallower than MLD_T. By contrast, in a winter-time profile north of the Polar Front (at 56.5°, 64.1° W) (Fig. 2.4d-f), the salinity gradient is much weaker, and MLD_ρ is only 18 m shallower than MLD_T.

Seasonal and regional differences between MLD_T and MLD_ρ are reflected in the cumulative distribution functions of MLD_T-MLD_ρ (Fig. 2.5a). MLD_T is typically deeper than MLD_ρ (i.e. right of 0-line in Fig. 2.5a). In our Drake Passage data set, we find that MLD_T is greater than MLD_ρ by at least 10 m in 58% of all casts, while in 38% of casts, MLD_T and MLD_ρ differ by less than 10 m. The difference between MLD_T and MLD_ρ is generally smaller in summer (December to March) than winter (June to September) (Fig. 2.5a; Table 2.2) and is smaller on average south of the Polar Front than north (Table 2.2). In 4% of casts, MLD_T is shallower than MLD_ρ by more than 10 m. These casts are characterized by density-compensating layers, occur mostly in winter, and are more often found south of the Polar Front than north.

The difference between MLD_T and MLD_ρ varies with the upper-ocean temperature stratification, which, in turn, varies seasonally and by region. Our results agree with those of Holte and Talley (2009), who found that MLD_T tends to overestimate the depths of deep mixed layers relative to MLD_ρ, and suggest that temperature is not always adequate for accurately determining MLD. This is especially the case in winter, when Drake Passage is characterized by deep mixing and low stratification. In the absence of strong vertical density or temperature

gradients, it can be difficult to unambiguously determine the true depth of mixing using MLD. To test the robustness of MLD estimates to the choice of threshold, we perturbed ΔT by ± 0.02 °C and $\Delta\rho$ by ± 0.003 kg m^{-3}, a $\pm 10\%$ change to the threshold criteria used to compute MLD$_T$ and MLD$_\rho$, respectively. This procedure is equivalent to perturbing the near-surface temperature or density by the same amount, making this test also a measure of how much MLD might change in response to a small surface heat or buoyancy exchange.

An example of the 10% perturbation in threshold is shown for a typical winter profile from an XCTD cast north of the Polar Front (at 56.5° S, 64.1° W) (Fig. 2.4d-f). MLD$_T$ has been computed using the original threshold criteria of $\Delta T = 0.20$ °C (dashed line in Fig. 2.4d), and the 10% pertubations $\Delta T = 0.18$ °C (top dotted line in Fig. 2.4d) and $\Delta T = 0.22$ °C (lower dotted line in Fig. 2.4d). Decreasing the temperature threshold ΔT reduces MLD$_T$ from 242 m to 240 m, while increasing ΔT deepens MLD$_T$ to 258 m (Fig. 2.4d). MLD$_\rho$ is much more sensitive to the change in $\Delta\rho$ threshold; reducing $\Delta\rho$ from 0.030 to 0.027 kg m^{-3} decreased MLD$_\rho$ from 220 m to 120 m (Fig. 2.4f), while increasing $\Delta\rho$ increased MLD$_\rho$ to 230 m. By contrast, for the cast collected south of the Polar Front (at 58.5° S, 63.7° W) a 10% perturbation to ΔT and $\Delta\rho$ changed MLD$_T$ and MLD$_\rho$ by less than 2 m (Fig. 2.4a-c).

The average MLD$_T$ change in response to a threshold perturbation is larger north of the Polar Front than south and is larger in winter than summer (Table 2.2). A cumulative distribution function of changes in MLD$_T$ shows that perturbing the threshold results in a small (5 m or less) change in MLD$_T$ $\sim$85% of the time, except during winter (June-September) north of the Polar Front (Fig. 2.5b). The reduced sensitivity south of the Polar Front may be a result of the stronger permanent thermocline that provides a lower bound on MLD and results in smaller maximum ΔMLD$_T$. Stronger near-surface temperature gradients in summer account for the reduced summer-time sensitivity to threshold. On average, MLD$_\rho$ and MLD$_T$ are equally sensitive to threshold perturbations north of the Polar Front, and MLD$_\rho$ is a little more sensitive than MLD$_T$ south of the Polar Front (Table 2.2).

Because MLD is sensitive to small-amplitude noise, small differences be-

tween two adjacent profiles may result in large differences in MLD. Two temperature profiles from XBTs deployed only 10 km (∼1 hour) apart north of the Polar Front (at 57.3° S and 57.4° S, 64.0° W on 19 September 2009) have MLD_T of 263 m (Fig. 2.6a) and 118 m (Fig. 2.6b). While these profiles share many features, such as alternating warm and cold layers, a slight warming at 120 m is observed in the southernmost profile (Fig. 2.6b), resulting in MLDs that differ by >100 m.

To quantify the cast-to-cast variability of MLD as observed in Figure 2.6, we computed the root-mean-square (RMS) change in MLD_T from one cast to the next. We selected 5010 pairs of casts that occurred less than one hour apart (typically <10 km spacing). The cast-to-cast difference in MLD_T (± one standard error) is much greater in winter (54±3 m) than summer (20±1 m) and is greater north (40±1 m) than south (24±1 m) of the Polar Front. This agrees with the examples shown in Figures 2.3a and 2.6; south of the Polar Front, MLD variations are small, whereas large MLD changes over short spatial scales are common north of the Polar Front.

2.4.2 Upper-ocean heat content

We expect heat content to show a more direct relationship to heat flux forcing than MLD and to be less affected by cross-frontal differences in temperature stratification than MLD. Potentially, this makes heat content a more consistent, more robust, and less noisy measure of upper-ocean variability. In this section, we examine whether upper-ocean heat content estimated from the Drake Passage data set fulfills this expectation.

We define $\mathcal{H}_{z_0}$, the upper-ocean heat content integrated from the surface to a depth z_0, to be

$$\mathcal{H}_{z_0} = \int_{-z_0}^{0} \rho_0 \; c_p \; T(z) \; dz, \tag{2.2}$$

where $\rho_0 = 1030$ kg m^{-3} is a reference density, $c_p = 3895$ J kg $^{-1\circ}$C^{-1} is the specific heat capacity of seawater, $T(z)$ is the depth-varying temperature, and z_0 is an integration depth to be determined so as to capture the full effect of surface forcing. To assess an appropriate integration depth, the heat content within 50 m

layers between 0 and 800 m depth was computed. Figure 2.7a shows the standard deviation of the heat content over each depth interval for all casts, binned north and south of the Polar Front. South of the Polar Front, the amplitude of variations is small below about 200 m depth, while north of the Polar Front heat content variability has more significant amplitude down to ∼600 m.

Figure 2.7b shows the correlation of heat content in the surface layer (0-50 m) with heat content deeper in the water column. South of the Polar Front, this correlation appears similar to the standard deviation (Fig. 2.7a); surface heat content changes are significantly correlated with heat content changes in layers above 200 m. North of the Polar Front, significant correlation with surface layer heat content are found in layers above ∼350 m. Changes below this depth are uncorrelated with heat content changes in the surface layer (Fig. 2.7b), but still represent a significant fraction of the variability present north of the Polar Front (Fig. 2.7a). The vertical coherence of this additional heat content variability below 350 m is shown by the correlation of heat content in the layer at 750-800 m, the deepest layer for which we had reliable XBT profiles, with heat content in the rest of the water column (Fig. 2.7b). Heat content changes at 750-800 m are well-correlated ($r > 0.8$) with heat content changes in layers below ∼300 m depth south of the Polar Front and below ∼200 m depth north of the Polar Front. This level of vertical coherence is typical of the low-stratification environment of the Southern Ocean and is often associated with advective processes (Sokolov and Rintoul, 2009).

This study aims to test the adequacy of a 1-D heat budget in Drake Passage, forced only by surface heat fluxes; other processes, such as advection, may degrade the validity of this first-order heat balance. The choice of integration depth, z_0 in equation (2.2), reflects a trade-off between capturing as much of the surface-forced signal as possible while avoiding variability unrelated to surface heat fluxes. Based on Figure 2.7b, a choice of z_0= 400 m is likely to reflect all of the heat content signal that is significantly correlated with the surface layer; 400 m is deeper than 99% of the MLD_T estimates. As noted above, vertically-coherent and presumably advective processes below 200 m depth contribute significantly to heat content

variability north of the Polar Front. Selecting z_0= 400 m rather than a deeper integration depth reduces the weight of this variability relative to surface-forced variability, but does not exclude variability resulting from other processes. For z_0= 400 m, 77% of the vertically-integrated temporal and spatial variance in heat content is captured north of the Polar Front and 92% is captured south of the Polar Front. The sensitivity of our results to this choice of z_0 is discussed in section 2.5.

As noted in the introduction, a number of previous studies have examined the heat budget within the mixed layer (e.g. Qiu and Kelly, 1993; Dong et al., 2007). To directly compare the variability of heat content in equation (2.2) with MLD, we also examine the heat content within the mixed layer. Mixed-layer heat content, $\mathcal{H}_{ML}$, is defined as

$$\mathcal{H}_{ML} = \rho_0 \; c_p \; T_{ML} \; h_{ML}, \tag{2.3}$$

where h_{ML} is the depth of the mixed layer (MLD_T), and T_{ML} is the mixed-layer temperature. This quantity is not always directly computed in mixed-layer heat budgets, which more often use MLD to relate heat fluxes to the rate of change of the mixed-layer temperature, but it provides a good analog for $\mathcal{H}_{z_0}$ because the units are the same. Mixed-layer heat budgets often assume that the mixed layer is isothermal, and equation (2.3) represents the mixed-layer heat content under this assumption.

For the XBT/XCTD transect shown in Figure 2.3a, both $\mathcal{H}_{400}$ and $\mathcal{H}_{ML}$ increase with water temperature north of the Polar Front (Fig. 2.3b). Small-scale variability is more pronounced in $\mathcal{H}_{ML}$, as it reflects the large changes in MLD from one cast to the next (e.g., Figure 2.6), particularly north of the Polar Front. Large fluctuations in $\mathcal{H}_{400}$ are not as prominent at these small scales. For example, the RMS cast-to-cast difference in $\mathcal{H}_{ML}$ for the two casts shown in Figure 2.6 is 1.7 GJ m^{-2}, compared with a $\mathcal{H}_{400}$ difference of only 0.2 GJ m^{-2}. This tendency for $\mathcal{H}_{400}$ to exhibit smaller cast-to-cast variations than $\mathcal{H}_{ML}$ is true in general. Differences in $\mathcal{H}_{400}$ and $\mathcal{H}_{ML}$ cast-to-cast variability are greatest in winter north of the Polar Front: the RMS cast-to-cast $\Delta\mathcal{H}_{400}$ (separated by $\sim$10 km) is $<$10% of the RMS cast-to-cast $\Delta\mathcal{H}_{ML}$, while in summer, the RMS of $\Delta\mathcal{H}_{400}$ is about 20% as large as the RMS of $\Delta\mathcal{H}_{ML}$ (Table 2.2). South of the Polar Front, the

differences in cast-to-cast RMS variability are not as extreme; in winter the RMS of $\Delta\mathcal{H}_{400}$ is about 20% as large as $\Delta\mathcal{H}_{ML}$, while in summer the RMS $\Delta\mathcal{H}_{400}$ is 30% as large as RMS $\Delta\mathcal{H}_{ML}$ (Table 2.2). Not only does $\mathcal{H}_{400}$ exhibit smaller RMS cast-to-cast variability than $\mathcal{H}_{ML}$, but it is also more consistent from season to season. Cast-to-cast variability in $\mathcal{H}_{ML}$ is 3-4 times greater in winter than in summer; for $\mathcal{H}_{400}$, RMS cast-to-cast variability in winter is less than twice as great as in summer (Table 2.2). This demonstrates one way in which the use of MLD_T may present a distorted picture of seasonal variability that enhances the apparent upper-ocean variability in winter relative to summer. Use of $\mathcal{H}_{400}$, with its smaller season-to-season differences in RMS cast-to-cast variability, may reduce this distortion.

2.5 Seasonal heating and cooling of the upper ocean

As a first step towards understanding the seasonal variability of upper-ocean heat content, we examined the annual pattern of heat fluxes and the expected changes in heat content. As shown in Table 2.1, the amplitude of the seasonal cycle in heat fluxes is approximately 130 W m^{-2}, with a maximum around 25 December. If a heat flux forcing with this amplitude and phase is integrated in time, it yields an annual cycle in heat content of $\sim$0.66 GJ m^{-2} that peaks on 25 March (green line, Fig. 2.8a,b). In this section, we test whether the mixed-layer and upper-ocean heat budgets reflect this seasonal surface heat input.

For our heat budget, we use a simplified first-order relationship between the heat content $\mathcal{H}$ and the surface forcing Q_{net} in which

$$\frac{\partial \mathcal{H}}{\partial t} = Q_{net}. \tag{2.4}$$

This relationship neglects the effects of advection and vertical entrainment on upper-ocean heat content. Although these other factors may be important to mixed-layer heat budgets (e.g., Qiu and Kelly, 1993; Dong et al., 2007), our main focus here is to isolate the influence of air-sea heat exchange on the ocean to

examine the expected first-order terms in the Southern Ocean.

In our estimate of the seasonal cycle in upper-ocean heat content, we averaged casts that were collected north of the Polar Front separately from those south of the Polar Front for each of the 85 transects (averages denoted by $\overline{\mathcal{H}}$). The date of each cruise average was assigned as the median date of the casts from each transect. A least-squares fit to an annual cycle was made for the time series of $\overline{\mathcal{H}_{ML}}$ (Fig. 2.8a) and $\overline{\mathcal{H}_{400}}$ (Fig. 2.8b). North of the Polar Front, a seasonal cycle in $\overline{\mathcal{H}_{ML}}$ accounts for 38% of the variance and has an amplitude of 0.77 GJ m^{-2} with a maximum occurring July 4, in the middle of austral winter (Fig. 2.8a). South of the Polar Front, a seasonal cycle in $\overline{\mathcal{H}_{ML}}$ with amplitude 0.47 GJ m^{-2} peaks on March 7 and explains 83% of the variance in heat content. For $\overline{\mathcal{H}_{400}}$ north of the Polar Front, an annual cycle with amplitude 0.51 GJ m^{-2} peaks on April 8 and explains 24% of the variance (Fig. 2.8b). South of the Polar Front, the annual cycle has an amplitude of 0.58 GJ m^{-2}, peaks on March 19, and explains 63% of the variance. There are a number of reasons why the seasonal cycle explains a larger fraction of the variance in $\overline{\mathcal{H}_{ML}}$ than in $\overline{\mathcal{H}_{400}}$. South of the Polar Front, MLD is generally much less than 400 m, so that $\overline{\mathcal{H}_{ML}}$ reflects variability nearer the surface, where the seasonal pattern of heating and cooling is stronger. North of the Polar Front, a large seasonal change in MLD, from very shallow in summer to very deep in winter, contributes to the stronger seasonality in $\overline{\mathcal{H}_{ML}}$. In terms of phase, the deep winter MLDs result in a mid-winter (August, Fig. 2.8a) maximum in $\overline{\mathcal{H}_{ML}}$ that occurs about 4 months after the date at which the cumulative heat input has reached its maximum (March). Thus the phase of the seasonal surface heat input agrees with the phase of $\overline{\mathcal{H}_{400}}$ better than with the phase of $\overline{\mathcal{H}_{ML}}$ (Fig. 2.8a).

We tested whether surface heat input and $\overline{\mathcal{H}_{z_0}}$ agreed similarly well for other values of the integration depth z_0. A least-squares fit to a sinusoidal annual cycle was made for $\overline{\mathcal{H}_{z_0}}$ with z_0 ranging from 50 to 800 m varying in 50 m increments. South of the Polar Front, the amplitude of the seasonal cycle changes only slightly with depth below $\sim$100 m (Fig. 2.9a). As z_0 increases, the date of the maximum heat content south of the Polar Front is slightly delayed: at z_0=50 m the cycle peaks in early March, whereas at z_0=800 m the peak occurs in late March

(Fig. 2.9b). South of the Polar Front, the heat fluxes explain 80% of the variance at z_0=100, decreasing to 27% at z_0=800 m (Fig. 2.9c). North of the Polar Front, the amplitude of the seasonal cycle in heat content changes more with increasing z_0, from 0.33 GJ m^{-2} at z_0=100 m to 0.62 GJ m^{-2} at z_0=750 m (Fig. 2.9a). The peak heat content at z_0=800 m occurs in late April, almost 8 weeks later than for z_0=100 m in late February (Fig. 2.9b). Heat fluxes explain 55% of the variance in $\overline{\mathcal{H}_{z_0}}$ at z_0=100 m, while less than 25% of the variance is explained for z_0 >400 m (Fig. 2.9c). At all depths, the amplitude of the annual cycle in heat content was smaller than the 0.66 GJ m^{-2} annual cycle in heat input from surface fluxes. Trenberth and Fasullo (2010) note that reanalysis heat fluxes over the Southern Ocean have a seasonally-varying bias that is greater in summer than winter. Removing such a bias would reduce the amplitude of the annual cycle in heat flux input and may lead to better agreement between the annual cycles in heat content and heat input by surface fluxes.

These results are consistent with the patterns of temperature variance (Fig. 2.7a) that show temperature variations to have higher amplitudes north of the Polar Front than south, illustrating the differences in vertical heat transfer in the two regions. South of the Polar Front, most heat content fluctuations occur above 200 m (Fig. 2.7a); integrating deeper than 200 m adds very little new information and so changes the seasonal cycle in heat content only slightly. North of the Polar Front, however, a clear depth limit to heat content fluctuations is less evident. Heat concentrates in the upper 100 m during the spring restratification, but this heat is gradually mixed downward. The downward mixing of heat away from the surface results in heating at depth that is delayed relative to the surface (Fig. 2.9b). The maximum temperatures at 650-700 m north of the Polar Front, for example, occur in late May (not shown); however, because we have integrated over the whole water column above this depth, the average date of the maximum in $\overline{\mathcal{H}_{700}}$ north of the Polar Front occurs in April. Wintertime cooling at the surface results in a nearly isothermal, cool, water column in the upper 800 m north of the Polar Front around September, following which warming and restratification begin anew. The combination of the abrupt cooling in September and the delay in heat

transfer from the surface to depth is part of the reason the sinusoidal fit to the integrated heat fluxes in Figure 2.8 explains less variance as z_0 increases (Fig. 2.9c). The amplitude of the seasonal cycle in surface heating also decreases with depth. This suggests that the 1-D balance between heat fluxes and heat content degrades as z_0 increases, and the relative importance of other processes, such as horizontal heat advection, may come into play. Finally, these results may also have implications for the choice of the integration depth z_0 such that $\mathcal{H}_{z_0}$ reflects the surface forcing. South of the Polar Front, a choice of z_0 >200 m appears to provide a sufficient constraint. However, north of the Polar Front the relative importance of surface heating to other processes in determining $\mathcal{H}_{z_0}$ varies more greatly with depth and suggests greater sensitivity in this region to the choice of z_0.

The delay of heating with depth in the phase of the seasonal cycle can be used to estimate an effective mixing rate in the upper ocean. In more vigorous mixing regions, surface heating is transported downward quicker, and so less phase change with depth is observed. Conversely, where mixing is less active, surface heating takes longer to propagate downward, resulting in a longer delay of heating with depth. To relate phase to mixing rate, we modeled mixing as an effective diffusivity and numerically solved the heat equation for a system forced at the surface by a sinusoidal annual cycle for a range of diffusivities, κ_{eff}. A relationship was derived between κ_{eff} and the vertical gradient in phase of the resulting $\mathcal{H}_{z_0}$. Our results indicate an annual average of $\kappa_{eff} \approx 10^{-3}$ m^{2}s^{-1} over the upper 200 m of the water column in Drake Passage. While effective diffusivity may be an incomplete representation of a broad array of upper-ocean mixing processes that are not strictly diffusive (e.g. entrainment), our value compares favorably to other measures of vertical diffusivities in this region (e.g., O(10^{-3} m^{2}s^{-1}) Thompson et al., 2007).

2.6 Summary

In this study, we have used XBT/XCTD profiles and reanalysis heat flux products to examine air-sea heat exchange in Drake Passage on a seasonal timescale.

We compared mixed-layer depth and heat content as two methods for measuring the response of the upper-ocean to surface heat forcing. Results of this study show that upper-ocean heat content is a robust indicator of upper-ocean variability due to surface heat flux forcing in Drake Passage.

Regional differences and temporal variability in Drake Passage stratification make it difficult to define MLD such that it is a true measure of the vertical extent of air-sea forcing. Estimates of MLD_T and MLD_ρ can disagree, suggesting that temperature alone is inadequate to unambiguously determine MLD. Further, as a result of low winter-time stratification, MLD estimates are not always robust; low-amplitude forcing or slight changes to the criteria used to define MLD can lead to large changes in MLD estimates. Perhaps as a consequence of the sensitivity of MLD calculations to small differences in temperature profiles, MLD_T also shows considerable variability at small horizontal scales.

In contrast to MLD, upper-ocean heat content is a robust measure of upper-ocean variability. Average cast-to-cast differences in $\mathcal{H}_{400}$ were 3 to 10 times smaller than in $\mathcal{H}_{ML}$; the cast-to-cast variability in $\mathcal{H}_{400}$ also changed less with season and less between the zones north and south of the Polar Front than cast-to-cast variability in $\mathcal{H}_{ML}$. This suggests that $\mathcal{H}_{400}$ is a consistent measure of upper-ocean variability north and south of the Polar Front and in both winter and summer.

A first-order heat balance between the seasonal cycles of anomalous heat fluxes (minus the annual mean) and upper-ocean heat content explains a large fraction ($\sim$63%) of the variance of upper-ocean heat content to 400 m depth south of the Polar Front and to a lesser extent ($\sim$24%) north of the Polar Front. In contrast, an annual cycle that used heat content over the mixed layer did not match the surface-flux driven annual cycle as well in phase or in amplitude. However, the phase and amplitude of the seasonal cycle in $\overline{\mathcal{H}_{z_0}}$ are somewhat sensitive to the choice of integration depth, z_0, particularly north of the Polar Front, where the amplitude increases and the date of the maximum heat content is delayed as integration depth increases. This is a result of heat mixing more deeply north of the Polar Front than south.

Although we found reasonable agreement between seasonal cycles in upper-

ocean heat content and heat fluxes, the simple 1-D heat budget employed in this study may not be a complete picture of the processes governing upper-ocean variability. Horizontal advection, whether zonal advection by the mean ACC flow or meridional Ekman transport, is likely to be an important component of a full upper-ocean heat budget. Particularly north of the Polar Front, advection of eddies through Drake Passage may represent a large but transient departure from the seasonal cycles of upper-ocean heat content we have calculated here. These processes will be important to consider in constructing a more complete understanding of the upper-ocean response to air-sea fluxes.

We have shown that upper-ocean heat content can be a useful measure of the effects of air-sea heat flux forcing and may be more suitable for this purpose than MLD. One of the attractions of using MLD in studies of the Southern Ocean is the ability to couple remote-sensing observations of SST to an upper-ocean heat budget. As *in situ* data in the Southern Ocean become more widely available, the need for this proxy measurement of MLD that remotely-sensed SST provides may be reduced. With the advent of Argo profiling floats, for example, there are now a few thousand profiles collected each year in the Southern Ocean, offering the prospect to observe the impact of upper-ocean heating and cooling directly.

Table 2.1: The annual mean net heat fluxes computed from NCEP, J-OFURO, and OAFlux heat flux products, averaged over gridpoints north (56-59° S) and south (59-62° S) of the climatological position of the Polar Front in the longitude range 60-64° W. A least-squares fit to a sinusoid with period 365.25 days gives the amplitude and phase of the annual cycle. One-sigma uncertainties were computed by multiplying the error estimates from the least-squares fitting procedure by the standard deviation of the heat flux values. A Monte-Carlo method with N=10^5 was used to calculate the uncertainty on the date of maximum amplitude.

Heat Flux Product	Region	Annual Mean Q_{net} (W m^{-2})	Amplitude of cycle (W m^{-2})	Date of max. amplitude
NCEP	North of PF	29.5±1.6	130±3.2	25 Dec. ±1 day
	South of PF	31.7±1.6	131±3.2	24 Dec. ±1 day
J-OFURO	North of PF	22.1±1.8	131±3.6	27 Dec. ±1 day
	South of PF	41.6±1.9	127±3.7	25 Dec. ±1 day
OAFlux	North of PF	39.4±1.7	137±3.4	25 Dec. ±1 day
	South of PF	56.3±1.9	131±3.8	22 Dec. ±1 day

Table 2.2: Characteristics of MLD and heat content are described by region (north or south of the Polar Front) and season (winter or summer). The average difference in MLD defined using temperature and density criteria (MLD_T-MLD_ρ) was computed from XCTD casts. Δ MLD_T and Δ MLD_ρ are the average changes in calculated MLD in response to a 10% change in the thresholds used to calculate MLD with temperature (MLD_T) and density (MLD_ρ), respectively. The uncertainties represent one standard error. Cast-to-cast $\Delta\mathcal{H}_{ML}$ and $\Delta\mathcal{H}_{400}$ are the RMS differences in mixed-layer heat content and heat content over 400 m depth respectively, over pairs of casts collected less than 1 hour (about 10 km) apart. N is the number of cast-pairs used to compute $\Delta\mathcal{H}_{ML}$ and $\Delta\mathcal{H}_{400}$.

Region	Season	MLD_T-MLD_ρ	Δ MLD_T	Δ MLD_ρ	RMS cast-to-cast $\Delta\mathcal{H}_{ML}$ (GJ m^{-2})(N)	RMS cast-to-cast $\Delta\mathcal{H}_{400}$ (GJ m^{-2})(N)
North of PF	Summer	13±2 m	2.4±0.6 m	3.0±1.1 m	0.56 (609)	0.12 (609)
	Winter	48±7 m	7.1±1.5 m	8.2±2.2 m	1.99 (429)	0.16 (429)
South of PF	Summer	6±2 m	1.8±0.4 m	2.4±0.6 m	0.36 (643)	0.12 (643)
	Winter	34±5 m	4.0±0.8 m	5.2±1.3 m	0.95 (560)	0.20 (560)

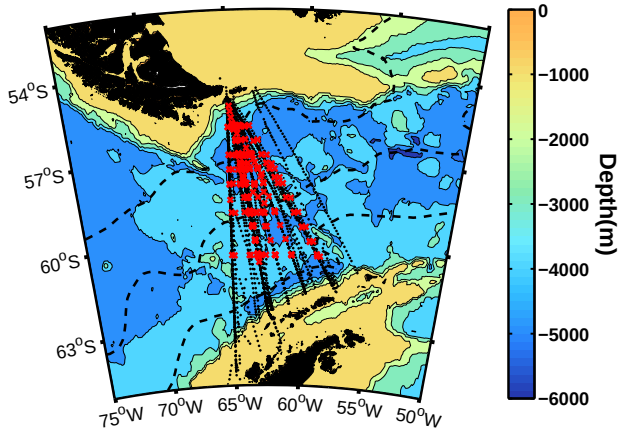

Figure 2.1: Map of Drake Passage showing the locations of the XBT (black dots) and XCTD (red Xs) casts. The climatological mean frontal positions (Orsi et al., 1995) of (from north to south) the Subantarctic Front, Polar Front, and Southern Antarctic Circumpolar Current Front are indicated (dashed lines).

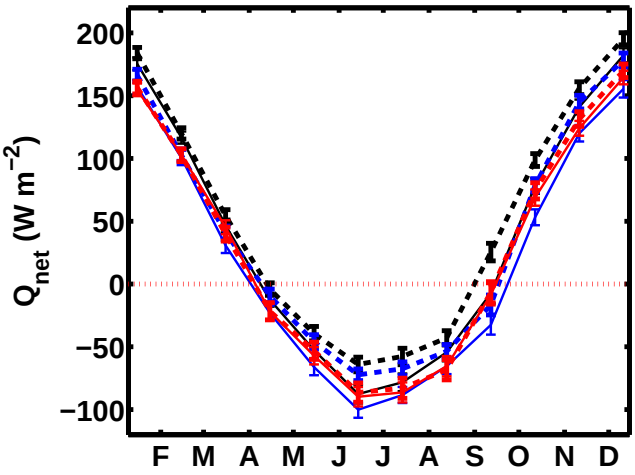

Figure 2.2: Monthly heat flux climatologies for NCEP (red), J-OFURO (blue), and OAFlux (black) over regions north (solid line) and south (dashed line) of the climatological position of the Polar Front. Vertical lines indicate the two-sigma standard error of a 30-day average.

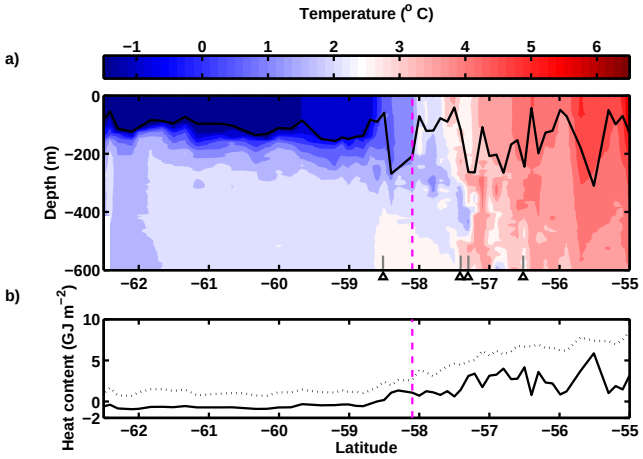

Figure 2.3: (a) A section of temperature (°C) from XBT casts during a Drake Passage transect 18-23 September 2009. The position of the Polar Front is indicated by the dashed magenta line. Mixed-layer depth (MLD) is indicated by the black line. The latitude of example casts in Figures 2.4 and 2.5 are also indicated (triangles). (b) Mixed-layer heat content (solid black) and heat content integrated to 400 m (dashed line) for XBT casts from the transect in (a).

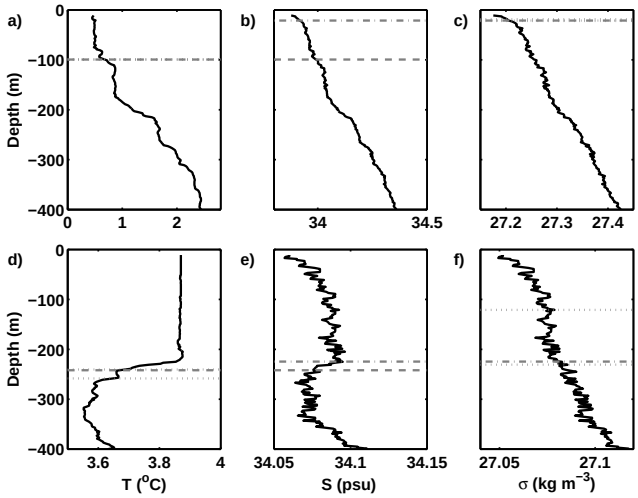

Figure 2.4: Profiles from XCTD casts collected during the transect shown in Figure 2.3 on 20 September 2009 (a,b,c) near 58.5° S, 63.7° W and on 19 September 2009 (d,e,f) near 56.5° S, 64.1° W. Profiles show temperature (°C, a, d), salinity (psu, b, e), and potential density (kg m^{-3}, c, f). MLD_T is shown by the dashed line (a,b,d,e) and MLD_ρ is shown by the dash-dot lines (b,c,e,f). Dotted lines show differences in MLD_T (a,d) and MLD_ρ (c,f) after ΔT and $\Delta\rho$ are changed by $\pm 10\%$, respectively. In panels (a) and (c), these lines lie very close to the dashed line indicating MLD_T. Note also that the x-axis scale is different for the upper and lower panels.

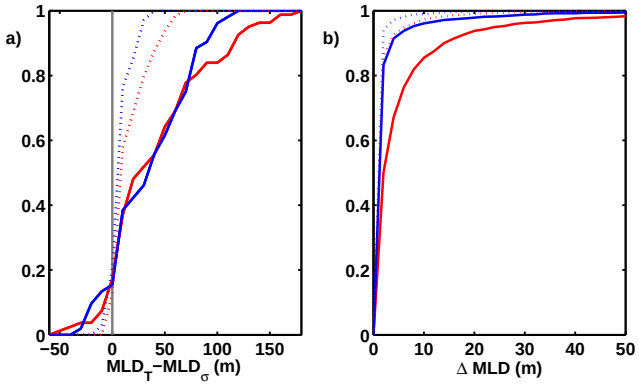

Figure 2.5: (a) Cumulative distribution functions (CDFs) of the difference between MLD_T and MLD_ρ (i.e. MLD_T-MLD_ρ) and (b) CDFs of the change in MLD_T in response to a $\pm$ 10% perturbation to ΔT for XCTD casts collected in winter (solid line) and summer (dotted line), north (red) or south (blue) of the Polar Front.

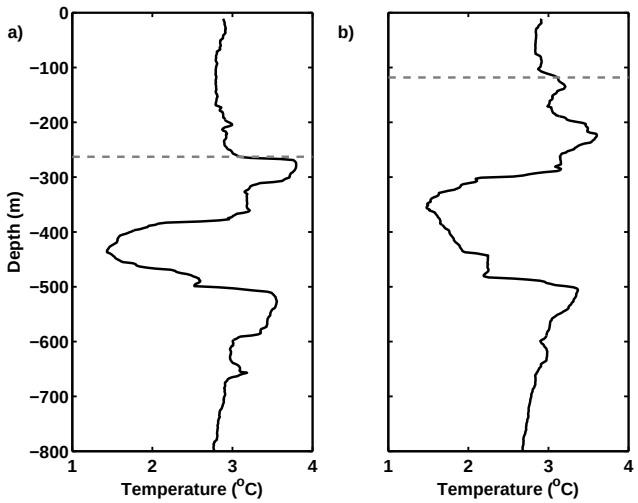

Figure 2.6: Temperature (°C) profiles with depth (m) taken 10 km and less than one hour apart at (a) 57.4° S and (b) 57.3° S near 64.0° W, 19 September 2009, during the transect illustrated in Figure 2.2. Mixed-layer depths (MLD_T, gray dashed line) of (a) 263 m and (b) 118 m were determined using a 0.2° C temperature threshold.

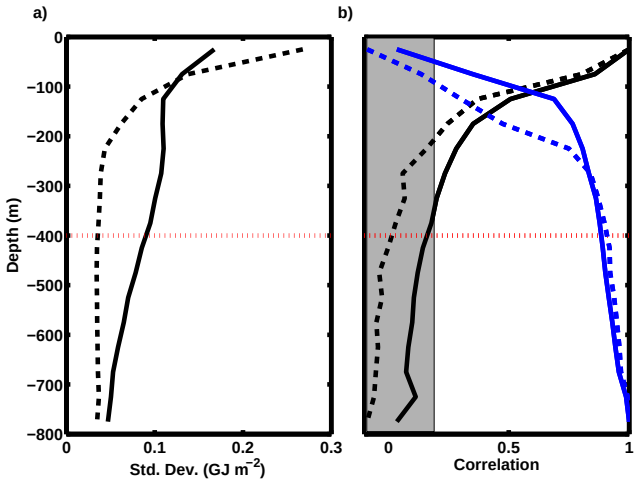

Figure 2.7: (a) Standard deviation of heat content in 50-m layers north (solid) and south (dashed) of the Polar Front. (b) The correlation of heat content in the shallowest layer (0-50 m, black) and in the deepest layer (750-800 m, blue) with heat content in other layers north (solid) and south (dashed) of the Polar Front. The gray bar indicates correlations that are not significant and the red dotted line delineates 400 m depth.

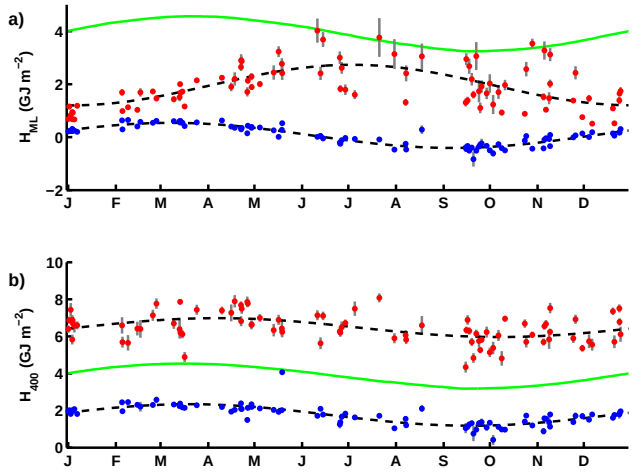

Figure 2.8: (a) $\overline{\mathcal{H}_{ML}}$, mean heat content over the mixed layer and (b) $\overline{\mathcal{H}_{400}}$, heat content in the upper 400 m of the water column for casts north (red) and south (blue) of the Polar Front for 85 XBT transects are plotted against the median year-day of the cruise. Error bars (gray) represent the standard error of the mean. A sinusoidal annual cycle (dashed lines) is least-squares fit to each timeseries. Surface heat fluxes drive an annual cycle in heat content (green line, offset by 4 GJ m^{-2}) made by integrating daily net heat flux anomalies (annual mean removed) from NCEP.

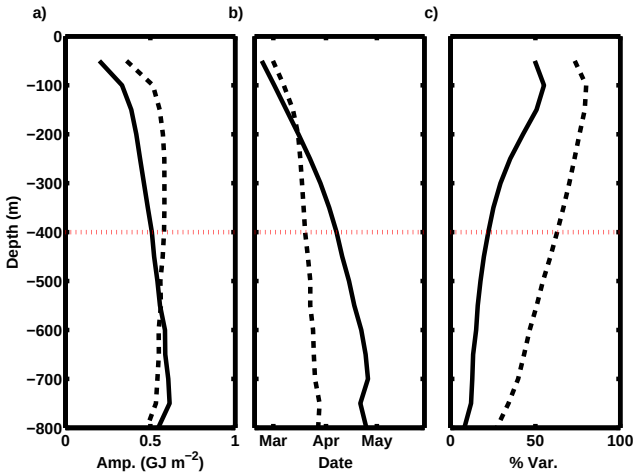

Figure 2.9: (a) Amplitude and (b) phase of a sinusoidal annual cycle fit to $\overline{\mathcal{H}_{z_0}}$ north (solid) and south (dashed) of the Polar Front for values of z_0 ranging from 50 to 800 m in 50 m increments. (c) The fraction of the variance in $\overline{\mathcal{H}_{z_0}}$ explained by an annual cycle in heat fluxes. The red dotted line indicates 400 m depth.

2.7 Acknowledgments

Data collection and analysis for this project was funded by NSF grants to STG (ARRA OCE08050350) and JS (ANT0943818) and a NASA grant to STG (NNX08AI82G). GRS would like to acknowledge a NASA Earth and Space Science Fellowship and the ARCS Foundation for their support. STG acknowledges sabbatical support from the French Centre National de la Recherche Scientifique.

Chapter 2, in full, is a reprint with no modifications to content of the article as it appears in Journal of Geophysical Research-Oceans, 2012, G.R. Stephenson Jr., S.T. Gille, and J. Sprintall, reproduced with permission of American Geophysical Union. The dissertation author was the primary researcher and author of this manuscript. Janet Sprintall provided the XBT/XCTD data and directed and supervised the research along with Sarah Gille.

Chapter 3

Interannual variability of upper-ocean heat content in Drake Passage

3.1 Abstract

A 16-year record of expendable bathythermograph (XBT) transects across Drake Passage is used to examine interannual variability in upper ocean heat content. The response of upper ocean heat content to anomalous heat fluxes, winds, two large-scale climate indices, and mesoscale eddies and meanders is examined. Results suggest that interannual variations in surface heat fluxes explain ∼5-10% of the variability in upper-ocean heat content. Anomalous surface heat fluxes are linked to meridional wind anomalies upstream of Drake Passage, which in turn are linked to forcing by El Niño / Southern Oscillation (ENSO) and the Southern Annular Mode (SAM). ENSO and SAM are correlated with upper ocean heat content at near-zero lags, although relationships at longer time scales are also evident. Interannual variability in upper ocean heat content due to mesoscale eddies and meanders is explored using a tracked eddy database. An empirical relationship is constructed relating upper ocean heat content anomalies to eddy length scales and amplitudes. Eddies and meanders are estimated to account for more than one third of the interannual variability in upper-ocean heat content in Drake Passage.

3.2 Introduction

In recent decades, the Southern Ocean has undergone significant warming (e.g., Gille, 2008). Although heat uptake by the Southern Ocean may retard projected increases in global atmospheric temperatures over the next century (Boé et al., 2009), an increase in sea water temperatures near the Antarctic continent will also contribute to increased ice sheet melting and accelerated sea level rise (Jacobs et al., 2011). More frequent positive El Niño / Southern Oscillation (ENSO) events in recent decades (Kwok and Comiso, 2002) and a positive shift in the index of the Southern Annular Mode (SAM) (Thompson and Wallace, 2000) have fueled inquiries into the mechanisms that link large-scale atmospheric forcing to Southern Ocean warming (e.g., Turner, 2004; Meredith et al., 2008; Ciasto and England, 2011).

The mechanisms by which ENSO and the SAM affect the upper-ocean are

complex and inter-related. SAM appears to be the major mode of atmospheric variability in the Southern Ocean and manifests itself as a strengthening of the meridional pressure gradient around Antarctica (Thompson and Wallace, 2000). With this increase in the sea level pressure gradient comes an intensification and poleward shift of the circumpolar winds (Hall and Visbeck, 2002). ENSO-derived changes in sea surface temperature (SST) anomalies in the tropical Pacific lead to atmospheric Rossby wave trains that propagate poleward as alternating cyclonic and anticyclonic (atmospheric) eddies (Turner, 2004; Meredith et al., 2008). These atmospheric waves affect zonal and meridional surface winds and cloud cover, and thereby influence surface heat fluxes over the Antarctic Circumpolar Current (ACC). These result in cold SST anomalies near Drake Passage and a warm SST anomaly ∼5000 km upstream (Meredith et al., 2008). Advection of the upstream anomalies leads to a positive SST anomaly in Drake Passage ∼2 years later (Meredith et al., 2008). Coupled anomalies in cloud cover, wind, SST, and sea ice concentration have been associated with the Antarctic Circumpolar Wave (ACW), an eastward propagating mode 2 wave in the ACC seen in data from 1985-1994 (White and Peterson, 1996), and the Antarctic Dipole (ADP), a mode of heightened contrast between the southeast Pacific and the southwest Atlantic (Yuan and Martinson, 2000). It has been suggested that the ACW and ADP, when they occur, may be partly driven by ENSO variability (Yuan and Martinson, 2000; Peterson and White, 1998).

To some extent, ENSO and SAM also covary; ENSO explains ∼25% of the variance of SAM in austral summer (L'Heureux and Thompson, 2006). The response of the ocean to forcing by ENSO and SAM occurs at many timescales and varies geographically. The general response to a positive SAM is a poleward shift in the position of the fronts of the ACC as a result of the corresponding poleward shift in the wind (e.g., Hall and Visbeck, 2002; Sallée et al., 2008). In the southeast Pacific, however, increased Ekman pumping and northward transport of cold, fresh water associated with the shift in circumpolar winds leads to a northward shift in the location of the fronts of the ACC during positive SAM (Sen Gupta and England, 2006; Sallée et al., 2008). In the same region, a positive ENSO index

(El Niño conditions) is associated with a poleward displacement of ACC fronts (Sallée et al., 2008). Observations suggest that eddy kinetic energy (EKE) in the ACC responds to the SAM and ENSO after a 1-3 year lag, albeit with a response that varies regionally (Morrow et al., 2010). Positive SAM index leads to an increase in EKE in the south Pacific after a 2-3 year lag (Morrow et al., 2010). Negative ENSO (La Niña conditions) tend to increase EKE after a 1-2 year lag, while positive ENSO decreases EKE after a 1-2 year lag (Morrow et al., 2010). The increased EKE may result in increased meridional heat transport (e.g., Böning et al., 2008), potentially of sufficient magnitude to account for the observed warming of the Southern Ocean (Hogg et al., 2008). Such changes in the Southern Ocean meridional transport have global effects, as forcing by the SAM may alter the strength of the meridional overturning circulation on decadal timescales (e.g., Sijp and England, 2009; Marini et al., 2011).

To discern the response of the upper ocean to atmospheric forcing, an account must be made of the variability already present in the upper ocean. On intraseasonal timescales, mesoscale eddies and meanders of the fronts of the ACC are an energetic perturbation to the mean ocean state. In addition to their role in the poleward transport of heat across the ACC fronts (Böning et al., 2008), eddies alter local air-sea heat fluxes (Jiang et al., 2011), and may influence primary productivity by causing local upwelling or downwelling (Chelton et al., 2011a, e.g.,).

In this study, we identify the effects of ENSO and SAM on upper ocean heat content and evaluate the importance of these two modes of atmospheric forcing to the overall variability in heat content of the ocean. Other processes are likely to be equally important. We focus on the Drake Passage as an ideal location to study the effect of ENSO and the SAM on the upper ocean, as heat content anomalies in the south Pacific must pass through Drake Passage to reach the other ocean basins. Previous work has shown that in Drake Passage a good one-dimensional balance between heat fluxes and upper ocean heat content exists on seasonal time scales; seasonal surface heat fluxes explain $\sim$24% of the variance in upper-ocean heat content north of the Polar Front and $\sim$63% of the variance in upper-ocean heat content south of the Polar Front (Stephenson et al., 2012). It is unclear how

well this balance will hold on interannual time scales, since meanders of the ACC fronts and advection of eddies are likely to be significant contributors to upper ocean variability in the Drake Passage region (Sprintall, 2003; Lenn et al., 2007; Sprintall, 2008). The goal of this study is to assess the relative contributions of each of these sources of interannual variability to the upper-ocean in Drake Passage. Section 3.3 describes the data sets used in this work. In Section 3.4, we review the characteristics of upper-ocean temperature variability in Drake Passage and define and describe upper-ocean heat content anomalies. In Section 3.5, the temporal and spatial scales relating atmospheric variability and climate forcing to heat content anomalies are determined using linear correlations at various time lags. Section 3.6 addresses upper-ocean variability due to eddies and frontal meanders identified in the Chelton et al. (2011b) tracked eddy database. In Section 3.7, we estimate the relative contributions of heat fluxes, meanders and eddies, and forcing by ENSO and the SAM to interannual upper ocean heat content variability. Section 3.8 summarizes our findings and presents our conclusions.

3.3 Data

3.3.1 Temperature transects

The heat content of the upper several hundred meters of the water column is examined using temperature transects from the Scripps High Resolution expendable bathythermograph / expendable conductivity, temperature, depth (XBT/XCTD) program. Since September 1996, operations on the ASRV L. M. Gould have included underway deployment of XBTs on 6-7 Drake Passage crossings each year (Fig. 3.1). XBT transects across Drake Passage have been performed in all seasons, since the use of expendable devices makes routine hydrographic measurements possible even in adverse weather conditions without unduly impacting normal ship operations. Each transect takes 2-3 days, during which ∼70 XBTs are deployed at 10-15 km spacing, or 6-10 km spacing across the Subantarctic and Polar Fronts. The Polar Front is defined here as the northward extent of the 2 °C isotherm at 200 m depth (Orsi et al., 1995). XBT probes typically return temperature profiles

to their rated depth of 850 m. The fall-rate correction of Hanawa et al. (1995) has been applied to each profile, and profiles are averaged to 2 m vertical resolution. Between September 1996 and August 2011, 99 transects were collected. Of these, three transects terminated north of 60^oS (September 1997, February 1998, and July 1999) and three transects deviated significantly from the typical crossings shown in Figure 3.1 (September 1999, June 2000, and January 2009). Data from these cruises have been excluded from our analysis. For each of the remaining 93 transects, temperature fields from the XBTs have been objectively mapped onto a regular grid with 10 m vertical resolution and 0.1^o latitude horizontal spacing (Sprintall, 2003).

3.3.2 Eddy database

Sea surface height fields can be used to identify mesoscale eddies. The simplest methods involve identifying constant contours of sea surface height (e.g., Sprintall, 2003; Fang and Morrow, 2003) or calculating Okubo-Weiss parameters (e.g., Isern-Fontanet et al., 2003). In this study, we use the database of eddies identified in weekly, gridded AVISO SSH fields by Chelton et al. (2011b). Their algorithm uses a range of thresholds to search a map of SSH anomaly for eddies with areas between 8 and 1000 pixels containing a local maximum or minimum, with amplitude of at least 1 cm. This algorithm for eddy identification differs from prior methods in that no thresholds (of SSH or other parameters) need be specified since a wide range of possible values are searched and the SSH fields do not need to be smoothed or differentiated. Eddy-like features are tracked from one weekly SSH field to the next; only those features lasting at least 4 weeks are included in the database.

The database includes information about eddies such as their center latitude and longitude, effective length scale and amplitude. The boundary of an eddy is identified as the location of the maximum current averaged along a contour. The area of the bounded region is calculated and the "effective length scale" of the eddy is reported as the radius of a circle whose area equals the bounded area. Amplitude is given by difference between the sea surface height anomaly at the

center of the eddy and the sea surface height anomaly at the boundary (Chelton et al., 2011b). Thus, cyclonic (cold-core) eddies have a negative amplitude, and anti-cyclonic (warm-core) eddies have a positive amplitude. The eddies in the Chelton et al. (2011b) database were identified using AVISO fields from October 1992 through January 2011, providing information about eddies in all but the three most recent cruises we examined. To identify XBT transects that intersected eddies, we interpolated eddy positions and properties (length scale and amplitude) linearly in time to match the median date of the XBT transect. We determined that an eddy was sampled if the distance from the eddy center to one or more XBT casts was less than the eddy's effective length scale.

3.3.3 Heat fluxes and wind fields

Stephenson et al. (2012) examined three heat flux products in Drake Passage–NCEP-NCAR Reanalysis 1 heat fluxes (Kalnay et al., 1996), Objectively Analyzed fluxes (Yu and Weller, 2007), and Japanese Ocean Fluxes with Use of Remote-sensing Observations (Kubota et al., 2002)–and found them to be similar on seasonal timescales. For this study, we employed NCEP-NCAR Reanalysis 1 heat fluxes, a daily, gridded product with resolution $\sim$1.9° x 1.9° sampled over 1 January 1996 - 31 December 2011, as this heat flux product overlaps the entire time span of the XBT transect time series. Heat fluxes in the vicinity of Drake Passage (270-305^{o}E, 54-65^{o}S) were smoothed with a 60-day running mean. Heat flux anomalies were computed relative to a daily climatology of fluxes at each gridpoint.

Interannual variability in wind forcing was explored using wind fields from the same NCEP-NCAR Reanalysis 1 fields (Kalnay et al., 1996). The 10-m zonal and meridional components of the wind were smoothed with a 60-day Loess filter. Wind anomalies were computed relative to a daily climatology at each gridpoint.

3.3.4 Climate indices

To examine the influence of major modes of climate variability, we used lagged correlations of upper-ocean heat content with climate indices. We use a

monthly, multivariate ENSO index based on principal component analysis of six observed variables in the tropical Pacific (Wolter and Timlin, 1998): sea-level pressure, two components of surface wind, sea surface temperature, surface air temperature, and cloud fraction. For the SAM index we use the monthly values based on zonally-averaged sea level pressure differences between 40^{o}S and 70^{o}S (Nan and Li, 2003).

3.4 Upper-ocean heat content

Drake Passage is a dynamically active region where transport of ∼140 Sv (Cunningham et al., 2003; Firing et al., 2011) passes through a 700 km wide gap. The strong flow is accompanied by strong temperature gradients at the ACC fronts (Orsi et al., 1995; Sokolov and Rintoul, 2009). The Subantarctic Front, Polar Front, and southern ACC Front, divide Drake Passage into regions with very different temperature and density stratification (Orsi et al., 1995; Sprintall, 2003). South of the Polar Front, cold Antarctic Surface Water (AASW) lies above a warmer, more saline Circumpolar Deep Water (CDW) (Figure 3.2a,b). North of the Polar Front, temperature stratification is much lower, with near-vertical isotherms possible to depths >800 m (Figure 3.2a,b).

The upper ocean heat content is a useful measure for understanding upper-ocean variability (e.g., Willis et al., 2004; Stephenson et al., 2012). In this study, we define upper-ocean heat content over the upper 400 m of the water column of a single profile, h_{400}, as

$$h_{400} = \int_{-400}^{0} \rho_0 c_p T(z) dz, \tag{3.1}$$

where $\rho_0 = 1030$ kg m^{-3} is the density of seawater, $c_p = 3985$ J kg m^{-3} is the heat capacity of seawater, and $T(z)$ is the temperature at depth z. The choice of 400 m as an integration depth is motivated by the following considerations: first, temperature variations are small below 400 m south of the Polar Front; second, while more variability is present below 400 m north of the Polar Front, temperature changes at 400 m were strongly correlated with changes down to 800 m, so most of the variability in upper-ocean heat content can be understood by considering h_{400}

(Stephenson et al., 2012).

Two winter (June) transects illustrate year-to-year variability in h_{400} in the region. In the first transect, sampled 10-12 June 2006 (Figure 3.2a), the Polar Front is found at 58.3^{o}S. In the second transect, sampled 28-30 June 2009 (Figure 3.2b), the Polar Front is located ∼50 km farther south at 58.8^{o}S. The minimum temperature of the AASW is ∼0.8^{o}C colder in 2009 than in 2006. The June 2009 transect also shows relatively cool 3-4^{o}C water at ∼56-57^{o}S latitude, north of the Polar Front. The temperature changes across the Polar Front have a strong signal in h_{400} (Figure 3.2c,d). The cool anomaly in the June 2009 transect appears as a local minimum at 56.5^{o}S (Figure 3.2d). This cool feature is likely associated with a cold-core eddy centered at (56^{o}S, 63^{o}W) just east of the June 2009 XBT transect (Figure 3.2f). Alternatively, the warm tempertures near 57-58°S may be associated with the warm-core feature centered near 58°S, 64°W. Both transects pass near or intersect cyclonic (cold-core) and anti-cyclonic (warm-core) mesoscale features. The effects of eddies on heat content variability will be discussed in Section 3.6.

Stephenson et al. (2012) separately considered averages of h_{400} over measurements collected north of the Polar Front, $\mathcal{H}_N$, and south of the Polar Front, $\mathcal{H}_S$ (e.g., Figure 3.2c,d). In this study, we consider h_{400} averaged over an entire transect across Drake Passage, denoting the transect-averaged quantity by the upper-case $\mathcal{H}_{400}$ to distinguish transect-averaged heat content from the single-profile values, h_{400}, used in Section 3.6 to examine mesoscale variability. We partition variability in $\mathcal{H}_{400}$ into changes in $\mathcal{H}_N$ and $\mathcal{H}_S$ and shifts in the latitude of the Polar Front. A northward shift in the Polar Front, for example, increases the amount of cold water present in Drake Passage, but does not necessarily imply a change in properties of the water masses that define the Polar Front. By partitioning variability this way, we can estimate how much heat content variability is due to water masses warming or cooling and how much is due to poleward shifts in the locations of fronts. A simple expression relates $\mathcal{H}_{400}$ to $\mathcal{H}_N$, $\mathcal{H}_S$, and the position of the Polar Front:

$$\mathcal{H}_{400} = \mathcal{H}_N \frac{\phi_N - \phi_{PF}}{\phi_N - \phi_S} + \mathcal{H}_S \frac{\phi_{PF} - \phi_S}{\phi_N - \phi_S} \tag{3.2}$$

where ϕ_N and ϕ_S are the northernmost and southernmost latitudes of the transect,

and ϕ_{PF} is the latitude of the Polar Front. The northern endpoint of the transects is roughly constant at 54.5^{o}S, since the L.M. Gould always departs from and returns to Punta Arenas, Chile. The southern endpoint, ϕ_S, varies depending on the ship's specific destination in Antarctica (Figure 3.1). To limit variation in ϕ_N and ϕ_S, we have restricted the latitude range of data considered in this study to between 54.5^{o}S and 62.5^{o}S; small variations in ϕ_S and ϕ_N occur where transects are terminated within this range. For the 93 Drake Passage transects, $\mathcal{H}_N$, $\mathcal{H}_S$, and ϕ_{PF} (as in equation 3.2) each contribute roughly one third of the variability in $\mathcal{H}_{400}$ (Table 3.1).

To define heat content anomalies associated with interannual variability, we remove a seasonal cycle from the transect-averaged heat content (Figure 3.3). A least-squares fit was made to annual and semi-annual harmonics; this fit explained $\sim$50% of the variability in $\mathcal{H}_{400}$. Similarly constructed fits explain $\sim$30% and $\sim$70% of the variability in $\mathcal{H}_N$ and $\mathcal{H}_S$, respectively (Table 3.1). The residuals left when seasonal cycles are removed are denoted $\mathcal{H}'_{400}$ (Fig. 3.3), $\mathcal{H}'_N$, and $\mathcal{H}'_S$. We note that $\mathcal{H}'_S$ has a standard deviation (0.37 GJ m^{-2}) half as large as that of $\mathcal{H}'_N$ (0.68 GJ m^{-2}). Movements of the Polar Front explain $\sim$34% of the interannual variability in $\mathcal{H}'_{400}$, whereas $\mathcal{H}'_N$ explains $\sim$26% of the variance in $\mathcal{H}'_{400}$ and $\mathcal{H}_S$ explains only 9% of the variance in $\mathcal{H}'_{400}$ (Table 3.1). This implies that on interannual timescales changes in water temperature south of the Polar Front contribute less to the overall variability of upper ocean heat content in Drake Passage than shifts in the Polar Front location and changes in heat content north of the Polar Front.

3.5 Variability due to atmospheric forcing

Atmosphere-ocean interactions at the sea surface are a primary driver of upper-ocean variability. On seasonal timescales, upper-ocean heat content appears to be governed by surface heat flux forcing (Stephenson et al., 2012). Interannual variability in surface heat fluxes is also expected to have a direct influence on upper-ocean heat content. This section examines contributions to interannual

upper-ocean heat content variability arising from changes in surface heat input, and links heat flux anomalies to meridional wind anomalies upstream of Drake Passage. Finally, we examine the response of $\mathcal{H}'_{400}$ to large-scale forcing using linear correlations with the ENSO and SAM indices.

Heat fluxes represent a time rate of change of upper-ocean heat content. The change in ocean heat content resulting from surface heat fluxes, $\Delta\mathcal{H}$, can be expressed as a simple time integral

$$\Delta\mathcal{H} = \int_{t_1}^{t_2} Q'_{net}\, dt \tag{3.3}$$

from time t_1 to t_2, where Q'_{net} is the net surface heat flux anomaly defined in Section 3.3.3. This is a simplified expression. In a strong current, such as the ACC, heat anomalies due to local surface heat fluxes are advected downstream, affecting heat content downstream at a time offset that depends on the distance and speed of the advection. Furthermore, since $\Delta\mathcal{H}$ has no explicit depth scale, and vertical mixing within the water column may distribute heat flux input to depths deeper than 400 m, the relationship between Q'_{net} and $\mathcal{H}'_{400}$ may be weakened. Therefore, this calculation requires careful consideration of the horizontal, vertical, and temporal scales over which a signal is likely to persist. Nontheless, prior work suggests that more than 75% of the upper-ocean thermal variability occurs above 400 m depth (Stephenson et al., 2012).

To determine where heat flux anomalies contribute most to heat content in Drake Passage, we constructed a map of the correlation between $\mathcal{H}'_{400}$ and Q'_{net} at points in and upstream of Drake Passage over a range of time offsets. The maximum correlation was found for Q'_{net} at 60^{o}S, 289^{o}E at a time offset of 75 days (i.e., heat flux anomalies 75 days prior to a transect, Q_{75d}) (r =0.42, Fig. 3.5a). In fact, at this location lagged correlations of Q'_{net} with $\mathcal{H}'_{400}$ have significant positive correlations spanning a range of time offsets from 55-80 days (Fig. 3.5b). At these time offsets, significant positive correlations cover a large area upstream (from ∼58-64^{o}S, 277-300^{o}E) of Drake Passage (Fig. 3.5a). This correlation pattern is consistent with downstream advection, and we conclude that this correlation is not overly sensitive to the time offset or location. The regression coefficient between heat fluxes at 60^{o}S, 289^{o}E and $\mathcal{H}'_{400}$ is 7.6±4.6×10^{-3} GJ W^{-1} (significant

with 99% confidence); this is equivalent to the heat accumulated by a constant 1 W m^{-2} heat flux over a time period of 88±53 days, or roughly 3±2 months. Typical values of Q'_{net} are closer to O(20 W m^{-2}), which lead to heat content anomalies of O(0.15 GJ m^{-2}) using the regression coefficient.

Two other peaks are evident in the lagged correlations at 35 and 185 days (Figure 3.5b). At a 35-day offset, the region of maximum positive correlation extends from ∼59-62^{o}S, 288-291^{o}E (not shown); at a 185-day offset, it is centered around 62^{o}S, 285^{o}E (not shown). The westward shift in the location of maximum correlation at greater time offsets is consistent with the idea that upstream heat content anomalies associated with more distant heat fluxes require more time to be advected into Drake Passage.

Heat flux anomalies are negatively correlated with meridional wind anomalies, with stronger correlations centered over the Polar Front ($r \sim -0.6$, Figure 3.6a). One interpretion of this anticorrelation is that positive wind anomalies tend to move cold air northward where it encounters warmer surface water, while negative wind anomalies tend to move warm air southward over cooler surface water. Regression coefficients of Q'_{net} onto meridional wind anomaly are also largest over the ACC, with magnitudes of 8.0±0.4 to 10.0±0.5 W m^{-2} per m s^{-1} near the Polar Front (Figure 3.6b). A change of 0.5 ^{o}C in air temperature would be sufficient to explain this regression coefficient; with an air temperature of 2 ^{o}C, SST of 4 ^{o}C, wind speeds of 1 m s^{-1} and 100% relative humidity, a 0.5 ^{o}C change in the air-sea temperature difference results in a change in sensible heat fluxes at the sea surface of ∼5 W m^{-2} and a change in latent heat fluxes of ∼ 4 W m^{-2}. These estimates are consistent with observations of turbulent heat fluxes in Drake Passage (Jiang et al., 2011).

Meridional wind anomalies and heat flux anomalies are two mechanisms by which ENSO and SAM variability is imprinted on SST (e.g., Meredith et al., 2008; Naveira Garabato et al., 2009; Ciasto and England, 2011). We find weak but statistically significant correlations between the ENSO index and meridional wind anomalies at 60^{o}S, 289^{o}E (where $\mathcal{H}'_{400}$ and Q'_{net} were maximally correlated) at 0 months lag (r =0.31); maximum correlations between the ENSO index and Q'_{net} at

the same location occur with Q'_{net} leading ENSO index by ∼6 months ($r = -0.19$). At the same location, maximum correlations with the SAM index were found with Q'_{net} leading the SAM by 2 months (r =0.17) and with meridional wind anomalies leading the SAM by 1 month (r =0.20).

To observe the oceanic response to general forcing by ENSO and SAM, we calculated lagged correlations of the ENSO and SAM indices with $\mathcal{H}'_{400}$, ϕ_{PF}, $\mathcal{H}'_N$, and $\mathcal{H}'_S$ (Figure 3.7) at time offsets from -6 months to +6 years. To accommodate the irregular temporal sampling of the XBT transects, we linearly interpolated the monthly ENSO and SAM indices so as to keep the time offset from the date of the XBT transects constant for each correlation. Positive lags indicate that a transect occurs after the climate index.

The strongest correlations with ENSO occur when $\mathcal{H}'_{400}$ leads the ENSO index by 1-3 months (r =-0.45, Fig. 3.7a). At this time lag, El Niño is associated with cooling of $\mathcal{H}'_{400}$, a northward shift of the Polar Front, and cooling of $\mathcal{H}'_S$ (Fig. 3.7). Similarly, La Niña is associated with warming of $\mathcal{H}'_{400}$, a southward shift of the Polar Front, and warming of $\mathcal{H}'_S$ (Fig. 3.7). This relationship may be explained by anomalous heat flux input upstream of Drake Passage. Recall that Q'_{net} at 60^{o}S, 289^{o}E leads the ENSO index by 6 months; if the resulting heat content anomalies require 2-3 months (∼75 days) to reach Drake Passage, we would expect a signal in $\mathcal{H}'_{400}$ that leads the ENSO index by 3-4 months. The time scale of this response also shows good agreement with results by Meredith et al. (2008); they found a negative response of SST near South Georgia Island, ∼1500 km east of Drake Passage, at a lag of 5 months, but estimated that SST anomalies advected by the ACC would require 5-6 months to reach South Georgia Island from the western Antarctic Peninsula. We also find significant correlations at time lags of 4.5 years (54 months), when ENSO and $\mathcal{H}'_{400}$ are negatively correlated (r =-0.27), ENSO and ϕ_{PF} are positively correlated (r =0.31) and ENSO and $\mathcal{H}'_N$ are negatively correlated (r =-0.24). Meredith et al. (2008) found a negative correlation of South Georgia SST with ENSO at a lag of 60 months. So if the signal from ENSO is advected to South Georgia from Drake Passage in 5-6 months, a minimum in the correlation of Drake Passage heat content with ENSO would be

expected at 54 months lag, consistent with what we observe. At a time lag of 10-11 months, ENSO and $\mathcal{H}'_{400}$ are positively correlated (r =0.24, Fig. 3.7a), as are ENSO and $\mathcal{H}'_N$ (r =0.26, Fig. 3.7c). The mechanism responsible for the time scale of this correlation is not clear. The atmospheric Rossby waves associated with ENSO are thought to imprint an SST anomaly in the south Pacific, but advection of this anomaly from the south Pacific to Drake Passage is expected to take ∼2 years (Meredith et al., 2008). South of the Polar Front, upper ocean heat content responds to ENSO on a different time scale. Correlations of $\mathcal{H}'_S$ with ENSO have a peak at a lag of ∼3 years (r =0.27), when correlations of ENSO with $\mathcal{H}'_{400}$, ϕ_{PF} and $\mathcal{H}'_N$ are not significant. This response is slower than the expected ∼2 years (Trathan and Murphy, 2002; Meredith et al., 2008); positive correlations between ENSO and $\mathcal{H}'_S$ at a 3-year lag are consistent with a similar response of Winter Water layer temperatures to ENSO at 3-year lag (Sprintall, 2008). The response of $\mathcal{H}'_S$ to forcing by ENSO may be mediated by interactions between the upper ocean and sea-ice, as sea-ice extent near the western Antarctic Peninsula is positively correlated with ENSO forcing at lags of 18-30 months (Yuan and Martinson, 2000), comparable to the ∼3 year response of $\mathcal{H}'_S$.

The response of $\mathcal{H}'_{400}$ to forcing by the SAM occurs at two timescales (Fig. 3.7). Near zero lag, positive correlations occur when $\mathcal{H}'_{400}$ leads the SAM by 1 month (r =0.22) or lags the SAM by 3 months (r =0.22). The maximum correlation of the SAM with $\mathcal{H}'_N$ occurs when $\mathcal{H}'_N$ leads the SAM by 1-5 months, with warm anomalies in $\mathcal{H}'_N$ being associated with a positive SAM and cold anomalies being associated with a negative SAM (r =0.27). These responses may be driven by heat fluxes or meridional wind anomalies associated with the SAM. The positive response of $\mathcal{H}'_{400}$ and $\mathcal{H}'_N$ to the SAM on short timescales mirror similar relationships between the SAM and SST (e.g., Kwok and Comiso, 2002; Liu et al., 2004) and between the SAM and temperatures at depths of 0 to 400 m north of the Polar Front (Sprintall, 2008). A second response to the SAM is seen at a lag of ∼38 months, when correlations with $\mathcal{H}'_{400}$ and $\mathcal{H}'_N$ are negative (r =-0.23 and r =-0.24, respectively) and correlation with ϕ_{PF} is positive (r =0.20), corresponding to a northward movement of the Polar Front in response to a positive SAM

index 38 months prior or a southward movement of the Polar Front in response to a negative SAM index 38 months prior. At a lag of 2 years, Sprintall (2008) found that the SAM was associated with cooler near-surface temperatures north of the Polar Front. One expected response to the SAM is an increase in EKE (Morrow et al., 2010) and meridional heat transport (Hogg et al., 2008). Negative correlations of $\mathcal{H}'_{400}$ and $\mathcal{H}'_N$ with the SAM at this lag are consistent with this possibility; increased EKE can lead to upwelling north of the Polar Front and an increase in the northward transport of Winter Water / Antarctic Intermediate Water (Naveira Garabato et al., 2009). Both processes are compatible with cooling north of the Polar Front. The response of heat content south of the Polar Front occurs at shorter time lags; our results show peaks in the correlations of the SAM with $\mathcal{H}'_S$ at lags of 6 months (r =0.27) and 18-24 months (r =0.40). Warm anomalies in $\mathcal{H}'_S$ may result from increased upwelling of warm upper Circumpolar Deep Water in response to increased zonal wind stress associated with the SAM. Several studies have also emphasized the importance of interactions between atmospheric forcing, sea-ice extent along the western Antarctic Peninsula, and resulting changes to the upper ocean (e.g., Yuan and Martinson, 2000; Meredith et al., 2008; Sprintall, 2008; Naveira Garabato et al., 2009). A positive SAM index has been linked to increased rates of sea-ice growth in the Pacific sector at lags of 0 and 1 year (Holland et al., 2005); interaction of sea-ice with the upper ocean south of the Polar Front may explain the presence of two peaks one year apart in the correlation of the SAM with $\mathcal{H}'_S$. A one year time scale may also results from the "memory" effect of heat content (Alexander and Deser, 1995; Deser et al., 2003), in which temperature anomalies below the mixed layer persist from one winter to the next.

3.6 Variability due to eddies and meanders

As in other regions of the Southern Ocean, upper ocean variability in Drake Passage at interannual time scales is dominated by mesoscale eddies and meanders of the fronts of the ACC (Sprintall, 2003, 2008). However, the degree to which

the Southern Ocean is eddy-saturated, and hence the response of meridional heat transport in the ACC to changing ENSO and SAM remains a subject of inquiry (e.g., Böning et al., 2008; Hogg et al., 2008). The goal of this section is to quantify the interannual heat content anomalies associated with mesoscale eddies and meanders of the Polar Front in Drake Passage. We first construct composite cold-core and warm-core eddies from eddies identified in a tracked eddy database and sampled by the XBT transects, then we determine the mesoscale anomalies in heat content associated with an eddy. Finally, we calculate the contribution of eddies and meanders to variability in $\mathcal{H}'_{400}$. Because the Chelton et al. (2011b) database is derived from sea surface height anomalies, it does not distinguish between transient eddies and frontal meanders, so for the purposes of this study, we treat eddies and meanders identically. A southward meander of the Polar Front, for example, appears as a large positive anomaly in sea surface height and has a positive effect on the heat content similar to a warm-core eddy.

To examine the mesoscale variability in upper-ocean heat content associated with eddies, we calculated the spatially-varying heat content, h_{400} (equation 3.1), and formed anomalies relative to a seasonal cycle and a meridionally-varying mean. The meridional mean was constructed by averaging at each 0.1° latitude point over all 93 objectively-mapped temperature transects, not only the 90 transects coinciding with the period of the Chelton et al. (2011b) eddy database. For points located north of the Polar Front, the seasonal cycle corresponding to $\mathcal{H}_N$ was removed; for points south of the Polar Front, a seasonal cycle in $\mathcal{H}_S$ was removed. The resulting field of spatially-varying upper ocean heat content anomalies (henceforth h'_{400}) differs from the regional averages discussed in Section 3.4 and 3.5. Indeed, h'_{400} shows considerable mesoscale activity, with strong anomalies near the latitude of the Polar Front (Figure 3.8a).

To identify mesoscale features associated with eddies and meanders, we classified a transect as crossing or intersecting an eddy where the distance from the eddy center to a point in the transect (d, as illustrated in Fig. 3.8b) is less than the length scale (R, as shown in Fig. 3.8b) associated with the eddy in the Chelton et al. (2011b) database. Most of the XBT transects crossed at least one

eddy (Figure 3.2, Figure 3.8a), with a total of 95 warm-core and 90 cold-core eddies sampled. Two distinct bands of eddy activity are noted: one band located between 56^oS and 59.5^oS and another cluster near 61^oS (Figure 3.8a). The largest, most intense eddies occur near or to the north of the Polar Front, while eddies south of the Polar Front are smaller and have lower amplitude (Table 3.2). These results agree with measurements in Drake Passage that show greater EKE north of the Polar Front than south (Lenn et al., 2007); this is thought to indicate that mesoscale features are more frequent and intense north of the Polar Front than south.

Eddies and meanders contribute significantly to regional variations in upper ocean heat content. The net effects of warm- or cold-core eddies on upper ocean heat content were evaluated by averaging values of $\mathcal{H}'_{400}$, $\mathcal{H}'_N$, $\mathcal{H}'_S$ over six categories of transects: transects that intersected any warm-core eddies, any cold-core eddies, warm-core eddies north of the Polar Front, warm-core eddies south of the Polar Front, cold-core eddies north of the Polar Front or cold-core eddies south of the Polar Front (Table 3.3). There is some overlap between the set of transects used to compute averages in each column. For example, transects that intersected both warm- and cold-core eddies contribute to the averages in the warm-core total and cold-core total columns in Table 3.3. On average, transects that intersected any warm-core eddy showed a slight increase in $\mathcal{H}'_N$. Transects that intersected warm-core eddies north of the Polar Front exhibit significant increases in $\mathcal{H}'_{400}$, a southward displacement of the Polar Front, and an increase in $\mathcal{H}'_N$ (Table 3.3).By contrast, transects that intersected a warm-core eddy south of the Polar Front were associated with cool anomalies in $\mathcal{H}'_{400}$ and $\mathcal{H}'_N$ but did not show significant differences in $\mathcal{H}'_S$ or $\Delta\phi_{PF}$ (Table 3.3). The difference in response may reflect differences in the number, size, and types of eddies intersected north as opposed to south of the Polar Front. Warm-core eddies south of the Polar Front are fewer, smaller and lower in amplitude than warm-core eddies north of the Polar Front (Table 3.2), and so may not contribute to significant warming. Transects in which cold-core eddies are intersected south of the Polar Front show overall cooling of $\mathcal{H}'_{400}$ and a northward shift in ϕ_{PF}. When cold-core eddies are encountered north

of the Polar Front, they decrease $\mathcal{H}'_N$ but do not have a significant impact on $\mathcal{H}'_{400}$; they also result in a southward displacement of the Polar Front and a slight warming of $\mathcal{H}'_S$ (Table 3.3).

Although we can not explicitly distinguish between eddies and meanders in our identification criteria, we expect that they will have different effects on $\mathcal{H}'_N$ and $\mathcal{H}'_S$. Southward (warm) meanders of the Polar Front may be included in our analysis as warm-core eddies located north of the Polar Front, while northward (cold) meanders of the Polar Front may be classed with cold-core eddies located south of the Polar Front. In Section 3.4, we showed that while meanders of the Polar Front are strongly linked to changes in $\mathcal{H}'_{400}$, they are not significantly correlated with changes in $\mathcal{H}'_N$ or $\mathcal{H}'_S$ (Table 3.1). Similar results are shown in Table 3.3; significant changes in $\mathcal{H}'_{400}$ are evident in the averages that include potential meanders (warm-core north of the Polar Front or cold-core south of the Polar Front), while transects that include cold-core eddies north of the Polar Front show a large decrease in $\mathcal{H}'_N$ but do not have a significant effect on $\mathcal{H}'_{400}$ (Table 3.3).

The spatial structure of typical eddies is examined by the construction of composite eddies. To make composite cold-core and warm-core eddies, we calculated zonal and meridional displacement of XBT casts from the centers of nearby eddies, with distances normalized by the length scale of the eddy. In total, $\sim$200 measurements were collected within 1 eddy radius of the center. Heat content anomalies were binned by distance (bin sizes of 0.5$\times$R) and direction (60° bins) from the center of the eddy to the measurement location, with cold-core and warm-core eddies considered separately (Fig. 3.9). The resulting composites show that the eddy length scale is a good scaling to describe heat content variations associated with mesoscale eddies; most of the cold or warm anomaly is contained within a circle of radius equal to the eddy length scale (Figure 3.9).

Eddies appear to be rotationally and east-west asymmetric. In the composite cold-core eddy, a cold anomaly of -0.29$\pm$0.10 GJ m^{-2} per cm eddy amplitude is concentrated on the west side of the composite eddy, but a warm anomaly is found along the eddy's eastern edge (Figure 3.9a). The warm-core composite eddy has a smaller peak temperature anomaly, 0.14$\pm$0.03 GJ m^{-2} per cm and has a

cold anomaly along its western edge (Figure 3.9c). The counterclockwise spiral of the cool temperatures at the edge of the warm-core eddy is consistent with anti-cyclonic movement in the Southern Hemisphere (Figure 3.9c). The warm anomaly along the edge of the cold-core eddy (and similarly the cold anomaly at the edge of the warm-core eddy) gives the composite eddy a dipole structure. Although the standard error in the mean heat content anomaly is large for some bins, portions of the dipole shape appear to be significant at 2 standard errors in both the cold- and warm-core eddies (Fig. 3.9b and 3.9d, respectively). Chelton et al. (2011a) noted a similar structure in ocean color maps of composite eddies. They suggest that the chlorophyll *a* dipole may result from effects of advection due to clockwise rotation around the cold eddy core or counterclockwise advection around a warm eddy core or that the dipole may indicate local upwelling induced by eddy pumping.

In order to estimate the net contribution of eddies to upper-ocean heat content, we consider a simplified model of a rotationally-symmetric eddy where h'_{400} is a function, $f(r, A)$, of the distance from the eddy center, r, and the eddy amplitude, A. We normalized h'_{400} by the (signed) amplitude, A, of the eddy and normalized distance from the eddy center by the length-scale of the eddy, R. The mean and median values of h'_{400}/A were computed over bins of width $0.2 \times R$ (Figure 3.10a). The mean normalized heat content anomaly decreases from a peak of 0.12±0.02 GJ m^{-2} in the interior of an eddy to 0.03±0.02 GJ m^{-2} at a distance equal to the eddy length scale. The median heat content anomaly crosses zero at a distance of $\sim 1.3 \times R$ from the eddy center. We approximate these curves by a truncated Gaussian given by the expression

$$f(r, A) = 0.15A \left(2e^{-r^2/2R^2} - 1\right) \tag{3.4}$$

over distances $|r| < 1.2R$ and zero outside this range (Fig. 3.10a). Because the eddy length-scale is defined by the area bounded by the maximum azimuthally-averaged velocity (see Section 3.3.2) a strong gradient is appropriate at a distance $r = R$ from the eddy center. A coefficient of 0.15 ± 0.02 (99% confidence interval) comes from a linear regression of h'_{400}/A onto $f(r, A)$ (Figure 3.10b). There is good agreement between the functional fit and observed values of h'_{400} (r =0.82, Fig. 3.10b), and results are not critically dependent on the functional form of $f(r, A)$; for example,

assuming a cylindrical eddy with constant amplitude A where $r < R$ also gives a good correlation (r =0.77, not shown).

How realistic are these coefficients relating heat content to eddy amplitude? Thermosteric expansion of seawater contributes significantly to sea surface height variability. For typical conditions in Drake Passage (salinity ∼34 psu, temperature ranging from -1 to 8 ^{o}C), the thermal expansion coefficient, α ≈5-10×10^{-5} ^{o}C^{-1}. A warming of 1 ^{o}C over a water column 400 m deep is equivalent to an increase of 1.6 GJ m^{-2} of heat over a sea surface height increase of ∼2-4 cm; equivalent to h'_{400}/A ≈0.4-0.8 GJ m^{-2} per cm sea surface height anomaly. The peak value of the functional fit in equation (3.4) relating heat content anomaly to eddy amplitude is 0.15 ± 0.02 GJ m^{-2} per cm, ∼20-40% of the value expected due to thermal expansion. The difference can be explained if eddies extend over the upper 1000-2000 m of the water column; this is not implausible, as some Southern Ocean eddies have been classed as "equivalent barotropic," extending nearly top-to-bottom in the ACC (e.g., Firing et al., 2011).

To test the dependence of this regression coefficient on the 400 m depth considered, we performed similar regressions for heat content anomalies calculated over a range of depths between 0 and 600 m, where we denote the heat content anomaly above a depth z_0 by h'_{z_0}. For these regressions, the functional form and length scale representing the eddy were fixed constant while we solved for the amplitude, i.e. the peak value of a functional fit as in in equation (3.4) (see also, Fig. 3.10a). The coefficient relating heat content anomaly to eddy amplitude increases with depth (Fig. 3.11). The increase of h'_{z_0} / A with depth was approximated by an exponential of the form $C_1 \times (1 - e^{z_0/C_2})$. We solved for C_1 = 0.33 GJ m^{-2} cm^{-1} (with a range of 0.29-0.40) and C_2 = 634 m (with a range of 520-830 m) by minimizing the RMS difference between h'_{z_0}/A and the exponential fit. Uncertainty ranges were estimated by considering values of C_1 and C_2 for which the RMS difference between h'_{z_0} / A and the fit were less than 0.023, twice the minimum RMS misfit. These results suggest that the vertical variations of heat content anomalies within an eddy may have an approximate e-folding scale between 520 and 830 m.

Based on the functional fit in equation (3.4), a typical eddy near 57^{o}S with

amplitude 20±1 cm and length scale 85±3 km (Table 3.2) represents a total, area-integrated anomaly of $25 \pm 3 \times 10^{18}$ J in the upper 600 m; a typical eddy near 60^{o}S, with amplitude 10±1 cm and length scale 71±4 km, represents an anomaly of only $9 \pm 2 \times 10^{18}$ J. The contribution of any single eddy to the transect-averaged heat content, $\mathcal{H}_{400}$, is a function not only of the eddy's amplitude and length-scale, but also of the length of the overlap of the transect with the eddy which, in turn, is prescribed by the proximity of the eddy to the transect and the length scale of the eddy. A schematic depicting this relationship is shown in Figure 3.8b. For a circular eddy, the length of the overlap, L, of the transect and the eddy can be expressed as

$$L = 2 \times \sqrt{R^2 - d^2}, \tag{3.5}$$

where R is the length-scale of the eddy, and d is the minimum distance from the eddy to the transect.

The total heat content anomaly associated with sampling a single eddy, h_e, can be expressed as an integral along the portion of the transect that lies within a distance R of the eddy's center (Figure 3.8b):

$$h_e = \int_{-\sqrt{R^2-d^2}}^{\sqrt{R^2-d^2}} f(\sqrt{d^2 + l^2}, A) dl, \tag{3.6}$$

where the integration variable l ranges from $+L/2$ to $-L/2$ (as in equation 3.5). The total heat content anomaly due to eddies and meanders in a transect, $\mathcal{E}$, is the sum of h_e (equation 3.6) along segments where a transect intersects individual eddies divided by the length of the transect. A regression of $\mathcal{E}$ onto $\mathcal{H}'_{400}$ (Fig. 3.12) shows that the amplitude of heat content anomalies due to eddies and meanders closely matches amplitude of the observed heat content anomalies. Variations in $\mathcal{E}$ are also well correlated with $\mathcal{H}'_{400}$ (r =0.604, Table 3.1). The effects of uncertainty in the amplitude of $f(r, A)$ on h_e were modeled as a fixed percentage of the total of ±13% of h_e, based on the uncertainty in the amplitude of the function $f(r, A)$ of ±.02 GJ m^{-2} per cm relative to a value of 0.15 GJ m^{-2} per cm at $r = 0$. We also estimated the sensitivity of h_e to a ±10 km change in d for R ranging from 20 to 90 km and d ranging from 0 to R; this represents uncertainty in the location of the center of the eddy. Averaged over the ∼850 km length of a typical transect,

uncertainty in the eddy position contributes an additional uncertainty in $\mathcal{E}$ of less than 4×10^{-3} GJ m^{-2} per eddy.

3.7 Significant contributors to $\mathcal{H}_{400}$

This study has explored several contributors to interannual variability in upper-ocean heat content in Drake Passage. We estimate the contribution of each factor to the overall variability in $\mathcal{H}'_{400}$ by computing linear regressions between $\mathcal{H}'_{400}$ and several variables: shifts in the latitude at which transects cross the Polar Front (ϕ_{PF}, Section 3.4), heat flux anomalies (Q'_{75d}, Section 3.5), ENSO and SAM (Section 3.5), and heat content anomalies associated with mesoscale eddies and meanders ($\mathcal{E}$, Section 3.6). These variables are not entirely independent of each other; meanders of the Polar Front are represented in both ϕ_{PF} and $\mathcal{E}$, and heat flux anomalies have been linked to both ENSO and SAM. The single best predictor of $\mathcal{H}'_{400}$ is $\mathcal{E}$ (r =0.60), followed by ϕ_{PF} (r =0.55), Q_{75d} (r =0.42), ENSO (r =-0.45), and SAM(r =0.21). Considering several terms together improves the fit; a multiple-linear regression of $\mathcal{H}'_{400}$ onto $\mathcal{E}$ and ϕ_{PF} together gives a much higher correlation (r = 0.70). Including ENSO increases the correlation to 0.78 and including Q_{75d} increases the correlation to 0.80, corresponding to 64% of the variability in $\mathcal{H}'_{400}$ explained by a combination of $\mathcal{E}$, ϕ_{PF}, ENSO, and Q_{75d}. Including the SAM in the regression does not appreciably increase the fraction of variance explained. If we consider upper ocean heat content variability at all time scales, as represented by $\mathcal{H}_{400}$, we find that the weighted sum of five terms ($\mathcal{E}$, ϕ_{PF}, the ENSO index at -45 day lag, Q_{75d} and the seasonal cycle in $\mathcal{H}_{400}$ computed in Section 3.4) is correlated at 0.92 with $\mathcal{H}_{400}$.

3.8 Summary and Conclusions

A 16-year record of temperature transects was used to examine interannual variations in upper ocean heat content in Drake Passage. The oceanic variability present in the form of mesoscale eddies and the response to climate forcing was

found to be different for regions north and south of the Polar Front. Interannual variability in the amount of heat above 400 m depth in Drake Passage was shown to be largely a result of shifts in the location of the Polar Front and changes in heat content north of the Polar Front, with changes in heat content south of the Polar Front making a smaller contribution.

On the >2 month time scales we examined, anomalous heat fluxes are a significant source of interannual variability in upper ocean heat content. In particular, we found a maximum in correlation between $\mathcal{H}'_{400}$ and heat flux anomalies ∼250 km west 2-3 months prior to a transect. Heat flux anomalies appear to be closely related to meridional wind anomalies in the Southern Ocean, as others studies have also noted (e.g., Kwok and Comiso, 2002; Meredith et al., 2008; Naveira Garabato et al., 2009). Atmospheric teleconnections to ENSO and large-scale forcing related to the state of the SAM affect both heat fluxes and wind anomalies, with the result that ENSO and SAM are correlated with heat content at several time offsets. Our results are broadly consistent with other studies that have looked at the effects of ENSO and SAM on Southern Ocean temperatures (Kwok and Comiso, 2002; Liu et al., 2004; Meredith et al., 2008; Sprintall, 2008; Naveira Garabato et al., 2009), although the time lags differ in some cases from these other results. Qualitative differences in ocean forcing associated with individual ENSO events included or excluded from these studies that cover different time periods may explain the range of temporal response scales observed. We find significant correlations between ENSO and $\mathcal{H}'_{400}$ at lags of -1 to -2 months, as well as 10-11 months and 4.5 years; significant correlations are found between the SAM and $\mathcal{H}'_{400}$ at time lags of ∼0 and 3 years. Important differences are seen in the response to ENSO and SAM of upper ocean heat content south of the Polar Front. $\mathcal{H}'_S$ responds to ENSO at ∼0 and 3-year lags and responds to the SAM at 6 month, 18 month, and 4.5 year lags. While the mechanisms responsible for the difference in response north and south of the Polar Front are not clear, interactions of the atmosphere and ocean with sea ice may contribute to the observed regional variation (Yuan and Martinson, 2000; Holland et al., 2005).

Meanders and eddies have been suggested as the dominant source of upper-

ocean variability in Drake Passage (Sprintall, 2003, 2008). Our results support these claims. Sources of mesoscale variability in the form of eddies or meanders were identified using the Chelton et al. (2011b) tracked eddy database. In 90 transects for which a tracked eddy database was available, 95 warm-core and 90 cold-core eddies were sampled by XBTs and composite cold- and warm-core eddies were constructed. The composite pictures of the heat content anomaly of an eddy show a number of well-known features of eddies: rotational and east-west asymmetry, spiral shapes, and warm or cold heat content anomalies near the edge of the eddy with an opposite sense to that of the eddy likely associated with upwelling or advection (Chelton et al., 2011a). A fit was made to the heat content in an eddy as a function of distance from the center; variations in the coefficient associated with this fit suggest that temperature anomalies within a composite eddy are "equivalent barotropic," perhaps extending top-to-bottom in Drake Passage. Based on the functional fit and eddy characteristics from the Chelton et al. (2011b) database, the contribution of eddies and meanders to upper ocean heat content was estimated to be more than one third of the interannual variability.

In total, heat fluxes (seasonal and interannual), meanders, eddies, and ENSO variability explain ∼84% of the variance of heat content in Drake Passage at all timescales, with the largest contributions coming from the seasonal cycle in surface heat fluxes and the variability associated with mesoscale eddies and frontal meanders. ENSO teleconnections have a significant effect on upper ocean heat content, but the response may be only partially explained by ENSO-driven modifications to the surface heat fluxes and meridional wind field. Different physical processes acting north and south of the Polar Front may modulate the time scales of the oceanic response in each region. Further inquiry is needed to better describe the mechanisms by which air-sea-ice interactions govern the oceanic variability we observe in response to climate modes.

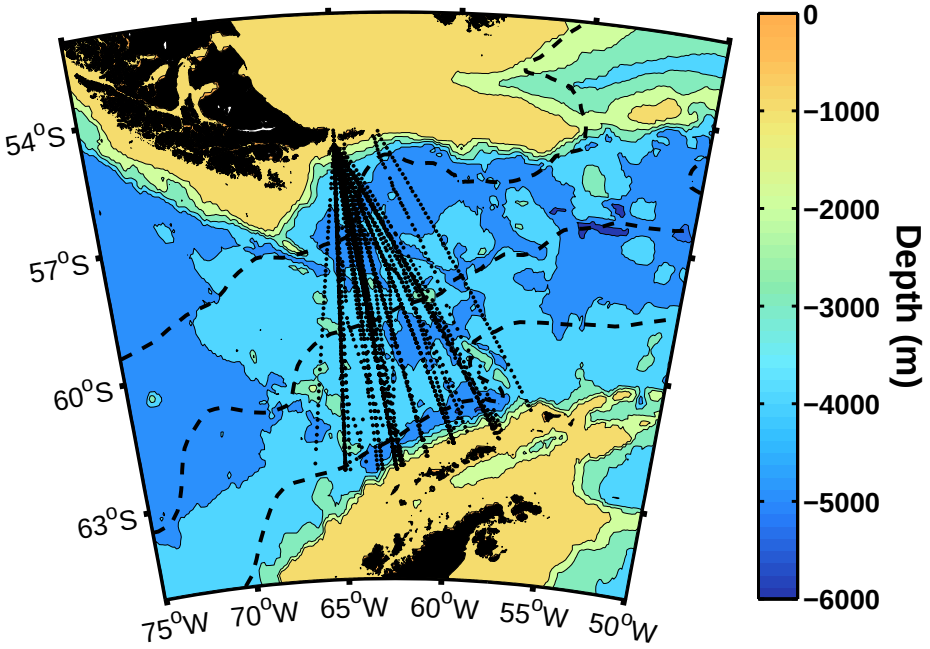

Figure 3.1: Bathymetric map of Drake Passage showing the locations of XBTs (black dots). The climatological mean frontal positions (Orsi et al., 1995) of (from north to south) the Subantarctic Front, Polar Front, and Southern Antarctic Circumpolar Current Front are indicated (dashed lines).

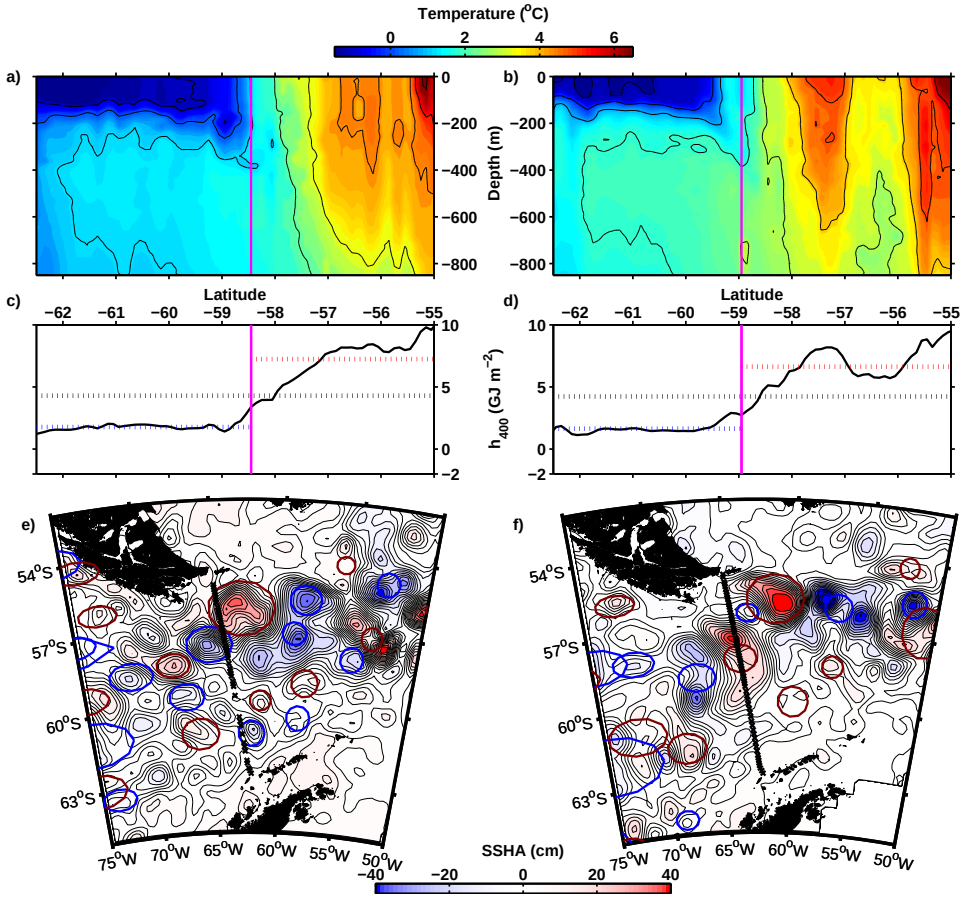

Figure 3.2: Temperature transects from June cruises in (a) 2006 and (b) 2009. Transects of heat content from 0-400 m, h_{400}, across (c) the June 2006 transect and (d) the June 2009 transect with average heat content north of the Polar Front ($\mathcal{H}_N$, red dotted line), south of the Polar Front ($\mathcal{H}_S$, blue dotted line), and over the entire transect ($\mathcal{H}_{400}$, black dotted line). The latitude of the Polar Front is indicated by a magenta line (a,b,c,d). Maps of daily sea surface height anomaly (e) 12 June 2006 and (f) 30 June 2009 and locations of XBT casts (black x). Center location and approximate length scale of cyclonic (blue) and anticyclonic (red) eddies identified in the Chelton et al. (2011b) database. Apparent overlap of eddies may be caused by linear interpolation of eddy position or by approximation of the eddies as circular.

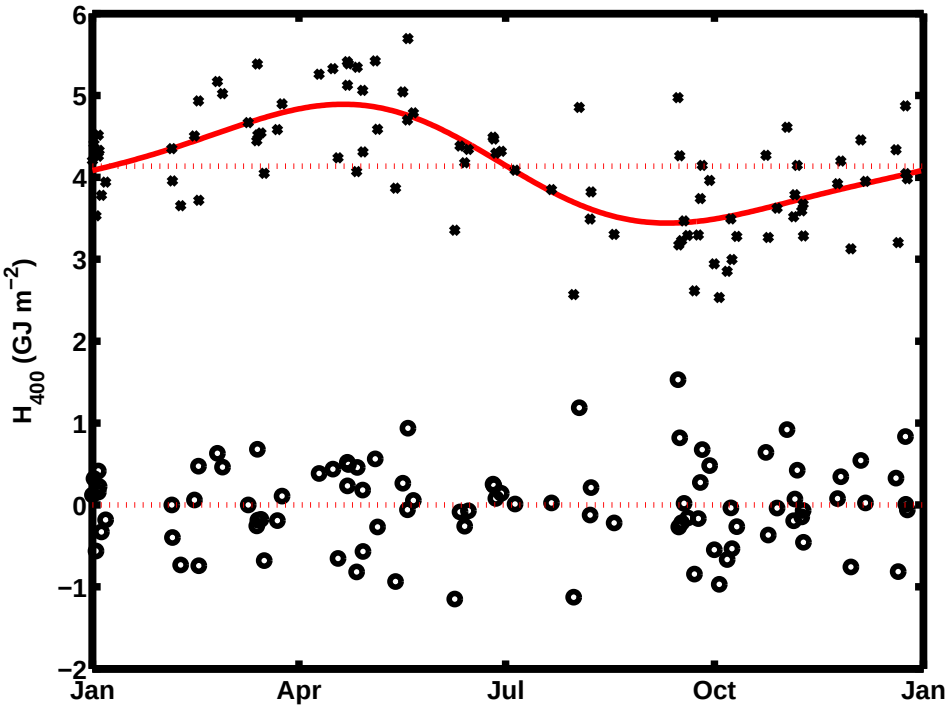

Figure 3.3: Transect-averaged $\mathcal{H}_{400}$ (black x) and an annual cycle fitting an annual and semiannual cycle (red curve). $\mathcal{H}'_{400}$ (black circles) are the residuals relative to the annual cycle.

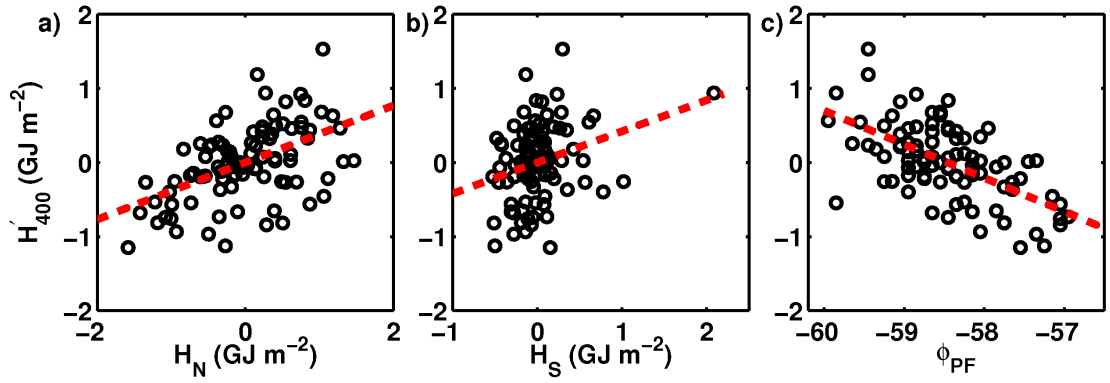

Figure 3.4: Linear regression red (dotted line) of $\mathcal{H}'_{400}$ onto (a) H_N (r =0.506), (b) H_S (r =0.292) and (c) latitude of the Polar Front (ϕ_{PF}, r =-0.599).

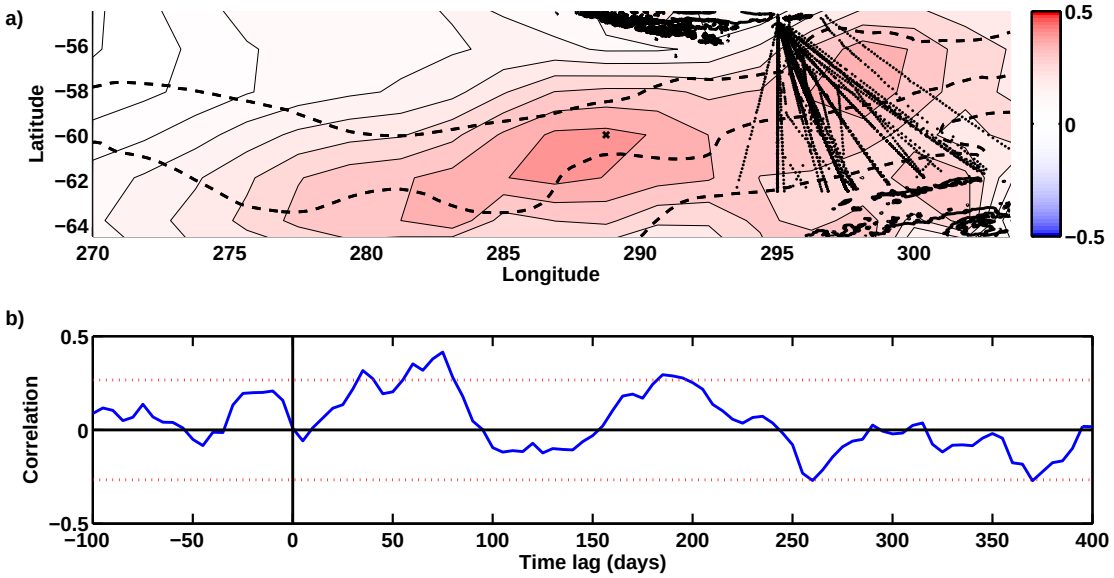

Figure 3.5: (a) A map of the correlation between $\mathcal{H}'_{400}$ and Q'_{net} 75 days prior (Q_{75d}) shows a maximum near 60^{o}S, 289^{o}E. The interval between contours is 0.05. (b) The correlation between Q'_{net} at 60^{o}S, 289^{o}E and $\mathcal{H}'_{400}$ reaches a maximum at $\sim$75 days. Positive time lag indicates Q'_{net} precedes $\mathcal{H}'_{400}$.

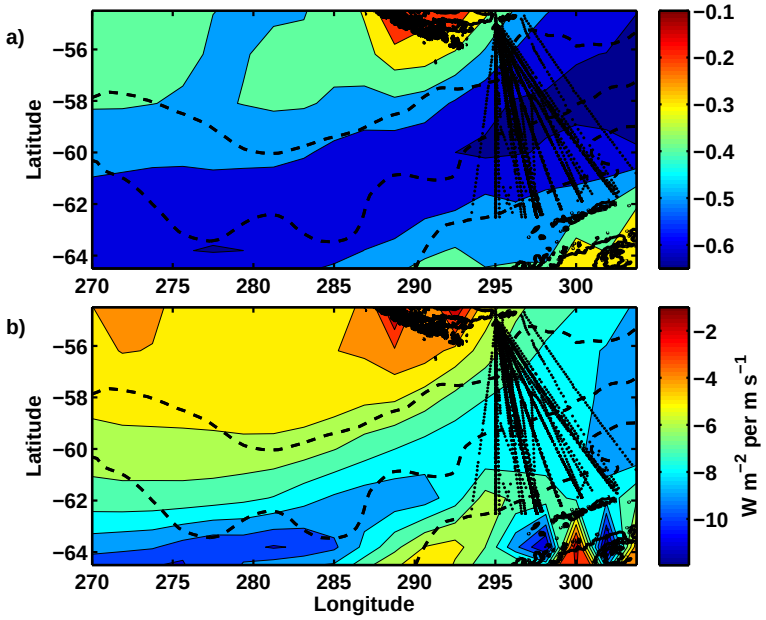

Figure 3.6: (a) Correlation of NCEP Reanalysis 1 heat flux anomalies (Q'_{net}) with meridional wind anomalies. (b) Regression coefficients of Q'_{net} onto meridional wind anomalies. Climatological position of the ACC fronts (dashed lines)are, from north to south, the Subantarctic Front, Polar Front, and southern ACC Front. Locations of XBT casts (black dots) are indicated.

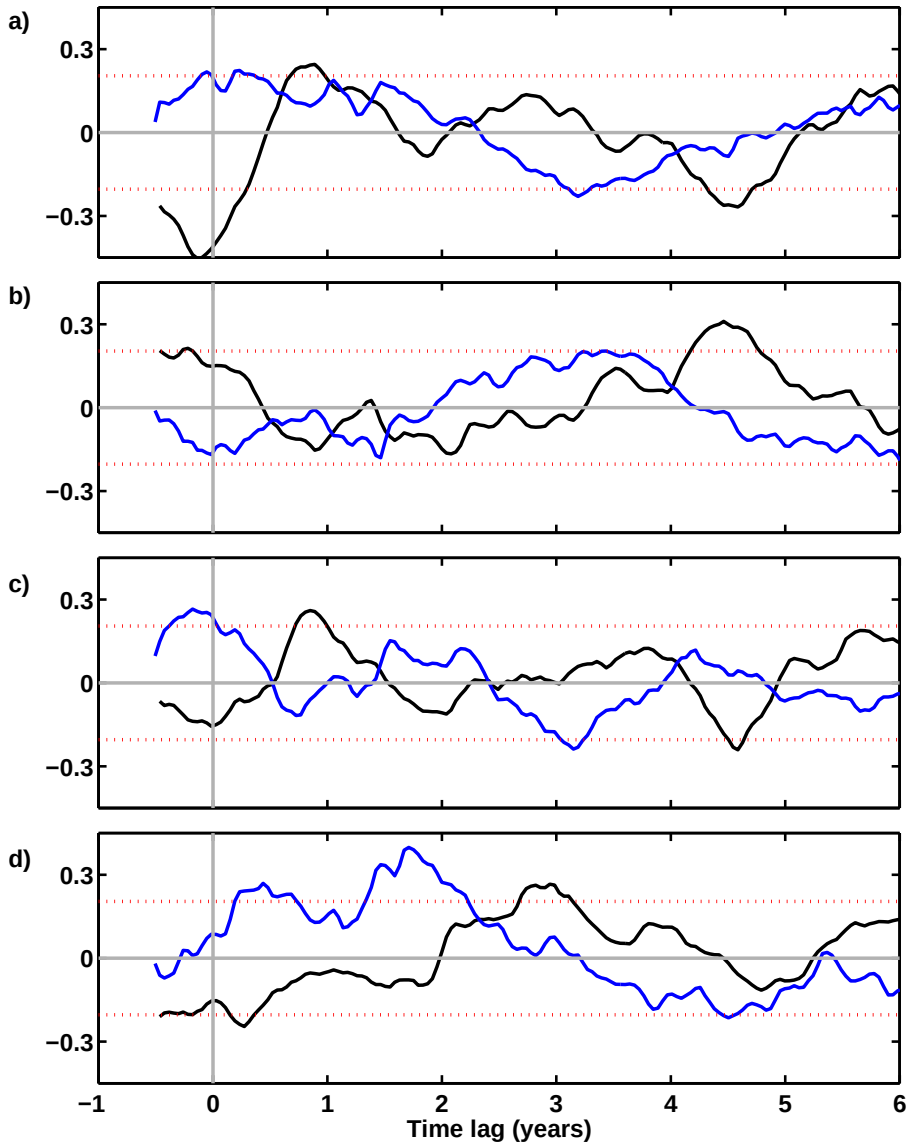

Figure 3.7: Correlations between the ENSO index (black line) or the SAM index (blue line) and (a) $\mathcal{H}'_{400}$, (b)ϕ_{PF}, (c) $\mathcal{H}'_N$, and (d) $\mathcal{H}'_S$. Positive time lags indicate the ENSO or SAM index precedes the XBT transect. Red dotted lines indicate the 0.95 significance level.

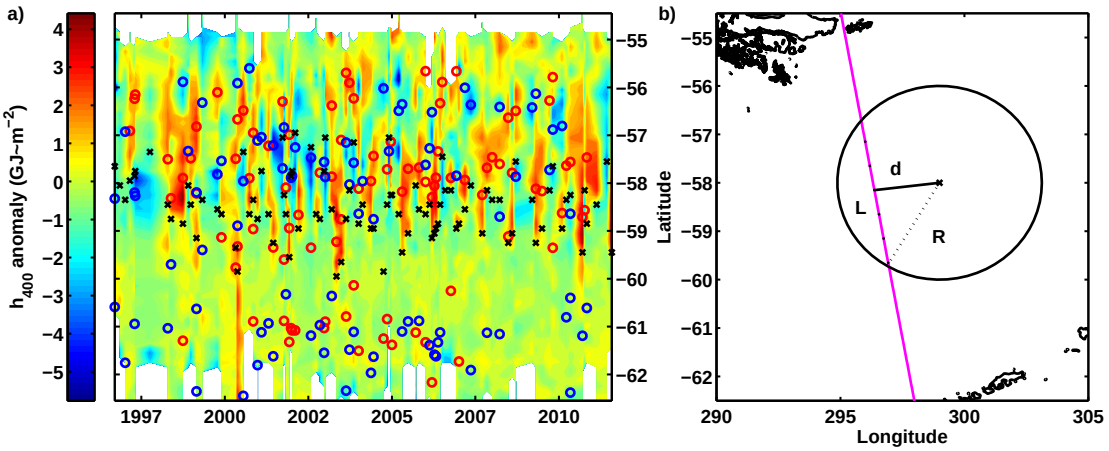

Figure 3.8: (a) Upper-ocean heat content anomalies, h'_{400}, relative to a seasonal cycle and a spatial mean (binned by latitude). The latitude of cold-core (blue circle) and warm-core (red circle) eddies that intersect an XBT transect are indicated, as well as the location of the Polar Front (black x) (b) A schematic depicting determination of the heat content anomaly associated with a transect crossing an eddy, h_e. The length, L, of the intersection between a transect (magenta line) and an eddy (black circle) depends on the minimum distance, d, from the center of the eddy to the transect and the length scale, R, of the eddy.

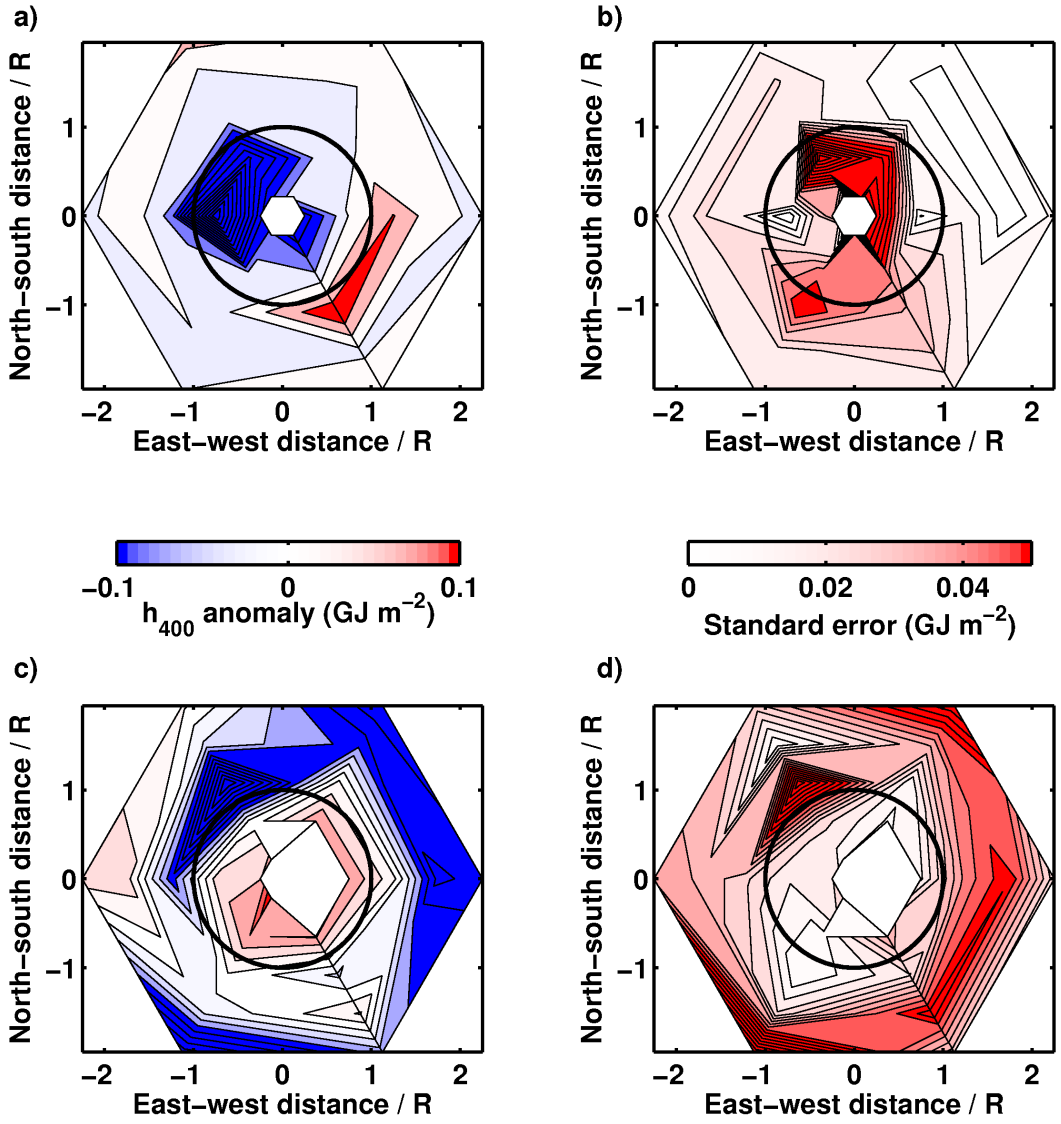

Figure 3.9: Spatial distribution of h'_{400} in (a) a composite cylonic (cold-core) eddy and (c) a composite anticyclonic (warm-core) eddy. For heat content measurements near an eddy, values of h'_{400} were normalized by the eddy's amplitude (units are GJ m^{-2} per cm eddy amplitude) and binned by position relative to the eddy center. Zonal and meridional displacement from the center of the eddy are scaled by the effective length-scale of the eddy. The standard error of the bin average is shown for (b) the cyclonic eddy and (d) the anticyclonic eddy. Contour intervals are 0.05 (a,c) or 0.01 (b,d) GJ m^{-2} per cm.

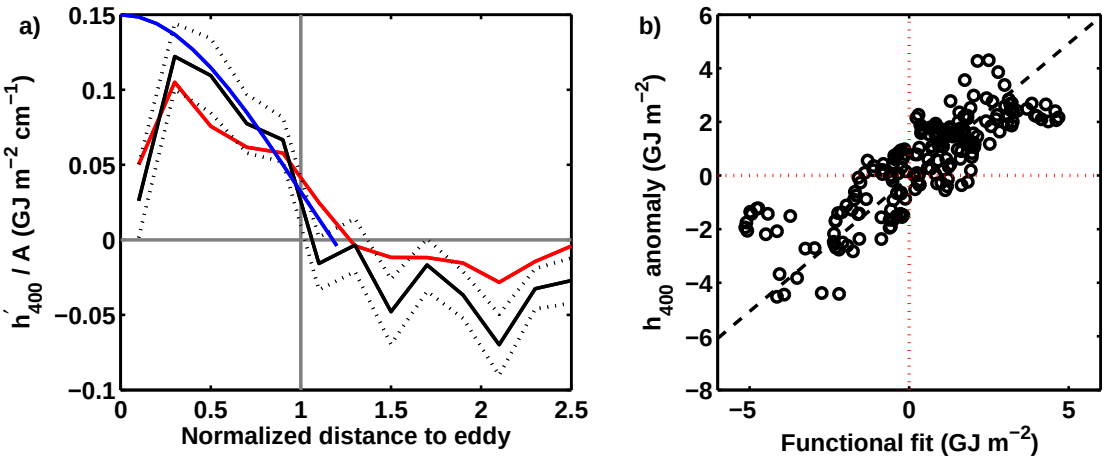

Figure 3.10: (a) The heat content anomaly associated with the eddy is a function of distance from the eddy center and the length scale and amplitude, A, of the eddy. For measurements located within an eddy, h'_{400} was normalized by the amplitude of the eddy; binned averages of h'_{400}/A were computed at d/R ranging from 0.1 to 2. Mean (black line) $\pm$ one standard error (dotted lines) and median (red) h'_{400}/A decrease from maxima near $0.3R$ from the eddy center to 0 at 1 to $1.3R$ from the center. A truncated Gaussian curve (blue line) as in equation (3.4) approximates $f(r, A)$. (b) A scatterplot of h'_{400} against the value of $f(r, A)$ at each measurement point (black circles), with a one-to-one line fit (dashed line).

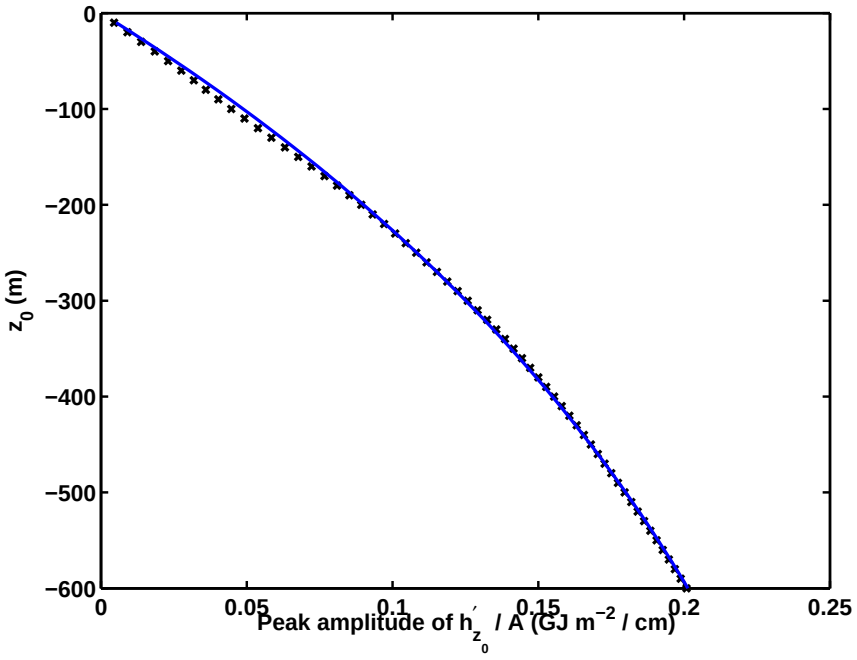

Figure 3.11: Peak amplitude of the functional fit (black x) computed as for Figure 3.10 for depths between 0 and 600 m. The increase with depth is approximated by an exponential curve (blue line) described by $(0.33 \times (1 - e^{z_0/634}))$.

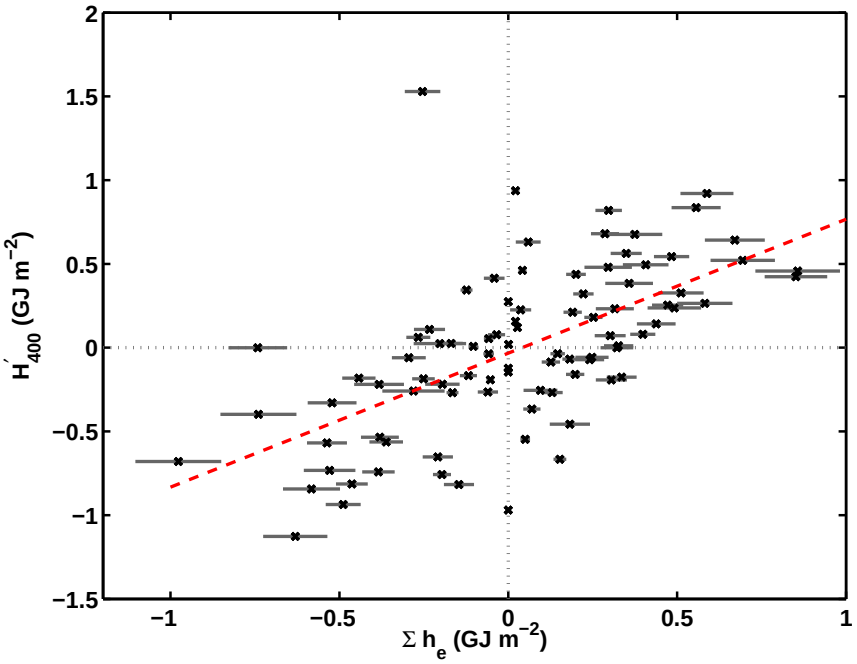

Figure 3.12: A scatterplot of $\mathcal{H}'_{400}$ against the sum of heat content anomalies due to eddies ($\mathcal{E}$). A linear regression (red dashed line) has a slope of 0.80±0.22. Uncertainties in $\mathcal{E}$ (gray lines) are computed as discussed in Section 3.7.

Table 3.1: The upper part of the table shows correlations of the transect-averaged upper-ocean heat content ($\mathcal{H}_{400}$) with average upper-ocean heat content north ($\mathcal{H}_N$) and south ($\mathcal{H}_S$) of the Polar Front and with the latitude of the Polar Front (ϕ_{PF}), as well as the correlation of each variable with a two-harmonic fit to the seasonal cycle in each. The lower part of the table shows correlations of the residual heat content when a seasonal cycle has been removed ($\mathcal{H}'_{400}$, $\mathcal{H}'_N$, $\mathcal{H}'_S$) and ϕ_{PF} with $\mathcal{H}'_{400}$, ϕ_{PF}, the average heat flux anomaly upstream of Drake Passage 75 days prior to a transect (Q_{75d}, defined in Section 3.5) and heat content anomaly due to mesoscale eddies and meanders ($\mathcal{E}$, defined in Section 3.6). Significant correlations appear as bold text.

	$\mathcal{H}_{400}$	$\mathcal{H}_N$	$\mathcal{H}_S$	ϕ_{PF}
$\mathcal{H}_{400}$	1	**0.642**	**0.681**	**-0.591**
seasonal cycle	**0.705**	**0.552**	**0.833**	**.311**
	$\mathcal{H}'_{400}$	$\mathcal{H}'_N$	$\mathcal{H}'_S$	ϕ_{PF}
$\mathcal{H}'_{400}$	1	**0.506**	**0.292**	**-0.599**
ϕ_{PF}	**-.599**	0.037	0.025	1
Q_{75d}	**.416**	0.147	0.101	**-0.213**
$\mathcal{E}$	**0.604**	**0.340**	-0.065	**-0.420**

Table 3.2: Mean properties of eddies from the Chelton et al. (2011b) database intersected by an XBT transect: the number of each type of eddy (N), the average amplitude (A), effective length scale (R) and latitude. Averages are computed over all warm- or cold-core eddies, or over eddies north or south of the Polar Front and ± one standard error is reported for all quantities.

warm core	total	N of PF	S of PF
N	95	57	38
A (cm)	14.4±1.0	18.2±1.2	8.6±1.1
R (km)	79.3±2.3	84.6±2.7	71.3±3.8
Lat. (°S)	58.4±0.2	57.2±0.1	60.0±0.2
cold core	total	N of PF	S of PF
N	90	18	72
A (cm)	-13.1±0.9	-15.8±1.7	-12.4±1.1
R (km)	75.7±2.6	73.4±4.0	76.3±3.0
Lat. (°S)	59.1±0.2	56.7±0.2	59.7±0.2

Table 3.3: Averages of $\mathcal{H}_{400'}$, $\mathcal{H}'_N$, and $\mathcal{H}'_S$ for all transects that intersected warm- or cold-core eddies and for transects that intersected warm- or cold-core eddies north or south of the Polar Front. The displacement of the Polar Front ($\Delta\phi_{PF}$) is computed relative to the mean latitude of the Polar Front (58.5^{o}S) over the 93 XBT transects. Error bounds are one standard error, and bold values are significant at one standard error.

warm core	All	N of PF	S of PF
N	74	60	26
$\mathcal{H}'_{400}$ (GJ m^{-2})	0.06±0.06	**0.15±0.06**	**-0.17±0.09**
$\mathcal{H}'_N$ (GJ m^{-2})	**0.14±0.07**	**0.23±0.08**	**-0.13±0.11**
$\mathcal{H}_{S'}$ (GJ m^{-2})	0.00±0.04	−0.00±0.05	0.04±0.06
$\Delta\phi_{PF}$ (km)	-8±9	**−18±9**	14±17
cold core	All	N of PF	S of PF
N	65	34	45
$\mathcal{H}'_{400}$ (GJ m^{-2})	-0.06±0.06	-0.08±0.08	**-0.10±0.08**
$\mathcal{H}'_N$ (GJ m^{-2})	0.00±0.08	**−0.24±0.11**	0.10±0.10
$\mathcal{H}_{S'}$ (GJ m^{-2})	0.02±0.05	**0.12±0.08**	-0.04±0.05
$\Delta\phi_{PF}$ (km)	5±9	**-20±10**	**20±11**

3.9 Acknowledgments

Data collection and analysis for this project was funded by NSF grants to STG (ARRA OCE08050350) and JS (ANT0943818) and a NASA grant to STG (NNX08AI82G). GRS would like to acknowledge a NASA Earth and Space Science Fellowship and the ARCS Foundation for their support. STG acknowledges sabbatical support from the French Centre National de la Recherche Scientifique. NCEP Reanalysis 1 data were provided by the NOAA/OAR/ESRL PSD, Boulder, Colorado, USA, from their Web site at http://www.esrl.noaa.gov/psd/.

Chapter 3, in full, is a manuscript in preparation for publication. I was the primary researcher and author of this material, with contributions from co-authors Sarah Gille and Janet Sprintall.

Chapter 4

Subsurface melting of a free-floating iceberg in the Weddell Sea

4.1 Abstract

Observations near a large tabular iceberg in the Weddell Sea in March and April 2009 show evidence that water from ice melting below the surface is dispersed in two distinct ways. Warm, salty anomalies in T-S diagrams suggest that water from the permanent thermocline is transported vertically as a result of turbulent entrainment of meltwater at the iceberg's base. Stepped profiles of temperature, salinity, and density in the seasonal thermocline are more characteristic of double-diffusive processes that transfer meltwater horizontally away from the vertical ice face. These processes contribute comparable amounts of meltwater–O(0.1 m^3) to the upper 200 m of a 1 m^2 water column–but only basal melting results in significant upwelling of water from below the Winter Water layer into the seasonal thermocline, suggesting that these two processes may have different effects on vertical nutrient transport near an iceberg.

4.2 Introduction

Calving from glaciers in Antarctica accounts for 2,000 Gt of yearly freshwater input into the Southern Ocean, half of which takes the form of large tabular icebergs (Jacobs et al., 1992). Icebergs with a major axis larger than 10 nautical miles are responsible for most of the transport of freshwater north of 63° S (Silva et al., 2006). Drifting icebergs redistribute heat and freshwater and transport trace metals (Smith et al., 2007). Their effects on surface temperature and salinity alter local stratification and may affect rates of sea-ice formation and Antarctic Bottom Water formation (Jongma et al., 2009). Because icebergs tend to follow well-defined tracks determined by prevailing winds and currents, they have enhanced impacts on specific regions (Jenkins, 1999). For example, in regions with high iceberg concentrations, such as the Weddell Sea, iceberg meltwater can contribute as much to the freshwater balance as precipitation minus evaporation (Silva et al., 2006).

Recent studies have shown that the wake of an iceberg is associated with an increase in surface chlorophyll concentration (Schwarz and Schodlok, 2009). Melt-

ing ice contains biologically important micronutrients such as iron (Lin et al., 2011) and may be enriched in nitrate and nitrite (Vernet et al., 2011). Concentrations of other nutrients, such as phosphate and silicate, generally increase with depth in the Weddell Sea (Vernet et al., 2011; Neshyba, 1977). Icebergs can therefore increase nutrient supply near the surface directly in their meltwater (Smith et al., 2007), or by melting at their base that entrains deep water and causes it to upwell (Neshyba, 1977). There has been considerable debate, however, concerning the location where most melting occurs, the vertical displacement of meltwater, and the amount of ambient water entrained by upwelling meltwater.

Donaldson (1978) summarized three possibilities for meltwater distribution from ice melting below the ocean surface. First, if little entrainment of surrounding water occurs, meltwater will rise in a relatively thin layer and spread horizontally at the surface as a lens of freshwater. Cooling and freshening of surface water near an iceberg is discussed by Helly et al. (2011a). Second, meltwater that entrains a large amount of ambient water from below the permanent thermocline can rise and appear as a T-S anomaly higher in the water column. Such anomalies have been observed near Pine Island Glacier (Jenkins, 1999). Third, meltwater can spread horizontally in stratified layers, resulting in steps in hydrographic profiles. These steps are a common feature of profiles in the Weddell Sea (Huppert and Turner, 1980, hereafter HT80) and have also been measured near the edge of the Erebus Glacier Tongue (Jacobs et al., 1981) and near an iceberg frozen into fast ice (Ohshima et al., 1994).

Here, we present evidence for upwelled meltwater mixtures and horizontal motion of meltwater in stratified layers observed near a free-floating iceberg in the Weddell Sea. These two types of melting are identified in T-S diagrams and potential density profiles and their freshwater contributions to the ocean near the iceberg are estimated.

4.3 Background

4.3.1 Turbulent mixing of meltwater

When ice melts in sea water, two opposing effects on density result. Heat transferred from ocean water to ice raises the ice temperature and effects a phase change, which requires L (344 kJ kg^{-1}) times the mass of ice to be melted, where L is the heat of fusion. As heat is used to melt ice, ambient water is cooled, which increases its density. At the same time, a reduction of salinity by dilution with fresh meltwater makes the ambient water less dense. For a range of temperatures and salinities including values typical of the Southern Ocean (T<10 °C, S>20 psu), the reduction in salinity dominates, making meltwater mixtures positively buoyant (Gade, 1993). Assuming 1) equal effective diffusivities of heat and salt, as can occur in turbulent mixing, and 2) conservative mixing of meltwater and ambient water, melting of ice by sea water produces a mixture that can be described by a linear relation between temperature and salinity (Gade, 1979). Overcoming the heat of fusion requires 80 times the heat required to raise the temperature of the same mass of liquid water by 1 °C. The melting of ice by ocean water can therefore be treated as mixing of two water masses, one with the properties of the ambient water where melting occurs, and one with a salinity of 0 and an effective potential temperature of around -80 °C (or cooler, depending upon the internal temperature of the ice). The intersection of this meltwater mixing line with the freezing temperature at a given salinity and pressure dictates the maximum amount of melting that the ambient water can induce. This sets an upper limit on the concentration of meltwater attainable, assuming there is no external source of heat, of about 1% per °C elevation of ambient temperature above freezing (Jenkins, 1999).

In T-S space, this meltwater mixing line intercepts the ambient water properties at the temperature and salinity of the depth where melting occurs and has a characteristic slope

$$\left(\frac{\partial T}{\partial S}\right)_{melt} = \frac{\Delta T + L{c_p}^{-1}}{S} \tag{4.1}$$

where ΔT (°C) is the elevation of ambient temperature above the freezing point of water at salinity S (psu), $L = 334$ kJ kg^{-1} is the latent heat of fusion of water, and $c_p = 4.2$ J kg^{-1} °C^{-1} is the specific heat capacity of water (Gade, 1979).

Because the addition of meltwater to seawater makes the mixture less dense, the meltwater mixture rises to a level at which it is neutrally buoyant. The relative slopes of the T-S curve of the ambient water column, $(\partial T/\partial S)_{ambient}$, and the meltwater mixing line determines how upwelled meltwater mixtures appear. Where the T-S slope within a water column is steeper than $(\partial T/\partial S)_{melt}$, meltwater mixtures will appear as intrusions that are anomalously warm and salty relative to the water surrounding them at their new, neutrally buoyant level (Jenkins, 1999). Where $(\partial T/\partial S)_{ambient}$ is less than $(\partial T/\partial S)_{melt}$, upwelled meltwater mixtures will appear cooler and fresher relative to unaffected water at the same density.

4.3.2 Double-diffusive mixing of meltwater

In the absence of turbulent mixing, the assumption of equal effective diffusivities for heat and salt in equation (4.1) is no longer valid. The molecular diffusivity of heat is two orders of magnitude higher than that of salt, which can lead to double-diffusion. Under the right conditions, double-diffusion can result in the formation of thermohaline staircases (eg. Morell et al., 2006). Near an ice face, melting into a vertical salinity gradient can lead to these "stepped" profiles of temperature, salinity, and density with depth. Thermohaline staircases also occur in the open ocean as a result of salt-fingering where warm, salty water overlies cool, fresh water, or diffusive convection where cool, fresh water overlies warm, salty water (Schmitt, 1994).

In a series of laboratory experiments, HT80 melted vertical ice blocks in a tank of water stratified with a uniform vertical salinity gradient. Melting along a "sloped ceiling" of ice (Jacobs et al., 1981) or a vertical wall (HT80) in a salinity gradient leads to a series of vertically-stacked circulation cells. These cells are visible as horizontal layers of uniform density separated by thin interfaces with a large density gradient. For experiments at a range of oceanic values of temperature

and salinity, HT80 derived an empirical equation for layer thickness, h,

$$h = \frac{0.65\left[\rho(T_{fp}, S) - \rho(T, S)\right]}{\frac{\partial \rho}{\partial z}}, \tag{4.2}$$

where density, ρ, is a function of the depressed freezing point near the ice, T_{fp}, the unperturbed salinity, S, and the unperturbed temperature, T.

Each circulation cell draws in ambient, unperturbed water near the top of the cell (Malki-Epshtein et al., 2004). This water cools near the ice face, is freshened slightly by entrainment of meltwater, and flows out near the bottom of the cell. As water flows out, it is warmed by thermal diffusion across the lower interface and rises slightly. Water flowing in along the tops of cells is cooled in a similar fashion, giving a tilt to the isopycnal layers. Most of the meltwater coming off the ice ends up vertically displaced to 2-3 layer thicknesses above where it formed (Malki-Epshtein et al., 2004).

In this paper, we use equation (4.1) to identify water in T-S diagrams and equation (4.2) to identify water in density profiles that has been influenced by two modes of melting (turbulent or double-diffusive, respectively). We then estimate where each type of melting occurs and gauge the amount of contributed meltwater and the direction (vertical or horizontal) of transport. Our ultimate goal is to understand the implications of iceberg meltwater for nutrient transport and biological productivity.

4.4 Data and Methods

In March and April 2009, a cruise on the RV/IB Nathaniel B. Palmer (NBP) to the Powell Basin (Fig. 4.1) in the Weddell Sea east of the Antarctic Peninsula was undertaken to assess the impacts of icebergs on their biological, chemical, and physical environment. The main object of study was a large tabular iceberg designated C-18a. The iceberg C18 calved from the Ross Ice Shelf in 2002; C-18a is a fragment of C18 that has been tracked by satellite since 2005 (Stuart and Long, 2011). Helly et al. (2011a) estimated the size of C-18a at about 35 km by 6 km with an average height above the water line of 28 m. During the cruise, Sherlock

et al. (2011) used a remote operated vehicle (ROV) to examine the subsurface face of C-18a directly. The maximum depth of ice recorded by a sonar onboard the ROV was 190 m. Since melting is likely to be greater at the edge of the iceberg, where this measurement was taken, the base of C-18a may have been deeper closer to the center of the iceberg. C-18a travelled about 200 km from March 9 to April 1, following a clockwise path around the Powell Basin (Fig. 4.1b). The approximate position of C-18a was estimated from a combination of the ship's location while circumnavigating the iceberg, position fixes from the navigational radar of the NBP, and interpolation in time and space when no direct measurements were available.

This paper focuses on temperature and salinity profiles from 65 CTD casts taken over the course of the cruise. Results from measurements of Fe and other nutrients are reported elsewhere in this issue (Lin et al., 2011; Vernet et al., 2011). Sampling centered around C-18a followed the same general trajectory as the iceberg (Fig. 4.1b), resulting in CTD casts spread across the basin, divided here into four regions : I. March 10-17 (red), II. March 18-22 (blue), III. March 29 - April 2 (green). IV. April 10-11 (magenta). Of the 65 CTD casts performed during the cruise, 56 were deeper than 250 m, with most of these profiles going deeper than 500 m. Of the 56 casts deeper than 250 m, 37 occurred within 20 km of C-18a. Of those 37 casts, 23 were between 0.4 and 2 km from the iceberg and 14 were between 2 and 20 km from C-18a. In a region commonly referred to as "Iceberg Alley" (IA, orange) (Ballantyne, 2002; Schodlok et al., 2006), characterized by a high concentration of small icebergs 15 m to 2 km in length, sampling occurred April 4-9 and included 12 CTD casts deeper than 250 m. An additional 7 CTD profiles collected outside of IA and farther than 50 km from C-18a at the time of survey occurred March 29 and April 3-7; these casts are grouped together (cyan).

4.5 Water masses of Powell Basin

Three main water masses—Warm (or Weddell) Deep Water (WDW), Winter Water (WW), and Antarctic Surface Water (AASW)—comprise the upper 500

m of the water column in Powell Basin (Fig. 4.2). Around 500 m, water properties are characteristic of WDW, with a temperature of 0.5 °C and salinity of 34.6 psu (Solomon et al., 2000). This water mass, a form of Circumpolar Deep Water that is cooled in the Weddell Gyre (Orsi et al., 1993; Rutgers van der Loeff, 1994), varies little across the basin. In the permanent thermocline above the WDW, both temperature and salinity increase with increasing depth with a slope of around 6 °C psu^{-1}. A temperature minimum, also known as the WW, is found in the remnant of the winter mixed layer. Temperature in the WW shows regional variability, with a general decrease to the south, reaching a minimum around -1.7 °C (region IA), compared to -1.3 °C in the north (region III), but all temperature minima occupy a relatively narrow salinity range around 34.4 psu. In the seasonal thermocline, above the WW layer, temperature increases while salinity decreases with a slope ranging from -1.25 °C psu^{-1} in IA to -4 °C psu^{-1} in regions II and III. Surface water properties range from -1 °C in IA to 0.5 °C near regions II and III with surface salinities near ∼33.8-33.9 psu.

The three water masses (WDW, WW, and AASW) form end members to a typical CTD profile in Powell Basin, with the seasonal and permanent thermoclines describing a "V" in T-S space. Deviations from a V-shape occurred in casts taken near the sill separating Powell Basin from the Scotia Sea (Fig. 4.2, blue), where large intrusions characteristic of interleaving water masses occur in the surface layer above the temperature minimum, suggesting that bathymetry or advection of water from the Scotia Sea may influence general water properties.

4.6 Results and Discussion

A series of five casts taken over 6 hours on a transect from 0.85 to 8.96 km west of C-18a shows a clear impact of ice melt on the subsurface water column (Fig. 4.3). Over the 8 km of the transect, the WW layer, marked in red in the left-most, closest cast (Fig. 4.3), decreases in thickness from 150 m to 50 m. The average salinity at 50 to 300 m depth increases with distance from C-18a. Cooler, fresher water near the iceberg suggests the presence of meltwater. To examine the

source of this meltwater, we first examine T-S anomalies consistent with meltwater that is turbulently mixed at depth and upwelled. We then characterize the thermohaline steps that indicate melting along a vertical ice face into a salinity gradient. Finally, we make an approximate calculation of the amount of meltwater attributable to each process.

4.6.1 A meltwater estimate from turbulent processes

Although the thick, well-mixed layer in the profile nearest C-18a in Figure 4.3 (WW marked in red) is cooler and fresher than water at the same depth in the other casts from the transect, when T-S properties are compared along isopycnals, this cast appears anomalously warm and salty (Fig. 4.4a). We use the T-S curve from this cast to illustrate our method for estimating the amount and concentration of meltwater in the vertical profiles due to turbulent basal melting (Fig. 4.4b).

To identify water within the warm, salty anomaly, two local temperature minima (points **a** and **b** in Figure 4.4b) are selected to define the line L_2, where L_2 is a linear approximation to the "unperturbed" T-S relation. Points on the observed T-S curve between **a** and **b** are therefore anomalously warm and salty relative to L_2. Points **a** and **b** also define the vertical extent of the warm intrusion; for the cast shown in Figure 4.4b, they correspond to the depth range from (**a**) 84 m to (**b**) 97 m.

For mixing to produce water with the T-S properties of this anomaly requires the upward displacement of warm, salty water from below the WW layer. We expect melting at the base of the iceberg to produce fresh, cold water. If this water mixes turbulently with ambient water, the resulting water will have a temperature that falls along a line of slope $(\partial T/\partial S)_{melt}$, defined by equation (4.1). The right-hand side of equation (4.1) is calculated using the temperature and salinity data for each cast. The mean value of $(\partial T/\partial S)_{melt}$ over the upper 300 m of a profile is then used as the slope of the meltwater mixing line, L_1. For the example shown in Figure 4.4b, the mean value of $(\partial T/\partial S)_{melt}$ over this depth range is 2.36 ± 0.05 °C psu^{-1}, where the uncertainty is computed as twice the standard

deviation of $(\partial T/\partial S)_{melt}$ over the upper 300 m. In equation (4.1), changes in ΔT and S are small relative to L and the mean value of S, so variations in $(\partial T/\partial S)_{melt}$ are small.

The meltwater mixing line, L_1, serves as an upper bound to the anomalous T-S region found between **a** and **b**. A line with slope $(\partial T/\partial S)_{melt}$ can pass through each point in the anomaly between **a** and **b**. Here we choose the line L_1 that is tangent to the T-S anomalies such that the intercept at $S = 0$ occurs at the maximum possible value for T. For the intrusion between **a** and **b** in the cast shown in Figure 4.4b, the meltwater line L_1 is defined by:

$$T(S) = (2.36 \pm 0.05) \times S - 82.4 \pm 0.2, \tag{4.3}$$

where T has units of °C and S is the salinity. The uncertainty in the intercept is twice the standard deviation of all possible T-intercept values for lines passing through the $T - S$ points between **a** and **b**.

The minimum temperature and salinity required for basal melting to produce the observed anomaly occurs where L_1 intersects the ambient T-S curve at point **c** (Fig. 4.4b). Point **c** defines the location in the permanent thermocline where the absolute value of the temperature difference between the ambient T-S curve and the T-S values defined by L_1 is a minimum. Uncertainties in the temperature and salinity at point **c** (T_c and S_c) are estimated by propagating uncertainties in the equation for L_1 to the intersection point **c**. The depth of point **c** then defines the minimum source depth, Z_{source}, of the upwelled meltwater. The uncertainty in Z_{source} is estimated as the uncertainty in T_c divided by the mean $\partial T/\partial z$ calculated over a 20 m depth range centered at Z_{source}. In the case shown in Figure 4.4b, T_c = -1.02 ± 0.18 °C, S_c = 34.50 ± 0.04 psu and Z_{source} = 253 ± 20 m.

To estimate the amount of meltwater contained in the anomalous T-S region between **a** and **b**, we consider water properties along L_1 as a dilution of the ambient water at **c**. Thus, the concentration of meltwater, M, is determined by

$$M(S) = \frac{S_c}{S} - 1, \tag{4.4}$$

where S is the salinity along L_1. In Figure 4.4b, for the small range of S (34.36-34.43 psu) for which intrusions occur, M ranges from 0.20-0.41%. The uncertainty

in S_c of $\pm$ 0.04 psu leads to an uncertainty in the meltwater concentration at each point of $\pm$ 0.11%. Since L_2 is an approximation to the background T-S relation, we take the concentration of meltwater along this line to be 0.

Points that fall between lines L_1 and L_2 can be described as a linear combination of water from L_1 and water from L_2. Assuming that the water from L_1 and L_2 mixes along isopycnals, and that water at $T-S$ point **p** is a combination of water with properties **d** and **e** (Fig. 4.4b), we solve

$$T_p = \alpha T_d + (1-\alpha)T_e, \tag{4.5}$$

for α, the relative contribution of water from L_1,

$$\alpha = \frac{T_p - T_e}{T_d - T_e}, \tag{4.6}$$

where T_p is the temperature at **p**, T_d is the temperature at **d** and T_e is the temperature at **e** (Fig. 4.4b). T_d and T_e are the temperatures at which the isopycnal through **p** (gray line, Fig. 4.4b) intersects L_1 and L_2, respectively. Uncertainty in L_1, described above, leads to uncertainty in T_d. Uncertainty in T_e is due to uncertainties in the slope and intercept of L_2, which result from measurement errors in temperature ($\pm$ 0.001 °C) and salinity ($\pm$ 0.01 psu). Equation (4.6) is nonlinear (particularly for small values of $T_d - T_e$); uncertainties in α are therefore determined using a Monte Carlo approach to perturb T_d and T_e by their estimated uncertainty. At the point **p** in the cast shown in Figure 4.4b, α is 0.57 $\pm$ 0.20. The meltwater fraction at **p** is equal to 0.15 $\pm$ 0.09%, which is a product of the meltwater fraction at point **d** (M_d = 0.26 $\pm$ 0.11%) and the relative contribution α (0.57 $\pm$ 0.20) of water with properties at **d**.

Integrating α over the depth range of the T-S anomaly gives the amount of upwelled water in an intrusion. The water column corresponding to the the T-S region between **a** and **b** in Figure 4.4b contains 7.2 $\pm$ 2.6 m^3 of water per m^2 horizontal area that has upwelled from 253 $\pm$ 20 m to a new depth of 84-97 m, a vertical displacement of more than 150 m. Integrating αM over intrusion **i** (Fig. 4.4b) yields an integrated meltwater content of 2.2 $\pm$ 1.2$\times 10^{-2}$ m^3 per m^2 area. Two more anomalies in the cast depicted in Figure 4.4b (**ii** and **iii**) contribute an additional 9.0 $\pm$ 5.0 $\times 10^{-2}$ m^3 per m^2 area of freshwater to the WW layer with

91.6 ± 29.0 m^3 of water upwelled from 246 ± 2 m into the depth range 97-240 m. This estimate of the amount of water upwelled due to meltwater injection at the base of the iceberg is sufficient to explain the 100 m increase in WW layer thickness in this cast relative to casts farther away (Fig. 4.3).

Meltwater intrusions similar to that shown in Figure 4.4b were identified in 11 of the 23 casts closer than 2 km to C-18a, in 5 of the 12 casts in Iceberg Alley, and in 1 cast 17 km from C-18a (Table 4.1). These T-S anomalies are smaller than the large excursions hypothesized as due to water mass interleaving found in casts near the sill to the northwest of Powell Basin (see for example blue casts in Fig. 4.2). The slopes of the T-S anomalies due to meltwater intrusions are generally close to the ∼2.4 °C psu^{-1} typical of meltwater mixing lines. Their appearance in casts close to icebergs and absence in casts in the same region but farther from icebergs suggest a local source. Most meltwater intrusions were found in region I (Fig. 4.1b, red). The meltwater intrusion identified in the cast 17 km from C-18a may be associated with a smaller iceberg observed in the vicinity at the time of the CTD cast.

A summary of the depth range of meltwater intrusions observed in these casts, the associated volume of meltwater and upwelled water, and the estimated source depth of meltwater is presented in Table 4.1. Warm, salty anomalies in T-S diagrams occurred primarily within the WW layer and at the base of the seasonal thermocline. For casts closer than 2 km to C-18a, the anomalies occurred over a range of depths from 67 m to 240 m, although the typical vertical extent of meltwater intrusions was ∼27 m. Three casts that were less than 1 km from C-18a showed multiple meltwater intrusions within one profile. Estimates of Z_{source} from casts within 2 km from C-18a ranged from 163-305 m, with a median depth of ∼233 m, consistent with the iceberg keel depth of at least 190 m from direct observations (Helly et al., 2011a). In Iceberg Alley, which was populated by icebergs much smaller than C-18a, intrusions occurred in a narrower depth range of about 76-158 m (Table 4.1) and were typically ∼25 m thick. Estimates of Z_{source} for the cast 17 km from C-18a and casts in IA were generally much shallower than those near C-18a, ranging from 124-164 m, at a median depth of ∼138 m (Table 4.1).

Smaller icebergs in IA are likely to have shallower keels than C-18a, consistent with these estimates of meltwater source depth.

The apparent source depth of meltwater intrusions near C-18a showed dependence on the position of a cast relative to fixed points on the iceberg. Although C-18a rotated and translated over the course of the study, when CTD cast locations are considered relative to the iceberg's major axis, a pattern emerges. To describe these variations, we use a north-south orientation of the iceberg's major axis (as depicted near region I, Fig. 4.1b) to describe the positions of CTD casts with meltwater intrusions (Table 4.1). Beginning with casts near the northwestern tip of C-18a and moving counter-clockwise, estimates of Z_{source} ranged from 270-305 m, decreased to 228-253 m at the midpoint of the iceberg's long edge and had a minimum of 163 m near the southern tip. Continuing counter-clockwise from the southern tip, Z_{source} increased to 180-213 m at the midpoint of the iceberg's eastern edge and to 240 m in casts taken near the northeast corner of C-18a. These variations in source depth may indicate that the northwest side of C-18a (in the north-south orientation depicted near region I) was thicker than the southeast side. These differences in thickness could have originated before C-18 initially calved, as a result of melting at the seaward edge of the iceshelf. Enhanced melting along the leading edge of the iceberg, ahead of the iceberg's direction of motion, could also lead to preferential thinning along that side of the iceberg.

Variations in Z_{source} could also result from variations in the depth of the permanent thermocline. We have assumed that each cast is representative of the conditions where melting occurs, but as Figure 4.3 shows, the permanent thermocline may shoal with distance from C-18a. Because water at a given source temperature and salinity is likely to be shallower in a cast farther from C-18a than in a closer cast, shallower estimates of Z_{source} may simply reflect differences in thermocline depth with distance from the iceberg. Thermocline depth may also vary with position around the iceberg, reflecting varying degrees of impact by the iceberg on water ahead or behind the direction of motion of the iceberg. Water ahead of the iceberg's leading edge may be less influenced by meltwater (although it contains upwelled intrusions), have a shallower permanent thermocline, and as

a result produce shallower estimates of Z_{source}.

The volume of meltwater in any one profile due to these upwelled intrusions spanned an order of magnitude from 0.6-13.5 $\times 10^{-2} m^3$ per m^2 (Table 4.1). The volume of upwelled water was also highly variable, and was 2-3 orders of magnitude higher than the volume of meltwater, reflecting the low concentrations of meltwater within an intrusion. In a typical meltwater intrusion near C-18a, O(10 m^3) water from the permanent thermocline is vertically displaced by O(100 m). Larger volumes of meltwater and upwelled water occurred in those casts less than 2 km from C-18a, where the median meltwater content in an intrusion was $\sim 2.8 \times 10^{-2} m^3$ per m^2 horizontal area and the median volume of upwelled water was $\sim$11.3 m^3, displaced vertically by $\sim$93 m. Farther from C-18a and in IA, the volume of meltwater in a typical intrusion was $\sim 1 \times 10^{-2} m^3$ per m^2, with an associated $\sim$8.7 m^3 per m^2 of water in the permanent pycnocline displaced $\sim$30 m upwards.

An intermittent physical mechanism for these meltwater intrusions could explain their localization and the variability of their meltwater content. If meltwater at the base of an iceberg is well-mixed, it would produce a less dense mixture of meltwater whose upward motion is constrained by the keel of the iceberg. This positively buoyant water would occasionally "spill" upwards from the edge of the iceberg and rise to a depth at which it is neutrally buoyant. Mixing with water as it rises or at its new density level would move the T-S properties away from the meltwater mixing line, resulting in T-S anomalies whose core has a slope near 2.4°C psu^{-1} and whose sides relax towards the ambient T-S curve. Several discrete upwelling events like this could explain the casts that exhibited multiple intrusions; such an intermittent mechanism would also explain why many casts close to icebergs did not display these intrusions and why such a large range of upwelled volumes was observed.

4.6.2 A meltwater estimate from double-diffusive processes

Melting along the vertical sides of an iceberg is a second source of freshwater that can ultimately be entrained into horizontally stratified layers. Unlike the intrusions associated with upwelled basal meltwater, these layers are not evident

in T-S diagrams, but are instead visible as steps in profiles of temperature, salinity, and density. As an example, steps are evident in profiles of potential density in two casts taken an hour apart at distances 0.4 km (Fig. 4.5a, left) and 1.3 km (Fig. 4.5a, right) from C-18a on 22 March 2009 (at 51.59° W, 61.68° S and 51.59° W, 61.67° S, respectively, blue in Fig. 4.1b). These thermohaline steps possess several of the qualities found in laboratory studies (HT80). One expected feature of layers formed by sidewall melting in a salinity gradient is an upward tilt away from the cooling source (HT80; Malki-Epshtein et al., 2004). In both casts in Figure 4.5a, steps appear at the same potential densities, but are displaced upwards by ∼12 m in the more distant cast (Fig. 4.5a, right), suggesting that layers are coherent over a distance of at least 0.9 km. The two casts shown in Figure 4.5 confirm that isopycnals slope upwards away from the ice face, as suggested by HT80. Another expected feature of the circulation cells is freshening with depth within a layer due to entrainment of meltwater into the outward-flowing circulation (HT80; Malki-Epshtein et al., 2004). Here we find negative values of the salinity gradient with depth, $\partial S/\partial z$, occur over short depth intervals within a generally positive salinity gradient (eg. at 113-115 m depth in Fig. 4.5b, Table 4.2), showing evidence of local freshening.

The circulation cells set up by double-diffusion at an ice face consist of layers of uniform density, bounded above and below by interfaces, where strong gradients occur. To identify possible interfaces in the 56 CTD casts deeper than 250 m, we determined local maxima in the vertical gradient of potential density, $\partial\sigma/\partial z$, (points **f** and **m** in Fig. 4.5b). We considered only points where $\partial\sigma/\partial z$ exceeded a threshold of 4×10^{-3} kg m^{-3} dbar^{-1}, approximately twice the mean of $\partial\sigma/\partial z$ over the upper 300 m of casts close to C-18a. Furthermore, a layer was identified only if the minimum value of $\partial\sigma/\partial z$ (**q** in Fig. 4.5b) between two adjacent interfaces was at least 4×10^{-3} kg m^{-3} dbar^{-1} smaller than $\partial\sigma/\partial z$ at both interfaces (**f** and **m** in Fig. 4.5b). Use of a smaller threshold increased the number of layers identified as steps and resulted in smaller average step sizes. A larger threshold had the opposite effect, finding fewer, larger steps. However, varying the threshold by 1×10^{-3} kg m^{-3} dbar^{-1}, resulted in no significant change in estimates

of the salinity deficit, nor in the resulting freshwater estimate associated with the steps. In some instances where potential density gradients were small, such as below ∼150 m, the use of the 4×10^{-3} kg m^{-3} dbar^{-1} threshold caused two or more step-like features separated by a weak gradient to be counted as one layer. Prior studies (eg Jacobs et al., 1981; Ohshima et al., 1994) that observed small steps embedded in larger steps identified the main layers with the stronger gradients as steps; where such steps occurred, we have done likewise.

The thickness of a layer bounded by the two interfaces (**f** and **m** in Fig. 4.5b) is measured from the bottom of the upper interface (**g**) to the bottom of the lower interface (**n**). The bottom (**g** or **n**) of an interface (**f** or **m**) is identified as the shallowest local minimum in $\partial^2\sigma/\partial z^2$ where $\partial\sigma/\partial z$ is less than the mean potential density gradient between the two interfaces (**f** or **m**). Given the 1 m resolution of the CTD data, the minimum observable layer thickness with this method is 2 m.

In the upper 300 m of the 56 CTD casts considered, 850 layers were identified using this methodology. In Table 4.2 we compare step properties for casts at different distances from the iceberg: closer than 2 km from C-18a; in a range 2-20 km from C-18a; in IA (orange, Fig. 4.1b); and in casts far from ice (cyan in Fig. 4.1b). Typically, ∼15 layers were found in each cast, irrespective of distance from the iceberg. Layers were characterized by average changes in temperature of approximately -0.05 °C, changes in potential density of approximately 0.023 kg m^{-3}, and salinity changes of approximately 0.027 psu on average, except in IA which had larger salinity and density changes and smaller temperature changes (Table 4.2). Layers most commonly appeared above the WW with a mean depth of ∼84 m, except in IA where the mean depth of the isopycnal layers was ∼57 m (Table 4.2). The mean layer thickness agreed within two standard errors, ranging from 7.3 ± 7.9 m in the casts far from the iceberg (C in Fig. 4.1b) to 9.1 ± 6.3 m for those casts less than 2 km from C-18a. The average minimum salinity gradient, $\partial S/\partial z$, was weakly negative (∼-2.4 ± 2.0×10^{-3} psu m^{-1}) for those casts closer than 2 km to C-18a. Farther from C-18a and in IA, the average minimum $\partial S/\partial z$ in a layer was not significantly different from zero. This suggests that freshening with depth within a layer, a feature of circulation cells suggested

by HT80, is more evident in casts closer to C-18a.

To test the predictions of layer thickness made by HT80, we computed h from equation (4.2) using the temperature and salinity from each cast and the freezing temperature calculated using the salinity-pressure profile. Potential density was used in place of density in equation (4.2), and for each cast the vertical gradient in potential density, $\partial\sigma/\partial z$, was averaged with a 50-point running mean.

While the laboratory experiments of HT80 were performed in a uniform density gradient and at constant temperature, the environment of the Weddell Sea has neither of these features. Variations in salinity, temperature, and $\partial\sigma/\partial z$ with depth (eg. Fig. 4.5a) lead to a vertically varying predicted layer thickness, h (Fig. 4.6a). Predicted layer thickness reaches a minimum of about 2.5 m in the temperature-minimum layer, where water as cool as -1.5 °C is already close to the depressed freezing point (Fig. 4.5a).

For each step identified in the potential density profiles, the observed and predicted layer thickness were binned by depth and averaged (Fig. 4.6b). Agreement between observed and predicted layer thickness is best from 40 to 100 m depth (Fig. 4.6b). In the surface mixed layer, air-sea heat flux and wind forcing mix out any stratified step structure, resulting in very few layers being identified in the upper 50 m. The resulting low stratifications in the surface mixed-layer lead to a breakdown in equation (4.2). This suggests that, in the surface layer, the dominant direction of meltwater motion is upwards, and also that double-diffusive melting into stratified layers may not be a relevant mixing process in this part of the water column.

Thicker layers observed below the temperature minimum (130-180 m in Fig. 4.5a) could be due to merging of two or more smaller layers with distance from the iceberg. Greater buoyancy of meltwater at depth results in meltwater that rises more quickly, which could lead to thicker layers at greater depth. Below the temperature minimum, water that is cool and fresh overlies warmer, saltier water and diffusive convection can occur, rather than salt fingering, which may also enhance layer thickness.

Following Jacobs et al. (1981), we estimate the amount of meltwater present

in the thermohaline steps by assuming that a salt deficit can be defined by the area between the salinity-depth profile of a typical thermohaline step and a line drawn tangent (**R** in Fig. 4.5b) between the bases of the two interfaces (**g** and **m**) that define the step (dashed lines in Fig. 4.5b). Water at the tops of the circulation cells (at **g** and **m**) is ambient water cooled slightly as it is drawn in towards the ice; it has the salinity of the ambient water, making line **R** a linear approximation to the background salinity profile.

Physically, we also assume that the observed steps are formed by the addition of freshwater to the water column and are not due to a rearrangement of T and S within the water column. Where the water column is diffusively stable (warm, fresh water over cool, salty water), as it is in the seasonal thermocline above the WW layer, diffusive convection and salt-fingering do not occur, suggesting that sidewall melting could be the predominant cause of the steps. The salinity deficit for the case pictured in Figure 4.5b is 0.05 psu m, equivalent to a deficit of about 0.05 g cm^{-2} salt or the addition of 1.5×10^{-2}m^3 freshwater to a 1 m^2 area of the water column.

In casts closer than 2 km to C-18a (Table 4.2), steps with a mean ($\pm$ 2 standard errors) salinity deficit of 0.042 ± 0.035 g cm^{-2} imply a freshwater excess of 1.23 ± 1.03 cm per step. The amount of freshwater in layers at other sites agreed within two standard error bars (Table 4.2), but the average freshwater excess in a typical layer in IA was not significantly different from zero. Integrating the freshwater excess over each cast, we find that the total freshwater contribution in the upper 300 m of a 1 m^2 water column due to sidewall melting is O(0.1-0.2 m^3).

4.7 Conclusions

At least two modes of meltwater mixing appear to contribute freshwater to the region near C-18a. Warm, salty anomalies appear primarily in CTD casts taken less than 2 km from the iceberg. The amount of meltwater, the proximity to the iceberg, and the close match in T-S space with the slope of the predicted meltwater mixing line are consistent with upwelled mixtures of basal melt and

ambient water near the base of the iceberg. Upwelled basal meltwater is highly variable in space, and appears to be localized; intrusions are detectable mostly within about 2 km of the iceberg. Only half of the casts within 2 km of C-18a exhibited these intrusions, suggesting that upwelling of meltwater mixtures may be an intermittent process. Where basal melting occurs, it appears to be responsible for O(0.1 m^3) of freshwater in a 1 m^2 water column. A small amount of ice is melted, cooling and freshening a much larger volume of water from the permanent thermocline. This water does not rise all the way to the surface, but instead finds a neutrally buoyant level at the base of the seasonal thermocline, where it forms a thick layer of water that, although slightly warmer than the ambient WW at the same density, is cool relative to the AASW and WDW. This supports the idea suggested by Jacobs et al. (1979) that icebergs may play a role in maintaining the WW layer.

The highly variable nature of the upwelling basal meltwater mixtures may contribute to the observed patchiness in micronutrient supply (Lin et al., 2011) and in the phytoplankton (Vernet et al., 2011) and zooplankton (Kaufmann et al., 2011) communities near C-18a. Vertical nutrient transport can stimulate primary production, but the initial effect of a large injection of deeper water (from ∼200 m) into the euphotic zone (estimated to be 50-100 m deep (Vernet et al., 2011)) is likely to be a dilution of phytoplankton populations. This may be a factor in the delay between passage of an iceberg and increased productivity in its wake (eg. Schwarz and Schodlok, 2009; Helly et al., 2011a).

Thermohaline steps consistent with melting from a vertical ice face are ubiquitous in profiles in this region, especially in the depth range 40-100 m. These steps exhibit many of the properties of the meltwater layers observed in the tank experiments of HT80. The average thickness of layers associated with steps in the seasonal thermocline matches that predicted by equation (4.2). Layers appear to be continuous over short distances and tilt upwards with distance from the iceberg. Freshening towards the bottom of the steps is also observed. The amount of freshwater contained in thermohaline steps within a 1 m^2 water column is ∼0.1-0.2 m^3, similar to the estimated freshwater ascribed to upwelled basal meltwater

mixtures. This value is 2-3 times larger than the 0.06 m^3 per m^2 that Jacobs et al. (1981) observed near the Erebus Glacier Tongue, where conditions were much cooler.

The appearance of these steps in all of the casts we examined, even far from ice, and in a diffusively-stable part of the water column suggests that they are stable and that the influence of melting ice is discernible across the Powell Basin. Horizontal spread of meltwater and associated nutrients by double-diffusive circulation cells provides a means by which the seasonal thermocline can be enriched in nutrients from ice melt over a much larger area than turbulent upwelling without diluting microbial and planktonic populations. Near an ice face, where ice is actively melting, advection by shear flow between cells could contribute to the formation of thin, vertically-stacked layers in existing patches of plankton, and could act to enhance horizontal dispersal of such patches.

This study confirms that both basal and sidewall melting contribute significant amounts of freshwater to the upper ocean near icebergs. No single mechanism dominates subsurface ice melt. Basal melt induces vertical transport of potentially nutrient-rich water, while sidewall melting has the potential to enrich the thermocline in micronutrients over a large areal extent. The data collected in this study were not sufficient to characterize horizontal variations in subsurface meltwater or the detailed advection of meltwater relative to the iceberg. These issues will require further detailed field work.

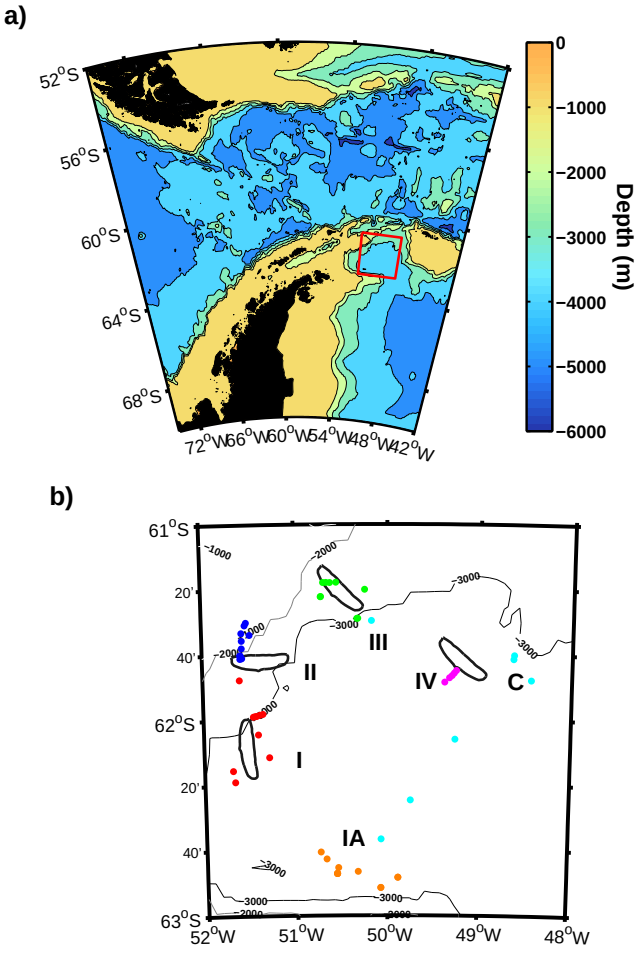

Figure 4.1: (a) Powell Basin is in the northwest Weddell Sea, just east of Drake Passage and the Antarctic Peninsula, south of the Scotia Sea. (b) C-18a travelled clockwise around the Powell Basin; the estimated positions on March 11 (I), March 22 (II), March 31 (III), and April 10 (IV) are indicated. CTD casts were collected near C-18a on March 10-17 (red), March 18-22 (blue), March 29-April 2 (green), and April 10-11 (magenta). Sampling occurred in Iceberg Alley (IA, orange) April 4-9. Outside of IA, casts that were more than 50 km from C-18a at the time of survey are grouped together (cyan) and include casts taken April 3-7 at or en route to a reference station (C) and one cast taken ∼74 km from C-18a on March 29 (near III).

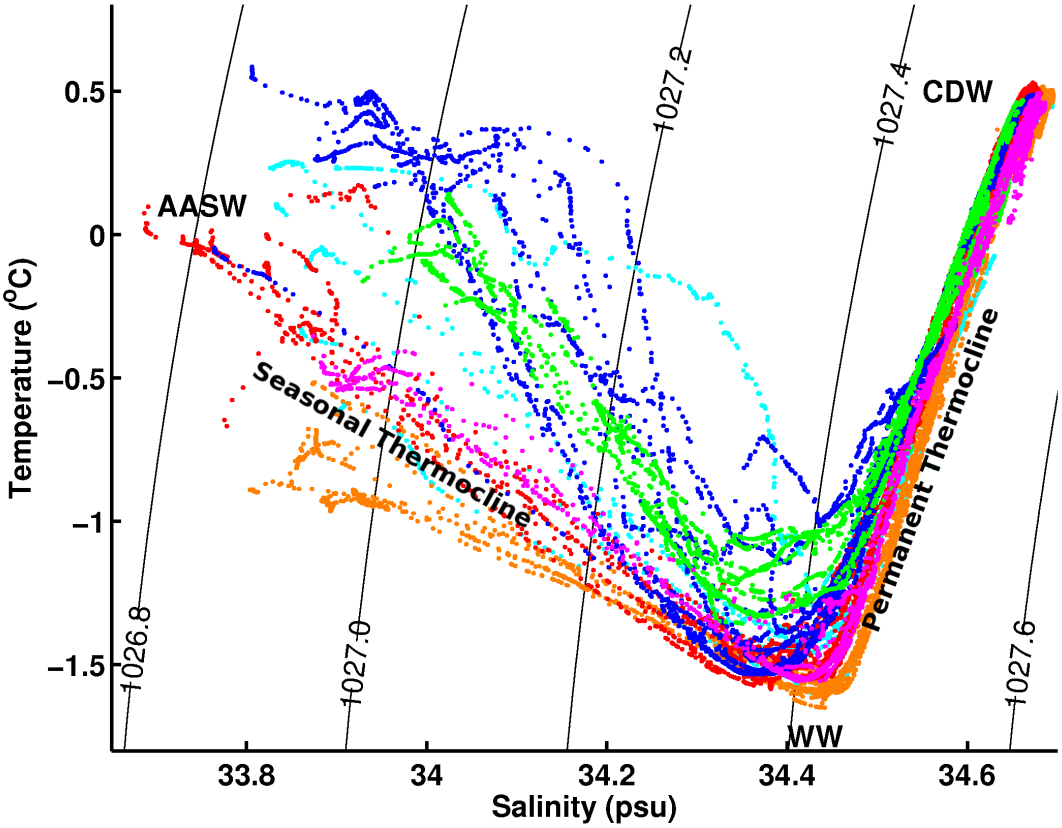

Figure 4.2: T-S curves for 56 CTD profiles are grouped by location and time and color-coded as in Fig. 4.1. CTD casts were collected near C-18a on March 10-17 (red), March 18-22 (blue), March 29-April 2(green), April 10-11 (magenta), in Iceberg Alley (orange), and far from ice (cyan). A seasonal thermocline lies between the AASW and WW. A permanent thermocline separates WW from WDW.

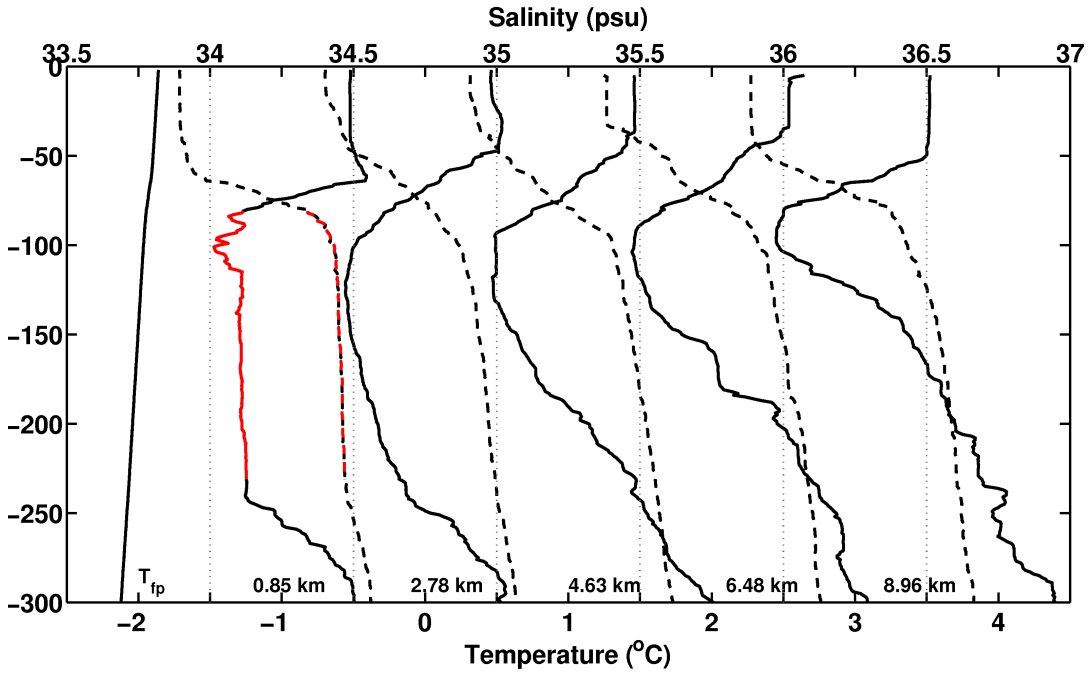

Figure 4.3: The freezing temperature of seawater (T_{fp}, solid line at left), temperature (solid) and salinity (dash-dot) profiles with 1 °C and 0.5 psu offsets (left to right) 0.85 km, 2.78 km, 4.63 km, 6.48, and 8.96 km west of C-18a collected over a 6-hour period April 10-11 (Region IV, magenta in Fig. 4.1b). The Winter Water layer in the cast 0.85 km from C-18a is highlighted in red.

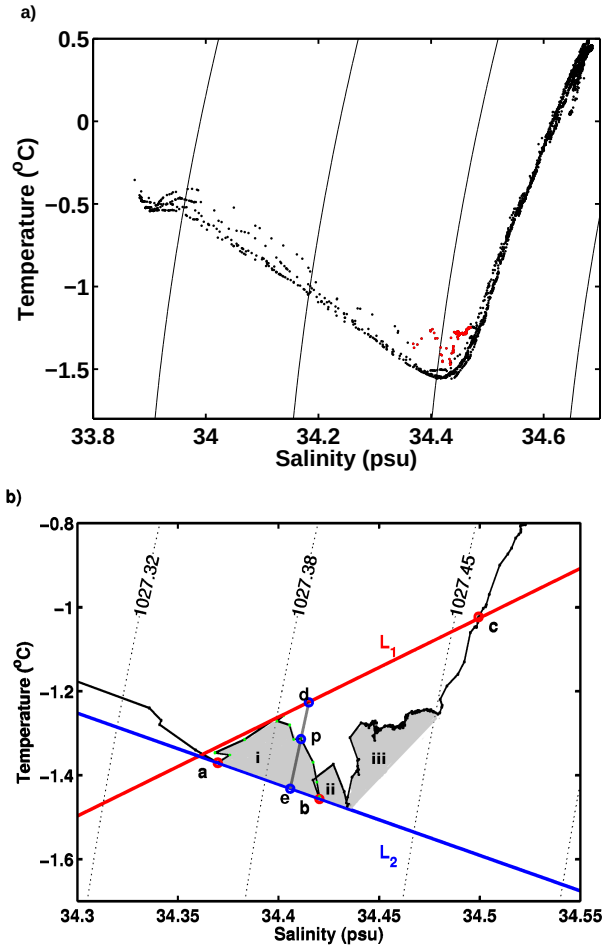

Figure 4.4: (a) T-S diagrams of casts taken 10-11 April (IV, magenta in Fig. 4.1). The cast 0.85 km from C-18a (see Fig. 4.3) shows warm and salty anomalies in the temperature-minimum layer (red). (b) Expanded view of a warm, salty anomaly (**i**) bounded by points **a** and **b**, illustrating the meltwater estimation procedure outlined in the text. A point **p** in the anomaly is modeled as an along-isopycnal mixture of water at **d** from the meltwater mixing line, L_1, and water at **e** from a linear approximation to the ambient T-S relation, L_2. The temperature and salinity required for basal melting to produce the anomaly (**i**) occurs where L_1 intersects the ambient T-S curve at **c**. Two additional anomalies (**ii** and **iii**) are evident in this cast.

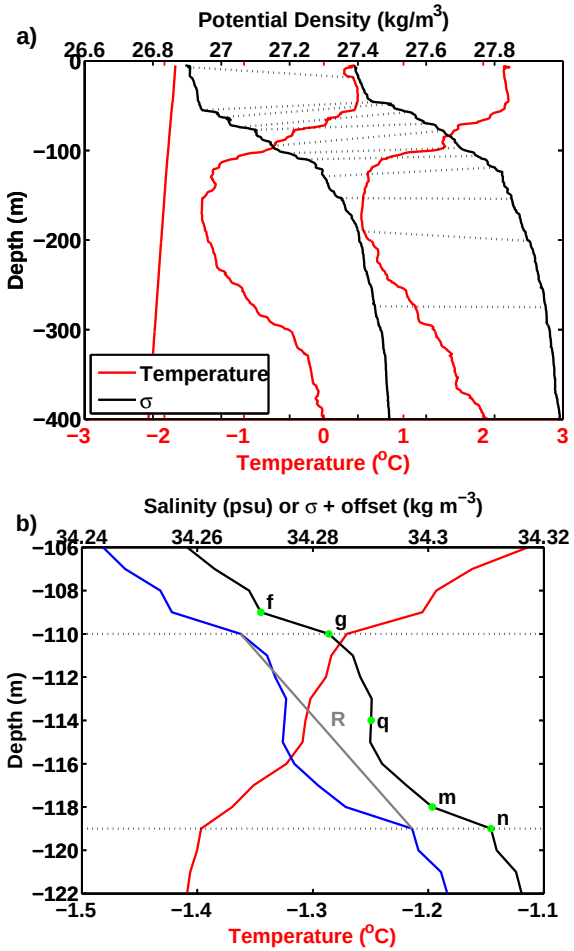

Figure 4.5: (a) The freezing temperature (red line, left) and profiles of temperature (red) and potential density (black) in two casts taken one hour apart 0.4 km (left) and 1.4 km (right) south of C-18a, March 22 (blue in Fig. 4.1b). The profile on the right is offset 2 °C and 0.2 kg m^{-3}. Isopycnals (dotted line) slant upwards away from the ice in 50-100 m depth range, so that steps in temperature and potential density in the cast at 0.4 km are evident at the same potential densities in the cast at 1.4 km, shifted vertically by $\sim$ 12 m. (b) Expanded view of a step in temperature (red), salinity (blue) and potential density (offset by -992.99 kg m^{-3}) (black) in the cast 0.4 km from C-18a (left profile in (a)), illustrating the step-finding procedure outlined in the text. The interfaces at **f** and **m** have lower bounds at **g** and **n**, respectively, at depths indicated by the dotted lines. A minimum in $\partial\sigma/\partial z$ is found at **q**. R is drawn tangent to the salinity/depth profile at the depths of **g** and **n**. The area between R and the salinity-depth profile (blue line) defines the salinity deficit.

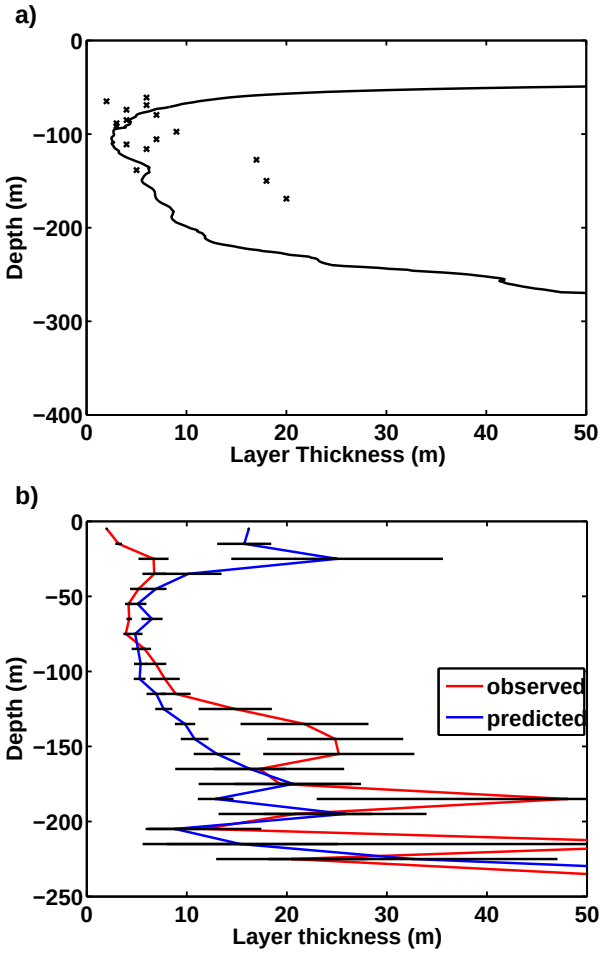

Figure 4.6: (a) Observed layer thickness (x) and layer thickness predicted from equation (4.2) (solid line), calculated from temperature and salinity data for the profile at 0.4 km in Fig. 4.5a. Layer thickness is at a minimum in the temperature minimum layer and increases below 200 m. (b) Mean observed (red) and predicted (blue) layer thicknesses binned by depth for all layers identified in potential density profiles. Where layers were observed, predicted layer thickness (red) is calculated as the average value of h in equation (4.2) over the depth range of the layer. Black lines indicate standard error. Layer thickness agrees most closely in the 40-100 m depth range, averaging about 5 m.

Table 4.1: Properties of meltwater intrusions in 11 casts closer than 2 km to C-18a, 1 cast 17 km from C-18a, and 5 casts in Iceberg Alley. The intrusion depth range of the warm, salty T-S anomalies are indicated. Source depth of meltwater mixtures and the volumes (per m^2 area) of meltwater and upwelled water in the intrusion are estimated as described for Figure 4.4b in the text. Error bars are computed as described in the text.

Cast #	Dist. to C-18a (km)	Region	Intrusion Depth (m)	Z_{source} (m)	Vol. Melt. (10^{-2} m^3)	Upwelled Vol. (m^3)
19	0.4	II	130 to 154	270 ± 18	6.0 ± 2.5	11.2 ± 4.7
25	0.4	III	67 to 88	241 ± 7	4.8 ± 1.3	8.8 ± 4.7
2	0.6	I	83 to 135	234 ± 24	10.2 ± 4.5	19.2 ± 10.4
			135 to 175	205 ± 7	3.3 ± 1.7	19.2 ± 7.3
9	0.6	I	72 to 77	163 ± 14	1.4 ± 0.5	2.7 ± 1.0
1	0.7	I	97 to 120	244 ± 6	2.6 ± 0.9	5.7 ± 5.5
			120 to 150	231 ± 4	7.6 ± 2.0	21.6 ± 5.8
			150 to 189	220 ± 7	2.7 ± 1.1	11.5 ± 6.5
10	0.7	I	83 to 107	228 ± 20	2.7 ± 0.9	6.2 ± 4.2
65	0.85	IV	84 to 97	253 ± 20	2.2 ± 1.2	7.2 ± 2.6
			97 to 101	241 ± 11	0.3 ± 0.2	2.0 ± 0.9
			101 to 240	246 ± 3	8.7 ± 4.8	89.6 ± 28.1
5	1.2	I	97 to 165	180 ± 7	5.3 ± 2.9	24.4 ± 11.5
30	1.7	III	202 to 208	305 ± 32	0.9 ± 0.5	1.9 ± 1.3
6	1.8	I	97 to 134	202 ± 7	4.6 ± 2.1	17.4 ± 6.8
16	1.8	II	136 to 182	213 ± 8	2.9 ± 1.2	12.8 ± 8.5
3	17.2	I	81 to 90	132 ± 5	0.6 ± 0.3	3.7 ± 2.2
41	–	IA	76 to 98	145 ± 7	1.3 ± 0.7	6.9 ± 4.2
50	–	IA	92 to 118	136 ± 3	1.1 ± 0.5	10.2 ± 4.5
51	–	IA	82 to 106	124 ± 10	1.6 ± 0.7	9.8 ± 4.6
52	–	IA	121 to 158	164 ± 2	0.7 ± 0.3	8.7 ± 7.1
55	–	IA	96 to 117	125 ± 2	0.8 ± 0.3	8.7 ± 3.6

Table 4.2: Mean properties (± twice the standard error) of themohaline steps in profiles of potential density from CTD casts less than 2 km from C-18a, between 2 and 20 km from C-18a, in Iceberg Alley, and other casts far from ice. The reported depth of a layer is the depth of its midpoint. Layer thickness is the distance between the bases of the interfaces that define the layer. $\Delta\sigma$, ΔT and ΔS are the change in potential density, temperature, and salinity across a layer. The minimum salinity gradient, $\partial S/\partial z$, observed within each layer is averaged over the casts in each group. The salinity deficit within a layer is computed as outlined in the text. The freshwater excess is the amount of freshwater required to account for the integrated salinity deficit in each cast.

Profile Group	< 2 km	2 to 20 km	Iceberg Alley	Other
Number of Casts	23	14	12	7
# of Layers per Cast	16.7±1.7	14.9±2.1	12.4±1.2	15.6±1.6
Depth of Layers (m)	89.5±20.1	78.9±15.7	57.2±12.4	82.9±14.1
Layer Thickness (m)	9.1±6.3	7.3±5.3	7.4±6.3	7.3±7.9
$\Delta\sigma$ (10^{-2} kg m^{-3})	2.2±0.9	2.3±0.8	3.1±1.0	2.5±0.9
Δ T (10^{-2} °C)	-5.4±4.7	-5.6±4.9	-2.1±6.0	-3.5±8.8
Δ S (10^{-2} psu)	2.6±1.0	2.7±1.0	3.9±1.2	3.0±1.2
Minimum of $\partial S/\partial z$ (10^{-3} psu m^{-1})	-2.4±2.0	-2.0±2.6	0.6±2.0	-1.9±2.6
Salinity deficit / step (10^{-2} g cm^{-2})	4.2±3.5	3.3±2.6	4.0±5.0	2.2±1.3
Freshwater excess / cast (10^{-2}m^3 per m^2)	18.5±4.7	12.9±4.1	13.5±4.7	9.1±1.5

4.8 Acknowledgments

We are grateful to the staff from Raytheon Polar Services and the captain and crew of the RV/IB *Nathaniel B. Palmer* for their support in the field. We would also like to thank Yvonne Firing for her feedback during the manuscript preparation. The field component of this research was funded by a NSF award to M. Vernet (ANT - 0636730). Data analysis was funded by a NSF award to S. Gille and J. Sprintall (NSF ARRA OCE0850350) and a NASA Earth and Space Science Fellowship to G. Stephenson.

Chapter 4, in its entirety, is a reprint with no modifications to content of the article as it appears in Deep-Sea Research II, 2011, G.R. Stephenson Jr., J. Sprintall, S.T. Gille, M. Vernet, J.J. Helly, and R.S. Kaufmann, reproduced with permission of Elsevier. I was the primary researcher and author of this manuscript. Maria Vernet, John Helly, and Ron Kaufmann contributed to the field component of the research which forms the basis of this chapter. Janet Sprintall and Sarah Gille supervised the analysis and writing of the manuscript.

Chapter 5

Conclusions

In this dissertation, we examined the response of the upper several hundred meters of the ocean to air-sea and ice-ocean interactions in Drake Passage and the Weddell Sea. In Chapters 2 and 3, remote-sensing and reanalysis products were used with a 16-year time series of XBT/XCTD transects to identify upper ocean variability associated with air-sea forcing as well as variability intrinsic to the ocean. In Chapter 2, we showed that one common measure of upper ocean variability, mixed-layer depth (MLD), is poorly suited to this goal in Drake Passage. Low stratification north of the Polar Front leads to MLDs that are poorly defined, while regional and seasonal variations in stratification make MLD an inconsistent measure of upper-ocean changes. By instead considering the heat content within a fixed depth interval of the upper ocean, we found a one-dimensional balance between upper-ocean heat content and air-sea heat fluxes on seasonal timescales. MLD and heat fluxes are two of the largest sources of uncertainty in mixed-layer heat budgets in the Southern Ocean (Dong et al., 2007). Results from Chapter 2 are important for two reasons. First, we showed that on seasonal timescales the amplitude and phase of forcing by several air-sea heat flux products agrees with the observed annual pattern of upper ocean heat content. This suggests that future studies of the upper-ocean heat budget in the Southern Ocean might be aided by an approach that considers heat content over a fixed depth rather than over the mixed layer. Second, Southern Ocean air-sea heat flux products give different estimates of daily and mean heat input to the ocean, so the conclusion that several air-sea heat flux products drive annual cycles of the same amplitude and phase is encouraging. Furthermore, the agreement of these annual cycles with the observed annual cycle in upper ocean heat content provides an indirect corroboration of air-sea heat flux products on seasonal timescales.

Chapter 3 extended the analysis of upper-ocean heat content variability to non-seasonal timescales. At interannual timescales, air-sea heat flux anomalies upstream of Drake Passage contribute significantly to variations in upper ocean heat content in the XBT record. Air-sea heat flux anomalies are strongly correlated with meridional wind anomalies and may be strongly influenced by large-scale climate modes including El Niño and the Southern Annular Mode (SAM). Chapter 3

also explored variations in upper ocean heat content in Drake Passage related to mesoscale eddies and meanders. Using XBT transects and eddy characteristics from a tracked eddy database, typical spatial patterns and heat content anomalies associated with eddies and meanders were explored by the construction of composite cold- and warm-core eddies. Mesoscale eddies and meanders of the Polar Front were shown to dominate the upper ocean heat content variability in Drake Passage. In total, five processes–seasonal air-sea heat fluxes, mesoscale eddies, meanders of the Polar Front, ENSO forcing, and interannual heat flux anomalies–explained 84% of the variance of upper ocean heat content in Drake Passage. Results from Chapter 3 corroborate other investigations that have observed responses of upper ocean temperatures to El Niño and the SAM. These results also illustrate the importance of eddies and meanders to a Southern Ocean heat budget and introduce a method to account for heat content variability due to individual eddies and meanders, which are responsible for much of the year-to-year and intraseasonal variability in upper ocean heat content in Drake Passage.

Chapter 4 addressed one aspect of ice-ocean interactions in the form of free-floating icebergs melting in the Weddell Sea. In this study, standard temperature and salinity profiles were used to investigate the physical mechanisms by which subsurface melting near a large tabular iceberg is dispersed into the ocean. Two mechanisms were explored: (1) turbulent entrainment of meltwater near the base of an iceberg that leads to vertical displacement of relatively warm, salty water, and (2) double-diffusive mixing of meltwater formed near the vertical ice face on the sidewall of an iceberg. These processes contribute roughly equal amounts of meltwater to the water column near an iceberg, but have different potential for impacting the stratification and nutrient distribution of the upper ocean. Free-drifting icebergs present a challenging target for observational campaigns, and this is one of the first studies to observe these processes in the field.

Air-sea-ice interactions span a greater variety of processes than can be fully explored in one dissertation, so there remain many open questions. Chapters 2 and 3 defined, characterized, and largely explained upper ocean heat content variability in Drake Passage. The exact physical mechanisms that lead to a delayed response

of upper ocean heat content to climate-mode forcing remain somewhat speculative and further inquiry will be required to establish direct causal links between atmospheric teleconnections and upper-ocean heat content response. Chapter 4 presented a detailed examination of two processes by which ice-ocean interactions drive ocean variability near one large tabular iceberg in late austral summer. Additional study is needed to determine what factors govern the length and time scales over which these perturbations persist, and to evaluate their importance on a larger regional scale.

References

Alexander, M. A., and Deser, C., 1995: A mechanism for the recurrence of wintertime midlatitude SST anomalies. *J. Phys. Oceanogr.*, **25**, 122137. doi: 10.1175/1520-0485(1995)025<0122:AMFTRO>2.0.CO;2.

Ballantyne, J., 2002: A multidecadal study of the number of Antarctic icebergs using scatterometer data. *Brigham Young University online report*, http://www.scp.byu.edu/data/iceberg/IcebergReport.pdf.

Bindoff, N. L., and McDougall, T. J., 2000: Decadal changes along an Indian Ocean section at 32°CS and their interpretation. *J. Phys. Oceanogr.*, **30**, 1207–1222.

Boé, J., Hall, A., and Qu, X., 2009: Deep ocean heat uptake as a major source of spread in transient climate change simulations. *Geophys. Res. Letters*, **36**(L22791). doi:10.1029/2009GL040845.

Böning, C. W., Dispert, A., Visbeck, M., Rintoul, S. R., and Schwarzkopf, F. U., 2008: The response of the Antarctic Circumpolar Current to recent climate change. *Nature Geoscience*, **1**, 864–869.

Bracegirdle, T. J., Connolley, W., and Turner, J., 2008: Antarctic climate change over the twenty first century. *J. Geophys. Res.*, **113**(D03103), doi:10.1029/2007JD008933.

Brainerd, K. E., and Gregg, M. C., 1995: Surface mixed and mixing layers. *Deep Sea Res.*, **42**, 1521–1543.

Caldeira, K., and Duffy, P. B., 2000: The role of the Southern Ocean in uptake and storage of anthropogenic carbon dioxide. *Science*, **287**, 620–622.

Chelton, D. B., Gaube, P., Schlax, M. G., Early, J. J., and Samelson, R. M., 2011a: The influence of nonlinear mesoscale eddies on oceanic chlorophyll. *Science*, **334**, 328–332.

Chelton, D. B., Schlax, M. G., and Samelson, R. M., 2011b: Global observations of nonlinear mesoscale eddies. *Prog. Oceanogr.*, **91**, 167–216.

Church, J., Gregory, J., White, N., Platten, S., and Mitrovica, J., 2011: Understanding and projecting sea level change. *Oceanography*, **24**, 130–143.

Ciasto, L. M., and England, M. H., 2011: Observed ENSO teleconnections to Southern Ocean SST anomalies diagnosed from a surface mixed layer heat budget. *Geophys. Res. Lett.*, **38**(L09701). doi:10.1029/2011GL046895.

Cunningham, S. A., Alderson, S. G., King, B. A., and Brandon, M. A., 2003: Transport and variability of the Antarctic Circumpolar Current in Drake Passage. *J. Geophys. Res.-Oceans*, **108**. doi:10.1029/2001JC001147.

de Boyer Montégut, C., Madec, G., Fischer, A. S., Lazar, A., and Iudicone, D., 2004: Mixed layer depth over the global ocean: An examination of profile data and a profile-based climatology. *J. Geophys. Res.*, **109**(C12003). doi: 10.1029/2004JC002378.

Deser, C., Alexander, M. A., and Timlin, M. S., 2003: Understanding the persistence of sea surface temperature anomalies in mid-latitudes. *J. Climate*, **16**, 57–72.

Donaldson, P. B., 1978: Melting of Antarctic icebergs. *Nature*, **275**, 305–306.

Dong, S., Gille, S. T., and Sprintall, J., 2007: An assessment of the Southern Ocean mixed layer heat budget. *J. Climate*, **20**, 4425–4442.

Dong, S., Sprintall, J., Gille, S. T., and Talley, L., 2008: Southern Ocean mixed-layer depth from Argo float profiles. *J. Geophys. Res.*, **113**(C6), C06013.

Durack, P. J., and Wijffels, S. E., 2010: Fifty-year trends in global ocean salinities and their relationship to broad-scale warming. *J. Climate*, **23**, 4342–4362.

Fang, F., and Morrow, R., 2003: Evolution, movement and decay of warm-core Leeuwin Current eddies. *Deep-Sea Res. Part II.*, **50**, 2245–2261.

Firing, Y. L., Chereskin, T. K., and Mazloff, M. R., 2011: Vertical structure and transport of the Antarctic Circumpolar Current in Drake Passage from direct velocity observations. *J. Geophys. Res.-Oceans*, **116**(C08015). doi: 10.1029/2011JC006999.

Gade, H. G., 1979: Melting of ice in sea water: A primitive model with application to the Antarctic ice shelf and icebergs. *J. Phys. Oceanogr.*, **9**, 189–198.

Gade, H. G., 1993: When ice melts in sea water: A review. *Atmosphere-Oceans*, **31**, 139–165.

Gille, S. T., 2008: Decadal-scale temperature trends in the Southern Hemisphere ocean. *J. Climate*, **21**, 4749–4765.

Gille, S. T., Lombrozo, A., Sprintall, J., Stephenson, G., and Scarlet, R., 2009: Anomalous spiking in spectra of XCTD temperature profiles. *J. Atm. Oceanic Technol.*, **26**, 1157–1164.

Hall, A., and Visbeck, M., 2002: Synchronous variability in the Southern Hemisphere atmosphere, sea ice, and ocean resulting from the annular mode. *J. Climate*, **15**, 3043–3057.

Hanawa, K., Rual, P., Bailey, R., Sy, A., and Szabados, M., 1995: A new depth-time equation for Sippican or TSK T-7, T-6 and T-4 expendable bathythermographs (XBT). *Deep-Sea Res.*, **42**, 1423–1451.

Hanawa, K., and Talley, L. D., 2001: Mode waters. In *Ocean Circulation and Climate*, editors G. Siedler, and J. Church, 373–386. Academic Press.

Helly, J. J., Kaufmann, R., Stephenson, Jr., G. R., and Vernet, M., 2011a: Cooling, dilution and mixing of ocean water by free-drifting icebergs in the Weddell Sea. *Deep-Sea Res. II*, **58**, 1346–1363.

Helly, J. J., Kaufmann, R. S., Vernet, M., and Stephenson, Jr., G. R., 2011b: Spatial characterization of the meltwater field from icebergs in the Weddell Sea. *Proc. Nat. Acad. Sci.*, **108**, 5492–5497.

Hogg, A. M. C., Meredith, M. P., Blundell, J. R., and Wilson, C., 2008: Eddy heat flux in the Southern Ocean: Response to variable wind forcing. *J. Climate*, **21**, 608–620.

Holland, M. M., Bitz, C. M., and Hunke, E. C., 2005: Mechanisms forcing an Antarctic Dipole in simulated sea ice and surface ocean conditions. *J. Climate*, **18**, 2052–2066.

Holte, J., and Talley, L., 2009: A new method for finding mixed layer depths with applications to Subantarctic Mode Water and Argo. *J. Atmosph. Oceanic Tech.*, **26**, 1920–1939.

Huppert, H. E., and Turner, J. S., 1980: Ice blocks melting into a salinity gradient. *J. Fluid Mech.*, **100**, 367–384.

Isern-Fontanet, J., Garcia-Ladona, E., and Font, J., 2003: Identification of marine eddies from altimetric maps. *J. Atmos. Oceanic Technol.*, **20**, 772–778.

Jacobs, S. S., Gordon, A. L., and Amos, A. F., 1979: Effect of glacial ice melting on the Antarctic Surface Water. *Nature*, **277**, 469–471.

Jacobs, S. S., Helmer, H. H., Doake, C. S. M., Jenkins, A., and Frolich, R. M., 1992: Melting of ice shelves and the mass balance of Antarctica. *J. Glaciol.*, **38**, 375–387.

Jacobs, S. S., Huppert, H. E., Holdsworth, G., and Drewry, D. J., 1981: Thermohaline steps induced by melting of the Erebus Glacier Tongue. *J. Geophys. Res.*, **86**(C7), 6547–6555.

Jacobs, S. S., Jenkins, A., Giulivi, C. F., and Dutrieux, P., 2011: Stronger ocean circulation and increased melting under Pine Island Glacier ice shelf. *Nature Geoscience*, **4**, 519–523.

Jenkins, A., 1999: The impact of melting ice on ocean waters. *J. Phys. Oceanogr.*, **29**, 2370–2381.

Jiang, C., Gille, S., Sprintall, J., Yoshimura, K., and Kanamitsu, M., 2011: Spatial variation in turbulent heat fluxes in Drake Passage. *J. Climate*, **25**, 1470–1488.

Jongma, J. J., Driesschaert, E., Fichefet, T., Goosse, H., and Renssen, H., 2009: The effect of dynamic-thermodynamic icebergs on the Southern Ocean climate in a three-dimensional model. *Ocean Modelling*, **26**, 104–113.

Joyce, T. M., Paterson, S. L., and Millard, R. C., 1981: Anatomy of a cyclonic ring in the Drake Passage. *Deep-Sea Res.*, **28A**, 1265–1287.

Kalnay, E., Kanamitsu, M., Kistler, R., Collins, W., Deaven, D., Gandin, L., Iredell, M., Saha, S., White, G., Woollen, J., Zhu, Y., Chelliah, M., Ebisuzaki, W., Higgins, W., Janowiak, J., Mo, K. C., Ropelewski, C., Wang, J., Leetmaa, A., Reynolds, R., Jenne, R., and Joseph, D., 1996: The NCEP/NCAR 40-year reanalysis project. *Bull. Amer. Meteor. Soc.*, **77**(3), 437–471.

Kara, A. B., Rochford, P. A., and Hurlburt, H. E., 2003: Mixed layer depth variability over the global ocean. *J. Geophys. Res.*, **108**(3079).

Kaufmann, R. S., Robison, B. H., Sherlock, R. E., Reisenbichler, K. R., and Osborn, K. J., 2011: Composition and structure of macrozooplankton and micronekton communities in the vicinity of free-drifting Antarctic icebergs. *Deep-Sea Res. II*, **58**, 1469–1484.

Kubota, M., Iwasaka, N., Kizu, S., Konda, M., and Kutsuwada, K., 2002: Japanese ocean flux datasets with use of remote sensing observations(J-OFURO). *J. Oceanogr.*, **58**, 213–225.

Kuhnel, I., and Henderson-Sellers, B., 1991: Mixed layer modeling with respect to ocean-atmosphere interactions in the eastern Indian Ocean. *Meteorol. Atmos. Phys.*, **46**(1-2), 51–64.

Kwok, R., and Comiso, J. C., 2002: Spatial patterns of variability in Antarctic surface temperature: Connections to the Southern Hemisphere Annular Mode and the Southern Oscillation. *Geophys. Res. Lett.*, **29**(1705). doi:10.1029/GL015415.

Lenn, Y.-D., Chereskin, T. K., Sprintall, J., and Firing, E., 2007: Mean jets, mesoscale variability and eddy momentum fluxes in the surface layer of the Antarctic Circumpolar Current in Drake Passage. *J. Mar. Res.*, **65**, 27–58.

Levitus, S., Antonov, J. I., Boyer, T. P., Locarnini, R. A., Garcia, H. E., and Mishonov, A. V., 2009: Global ocean heat content 1955-2008 in light of recently revealed instrumentation problems. *Geophys. Res. Letters*, **36**(L07608).

L'Heureux, M. L., and Thompson, D. W. J., 2006: Observed relationships between El Niño-Southern Oscillation and the extratropical zonal-mean circulation. *J. Climate*, **19**, 276–287.

Lin, H., Rauschenberg, S., Hexel, C. R., Shaw, T. J., and Twining, B. S., 2011: Free-drifting icebergs as sources of iron to the Weddell Sea. *Deep-Sea Res. II*, **58**, 1392–1406.

Liu, J., Curry, J., and Martinson, D. G., 2004: Interpretation of recent Antarctic sea ice variability. *Geophys. Res. Lett.*, **31**(L02205). doi:10.1029/2003GL018732.

Malki-Epshtein, L., Phillips, O. M., and Huppert, H. E., 2004: The growth and structure of double-diffusive cells adjacent to a cooled sidewall in a salt-stratified environment. *J. Fluid Mech.*, **518**, 347–362.

Marini, C., Frankignoul, C., and Mignot, J., 2011: Links between the Southern Annular Mode and the Atlantic meridional overturning circulation in a climate model. *J. Climate*, **24**, 624–640.

Meredith, M. P., Murphy, E. J., Hawker, E. J., King, J. C., and Wallace, M. I., 2008: On the interannual variability of ocean temperatures around South Georgia, Southern Ocean: forcing by El Niño / Southern Oscillation and the Southern Annular Mode. *Deep Sea Res. II.*, **55**, 2007–2022.

Morell, J. M., Corredor, J. E., and Merryfield, W. J., 2006: Thermohaline staircases in a Caribbean eddy and mechanisms for staircase formation. *Deep-Sea Res. II*, **53**, 128–139.

Morrow, R., Ward, M. L., Hogg, A. M., and Pasquet, S., 2010: Eddy response to Southern Ocean climate modes. *J. Geophy. Res.*, **115**(C10030). doi: 10.1029/2009JC005894.

Nan, S., and Li, J., 2003: The relationship between summer precipitation in the Yangtze River valley and the previous Southern Hemisphere Annular Mode. *Geophys. Res. Lett.*, **30**, 2266.

Naveira Garabato, A. C., Jullion, L., Stevens, D. P., Heywood, K. J., and King, B. A., 2009: Variability of Subantarctic Mode Water and Antarctic Intermediate Water in Drake Passage during the late-twentieth and early-twenty-first centuries. *J. Climate*, **22**, 3661–3688.

Neshyba, S., 1977: Upwelling by icebergs. *Nature*, **267**, 507–508.

Ohshima, K. I., Kawamura, T., Takizawa, T., and Ushio, S., 1994: Step-like structure in temperature and salinity profiles, observed near icebergs trapped by fast ice, Antarctica. *J. Oceanogr.*, **50**, 365–372.

Orsi, A., Whitworth, III, T., and W. D. Nowlin, Jr., 1995: On the meridional extent and fronts of the Antarctic Circumpolar Current. *Deep-Sea Res.*, **42**(5), 641–673.

Orsi, A. H., W. D. Nowlin, Jr., and Whitworth, III, T., 1993: On the circulation and stratification of the Weddell Gyre. *Deep-Sea Res. II*, **40**(1), 167–203.

Peterson, R. G., and White, W. B., 1998: Slow oceanic teleconnections linking the Antarctic circumpolar wave with the tropical El Niño-Southern Oscillation. *J. Geophys. Res.*, **103**, 24573–24583.

Price, J. F., Weller, R. A., and Pinkel, R., 1986: Diurnal cycling: Observations and models of the upper ocean response to diurnal heating, cooling, and wind mixing. *J. Geophys. Res.*, **91**, 8411–8427.

Qiu, B., and Kelly, K. A., 1993: Upper-ocean heat balance in the Kuroshio Extension region. *J. Phys. Oceanogr.*, **23**, 2027–2041.

Rutgers van der Loeff, M. M., 1994: 228 Ra and 228 Th in the Weddell Sea. In *The Polar Oceans and Their Role in Shaping the Global Environment, The Nansen Centennial Volume*, editors O. M. Johannessen, R. D. Muench, and J. E. Overland, 177–186. American Geophysical Union, Washington, D.C.

Sallée, J. B., Speer, K., and Morrow, R., 2008: Response of the Antarctic Circumpolar Current to atmospheric variability. *J. Climate*, **21**, 3020–3039. doi: 1175/2007JCLI1702.1.

Schmitt, R. W., 1994: Double-diffusion in oceanography. *Annu. Rev. Fluid Mech.*, **26**, 255–285.

Schodlok, M. P., Hellmer, H. H., Rohardt, G., and Fahrbach, E., 2006: Weddell Sea iceberg drift: five years of observations. *J. Geophys. Res.-Oceans*, **111**(C06018).

Schwarz, J. N., and Schodlok, M. P., 2009: Impact of drifting icebergs on surface phytoplankton biomass in the Southern Ocean: Ocean colour remote sensing and in situ iceberg tracking. *Deep Sea Res. I*, **56**, 1727–1741.

Sen Gupta, A., and England, M. H., 2006: Coupled ocean-atmosphere-ice response to variations in the Southern Annular Mode. *J. Climate*, **19**, 4457–4486.

Sherlock, R. E., Reisenbichler, K. R., Bush, S. L., Osborn, K. J., and Robison, B. H., 2011: Near-field zooplankton and ice-face biota of free-drifting Antarctic icebergs. *Deep-Sea Res.*, **58**, 1457–1468.

Sijp, W. P., and England, M. H., 2009: Southern hemisphere westerly wind control over the ocean's thermohaline circulation. *J. Climate*, **22**, 1277–1286.

Silva, T. M., Bigg, G. R., and Nicholls, K. W., 2006: Contribution of giant icebergs to the Southern Ocean freshwater flux. *J. Geophys. Res.*, **111**(C03004).

Smith, K., Robison, B. H., Helly, J. J., Kaufmann, R. S., Ruhl, H. A., Shaw, T. J., Twining, B. S., and Vernet, M., 2007: Free-drifting icebergs: Hot spots of chemical and biological enrichment in the Weddell Sea. *Science*, **317**, 478–482.

Sokolov, S., and Rintoul, S. R., 2009: Circumpolar structure and distribution of the Antarctic Circumpolar Current fronts: 2. Variability and relationship to sea surface height. *J. Geophys. Res.*, **114**(C11019). doi:10.1029/2008JC005248.

Solomon, H., Ushida, K., and Suzuki, T., 2000: Interannual variability of Antarctic hydrographic structure and frontal zones along meridional sections between Syowa station and southern Africa. *J. Oceanogr.*, **56**, 1–16.

Sprintall, J., 2003: Seasonal to interannual upper ocean variability in the Drake Passage. *J. Mar. Res.*, **61**, 27–57.

Sprintall, J., 2008: Long-term trends and interannual variability of temperature in Drake Passage. *Progress in Oceanography*, **77**, 316–330.

Stephenson, G. R., Jr., Sprintall, J., Gille, S. T., Vernet, M., Helly, J. J., and Kaufmann, R. S., 2011: Subsurface melting of a free-floating Antarctic iceberg. *Deep-Sea Research II*, **58**, 1336–1345. doi:10.1016/j.dsr2.2010.11.009.

Stephenson, J., G. R., Gille, S. T., and Sprintall, J., 2012: Seasonal variability of upper ocean heat content in Drake Passage. *J. Geophys. Res.*, **117**(C04019). doi:10.1029/2011JC007772.

Stuart, K. M., and Long, D. G., 2011: Tracking large tabular icebergs using the SeaWinds scatterometer. *Deep-Sea Res.*, **58**, 1285–1300.

Thompson, A. F., Gille, S. T., MacKinnon, J. A., and Sprintall, J., 2007: Spatial and temporal patterns of small-scale mixing in Drake Passage. *J. Phys. Oceanogr.*, **37**, 572–592.

Thompson, D. W. J., and Wallace, J. M., 2000: Annular modes in the extratropical circulation. Part I: month-to-month variability. *J. Climate*, **13**, 1000–1016.

Trathan, P. N., and Murphy, E. J., 2002: Sea surface temperature anomalies near South Georgia: relationships with the Pacific El Niño regions. *J. Geophys. Res.*, **108**(C4). doi:doi:10.1029/2000JC000299.

Trenberth, K., and Fasullo, J. T., 2010: Tracking Earth's energy. *Science*, **328**, 316–317.

Turner, J., 2004: The El Niño-Southern Oscillation and Antarctica. *Int. J. Climatol.*, **24**, 1–31.

Vernet, M., Sines, K., Chakos, D., Cefarelli, A. O., and Ekern, L., 2011: Impacts on phytoplankton dynamics by free-drifting icebergs in the NW Weddell Sea. *Deep-Sea Res. II*, **58**, 1422–1435.

White, W. B., and Peterson, R. G., 1996: An Antarctic circumpolar wave in surface pressure, wind, temperature, and sea ice extent. *Nature*, **380**, 699–702.

Willis, J. K., Roemmich, D., and Cornuelle, B., 2004: Interannual variability in upper ocean heat content, temperature, and thermometric expansion on global scales. *J. Geophys. Res.*, **109**(C12036). doi:doi:10.1029/2003JC002260.

Wolfe, C. L., and Cessi, P., 2010: What sets the mid-depth stratification in eddying ocean models? *J. Phys. Oceanogr.*, **40**, 1520–1538. doi:10.1175/2010JPO4393.1.

Wolter, K., and Timlin, M. S., 1998: Measuring the strength of ENSO - how does 1997/98 rank? *Weather*, **53**, 315–324.

Yu, L., and Weller, R., 2007: Objectively analyzed air-sea heat fluxes for the global ice-free oceans (1981-2005). *Bull. Amer. Meteor. Soc.*, **88**, 527–539.

Yuan, X., and Martinson, D. G., 2000: Antarctic sea ice extent variability and its global connectivity. *J. Climate*, **13**, 1697–1717.